CHARACTERISATION OF ELECTROHYDRODYNAMIC FLUID ACCELERATORS COMPRISING HIGHLY ASYMMETRIC HIGH VOLTAGE ELECTRODE GEOMETRIES

A dissertation submitted for the

degree of Doctor of Philosophy

by

Emmanouil D. Fylladitakis, BEng, MSc [Hons]

Monday, 28 September 2015

School of Engineering and Design

Department of Electronics and Computer Engineering

~Page intentionally left blank~

TABLE OF CONTENTS

ABSTRACT

Electrohydrodynamics (EHD) is a promising research field with several trending applications. Even though the phenomenon was first observed centuries ago, there is very little research until the middle 20th century, as the mechanisms behind it were very poorly understood. To this date, the majority of research is based on the development of empirical models and the presentation of laboratory experiments.

This work begins with an extensive literature review on the phenomenon, clarifying conflicts between researchers throughout the history and listing the findings of the latest research. The literature review reveals that there are very few mathematical models describing even the most important parameters of the EHD fluid flow and most are either empirical or greatly simplified.

As such, practical mathematical models for the assessment of all primary performance characteristics describing EHD fluid accelerators (Voltage Potential, Electric Field Intensity, Corona Discharge Current and Fluid Velocity) were developed and are begin presented in this work. These cover all configurations where the emitter faces a plane or another identical electrode and has a cylindrical surface. For configurations where the emitter faces a plane or another identical electrode and has a spherical surface, Corona Discharge Current and Fluid Velocity models have been presented as well.

Laboratory experiments and computer simulations were performed and are being thoroughly presented in Chapter 4, verifying the accuracy and usability of the developed mathematical models. The laboratory experiments were performed using two of the most popular EHD electrode configurations - wire-plane and needle-grid.

Finally, the findings of this research are being summarized in the conclusion, alongside with suggestions for future research. The step-by-step development of the equipotential lines mathematical model is presented in Appendix A. Appendix B covers the mathematical proof that the proposed field lines model is accurate and that the arcs are perpendicular to the surface of the electrodes and to all of the equipotential lines.

LIST OF FIGURES

LIST OF TABLES

DEDICATION

To humanity.

ACKNOWLEDGEMENTS

First and foremost, I would like to mention my mentor, Professor Antonios Moronis, for his continuous assistance, guidance, patience, encouragement and support throughout nearly a decade. Unfortunately, no words in any language that I know can express the debt of gratitude that I owe you. Thank you Professor.

I would like to extend my gratitude to my supervisor, Dr. Michael Theodoridis, whose assistance, guidance and patience made this PhD thesis possible.

Special thanks to Dr. Petros Axaopoulos for his continuous academic and professional assistance and advice throughout the years.

I would also like to thank my family and friends for their conscious and unconscious support throughout the years, as well as all of my teachers and professors, who slowly shaped the person that I am today.

Emmanouil D. Fylladitakis

Monday, 28 September 2015, Uxbridge, Middlesex, London

NOMENCLATURE

Symbol	Description (Unit)
A_{cs}	Discharge cross section area - m^2
D	Ion diffusion coefficient
d	Discharge gap - m
d_s	Distance of each twin electrode from the plane of symmetry - m
E	Electric field intensity - V/m
e^+	Electron charge - 1.6×10^{-19} C
I	Electric Current - Amperes
I_s	Unipolar saturation current limit per unit length - A/m
j	Current density - A/m^2
j_s	Unipolar saturation current limit - A/m^2
J_L	Unipolar saturation current limit for a given field line - A/m^2
K_{ge}	Function of the geometry - $m^{-1/2}$
N	Concentration of the molecules
P	Pressure - mm Hg
q	Line charge magnitude - C
r	Emitter electrode radius - m
Re	Reynolds Number
r_{eq}	Radius of an equipotential circle - m
r_{ion}	Ionization area radius - m
L	Field line arc length - m
T	Temperature - K
t	Time - s
V	Electric potential - Volts
V_D	Velocity of the fluid flow - m/s
v_i	Ionization area volume - m^3
V_{Sr}	Velocity of a fluid at the end of a field line - m/s
Z	Constant defined from boundary conditions
ε	Dielectric permittivity of the fluid - F/m
ε_o	Dielectric permittivity of vacuum - 8.85×10^{-12} F/m
μ	Average ion mobility of the fluid - $m^2V^{-1}s^{-1}$
μ_{dv}	Dynamic viscosity of the fluid - kg/(s m)
ρ	Space charge density - C/m^3
$\rho(t)$	Space charge density versus time - C/m^3
ρ_0	Space charge density within the ionization area - C/m^3
ρ_{fd}	Density of the fluid - kg/m^3
φ	Field line emission angle - °

ABBREVATIONS

AC	Alternating Current
BEM	Boundary Element Method
CFD	Computational Fluid Dynamics
COP	Coefficient of Performance
DC	Direct Current
EHD	Electrohydrodynamic
EMHD	Electromagnetohydrodynamic
ESP	Electrostatic Precipitator
FEA	Finite Element Analysis
FEM	Finite Element Method
HVAC	Heating, Ventilation & Air Conditioning
HVPS	High Voltage Power Supply
MAD	Mean Absolute Deviation
MAPE	Mean Absolute Percentage Error
MOC	Method of Characteristics
NASA	National Aeronautics and Space Administration
TDP	Thermal Design Power
WMAPE	Weighted Mean Absolute Percentage Error

LIST OF PUBLICATIONS

A. X. Moronis, K. N. Kiousis, E. D. Fylladitakis, and N. Simou, "A model for determining the unipolar ionic saturation current in parallel wire-cylinder electrodes during corona discharge," Dielectrics and Electrical Insulation, IEEE Transactions on, vol. 21, pp. 1035 - 1043, 16 June 2014.

E. D. Fylladitakis, M. P. Theodoridis, and A. X. Moronis, "Review on the History, Research, and Applications of Electrohydrodynamics," Plasma Science, IEEE Transactions on, vol. 42, pp. 358-375, 2014.

E. D. Fylladitakis, A. X. Moronis, and K. N. Kiousis, "Experimental Evaluation of a Needle-To-Grid EHD Pump Prototype for Semiconductor Cooling Applications," International Journal Of Circuits, Systems And Signal Processing, vol. 8, pp. 337-342, 10 Jun 2014.

E. D. Fylladitakis, A. X. Moronis, and K. Kiousis, "Design of a Prototype EHD Air Pump for Electronic Chip Cooling Applications," Plasma Science & Technology, vol. 16, pp. 491-501, May 07 2014.

E. D. Fylladitakis, A. X. Moronis, and M. Theodoridis, "Analytical estimation of the electrostatic field in cylinder-plane and cylinder-cylinder electrode configurations," Electromagnetics (Pending Review), 2015.

E. D. Fylladitakis, A. X. Moronis, and M. Theodoridis, "A mathematical model for determining an electrohydrodynamic accelerator's flow limit during positive corona discharge " Proceedings of the IEEE (Pending Review), 2015.

E. D. Fylladitakis, A. X. Moronis, and M. Theodoridis, "An analytical model for the determination of the unipolar ionic saturation current during positive corona discharge for geometries comprising cylindrical and spherical emitter electrodes," IEEE Transactions on PLasma Science (Pending Review), 2015.

K. N. Kiousis, A. X. Moronis, and E. D. Fylladitakis, "Ionic wind generation during positive corona discharge in a wire-cylinder air gap," International Journal of Engineering Science and Innovative Technology (IJESIT), vol. 4, January 2015.

A. X. Moronis and E. D. Fylladitakis, "Assessment of a wire-grid EHD pump for the cooling of computer CPUs," presented at the Science In Technology, Athens, 2015.

K. N. Kiousis, A. X. Moronis, and E. D. Fylladitakis, "Analysis of the Electric Field Distribution in a Wire-Cylinder Electrod Configuration," presented at the

Applied Mathematics and Computational Methods in Engineering, Rhodes (Rodos) Island, Greece, 2013.

K. N. Kiousis, A. X. Moronis, and E. D. Fylladitakis, "Fea Method For Detection Of The Corona Inception Voltage In A Wire - Cylinder Arrangement," presented at the 6th International Conference On Finite Differences, Elements, Volumes, Boundaries, Vouliagmeni, Greece, 2013.

E. D. Fylladitakis, A. X. Moronis, and K. N. Kiousis, "Evaluation of a single needle to grid EHD pump prototype for forced convection cooling applications," presented at the International Conference on Energy, Environment, Ecosystems and Development. (EEED 2013), Rhodes Island, Greece, 2013.

E. D. Fylladitakis, "Characterization of EHD devices - Poster Presentation," presented at the ResCon13, Middlesex, Uxbridge, London, 2013.

K. N. Kiousis, A. X. Moronis, and E. D. Fylladitakis, "Finite Element Analysis Method for Detection of the Corona Discharge Inception Voltage in a Wire-Cylinder Arrangement," in Proceedings of the 6th International Conference on Finite Differences, Finite Elements, Finite Volumes, Boundary Elements (F-and-B '13), Vouliagmeni, Greece, 2013, pp. 188-193.

M. Samarakou, E. D. Fylladitakis, D. Karolidis, W. G. Früh, H. Antonios, S. Athineos, et al., "Evaluation of an intelligent open learning system for engineering education," Knowledge Management & E-Learning (KM&EL), 2015 (Accepted for Publication).

M. Samarakou, E. D. Fylladitakis, W. G. Früh, A. Hatziapostolou, and J. J. Gelegenis, "An Advanced eLearning Environment Developed for Engineering Learners," International Journal of Emerging Technologies in Learning (iJET), 2015.

M. Samarakou, A. Papadakis, E. D. Fylladitakis, A. Hatziapostolou, G. Tsaganou, and W. G. Früh, "An Open Learning Environment for the Diagnosis, Assistance and Evaluation of Students Based on Artificial Intelligence," International Journal of Emerging Technologies in Learning (iJET), vol. 9, 2014.

P. Fokianou, M. Samarakou, D. Kandris, and E. D. Fylladitakis, "Star-Delta Switches Evaluation for Use in Grid-Connected Wind Farm Installations," Advances in Mechanical Engineering, vol. 2014, p. 9, 2014.

P. J. Axaopoulos, E. D. Fylladitakis, and K. Gkarakis, "Accuracy analysis of software for the estimation and planning of photovoltaic installations," International Journal of Energy and Environmental Engineering, vol. 5, 2 January 2014.

P. J. Axaopoulos and E. D. Fylladitakis, "Photovoltaic engineering e-learning applications developed for remote laboratory experimentation systems," International Journal of Energy and Environmental Engineering, vol. 5, pp. 1-10, 2014/03/18 2014.

M. Samarakou, G. Tsaganou, A. Papadakis, J. Gelegenis, E. D. Fylladitakis, and M. Grigoriadou, "Monitoring the Text Comprehension of Students for Profiling in ReTuDiS," Journal of Information Technology and Application in Education (JITAE), vol. 2, pp. 132-142, 02 December 2013.

M. Samarakou, E. D. Fylladitakis, and D. Karolidis, "A Versatile Multimedia Software for Wind Energy Education," European Scientific Journal, vol. 9, 2013.

P. J. Axaopoulos and E. D. Fylladitakis, "Performance and economic evaluation of a hybrid photovoltaic/thermal solar system for residential applications," Energy and Buildings, vol. 65, pp. 488-496, Oct 2013.

P. J. Axaopoulos and E. D. Fylladitakis, "Energy And Economic Comparative Study Of A Tracking Vs. A Fixed Photovoltaic System In The Northern Hemisphere," International Journal of Energy, Environment and Economics, vol. 21, pp. 1-20, 2013.

M. Samarakou and E. D. Fylladitakis, "An Electricity Demand Long Term Forecasting Model for South Europe Based on Economic Parameters," International Journal of Energy, Environment, and Economics, p. 517, 2012.

M. Samarakou, E. Fylladitakis, W. G. Fruh, A. Hatziapostolou, and M. Grigoriadou, "How eLearning Affects The Motivation Of Higher Education Students: A Case Study For StuDiAsE," presented at the Global Learn 2015, Berlin, Germany, 2015.

M. Samarakou, E. D. Fylladitakis, P. Prentakis, and S. Athineos, "Implementation Of Artificial Intelligence Assessment In Engineering Laboratory Education," presented at the 8th Multi Conference on Computer Science and Information Systems, Lisbon, Portugal, 2014.

M. Samarakou, E. D. Fylladitakis, G. Tsaganou, J. Gelegenis, D. Karolidis, P. Prentakis, et al., "Adaptation Of Educational Text To An Open Interactive Learning System : A Case Study For Retudis," presented at the IADIS International Conference e-Learning 2013, Prague, Czech Republic, 2013.

M. Samarakou, E. Fylladitakis, P. Prentakis, A. Papadakis, J. Gelegenis, G. Tsaganou, et al., "A student diagnosing and evaluation system for laboratory-based academic exercises," presented at the 24th annual conference of the Society for Information Technology and Teacher Education, New Orleans, 2013.

P. Axaopoulos and E. D. Fylladitakis, "Performance evaluation of small scale grid connected photovoltaic systems in Europe," presented at the Recent Researches in Environmental and Geological Sciences, Kos island, Greece, 2012.

E. D. Fylladitakis, P. J. Axaopoulos, and K. Moutsopoulos, "An Internet-Accessible Experiment Using a Remote Photovoltaic Laboratory," presented at the Science In Technology, Athens, 2015.

M. Samarakou, E. D. Fylladitakis, A. Papadakis, G. Tsaganou, J. Gelegenis, S. Athineos, et al., "Adaptation of Learning Methodologies for eLearning Environments " presented at the Science In Technology, Athens, 2015.

STATEMENT OF CONTRIBUTION

The primary aim of this work is the study of the electrohydrodynamic (EHD) phenomenon, in order to improve the overall efficiency and performance of this promising technology, focusing on EHD fluid accelerators.

After an extensive literature review, it was found that the vast majority of models used to assess the primary parameters describing an EHD device are either empirical or greatly simplified. Therefore, this work focused on the development of mathematical models for, according to the literature review, the most widely used electrode geometries.

Analytical and, at the same time, practical mathematical models for the assessment of all primary performance characteristics describing EHD fluid accelerators (Voltage Potential, Electric Field Intensity, Corona Discharge Current and Fluid Velocity) were developed and are being presented in this work. These cover all configurations where the emitter faces a plane or another identical electrode and has a cylindrical surface. For configurations where the emitter faces a plane or another identical electrode and has a spherical surface, Corona Discharge Current and Fluid Velocity models have been presented as well.

CHAPTER 1 - Introduction. What is EHD?

Electrohydrodynamics (EHD) is the study of the phenomenon where ionised fluid particles interact with surrounding electric fields and other particles of the fluid. The phenomenon is also known as "electrokinetics" and, in the case of air accelerators, ionic or electric wind. EHD phenomena generally involve the direct conversion of energy from electrical to kinetic, or vice versa.

The phenomenon known as the ionic wind has been observed since in the early 17th century by the Italian Jesuit Niccolo Cabeo [1]. Niccolo Cabeo was unable to explain the phenomenon and thus the first scientific recording of the ionic wind is credited to Francis Haukbsee [2], whose experiments were afterwards repeated by Isaak Newton [3]. Even though scientists observed and recorded the phenomenon, they lacked the knowledge to fully explain it for centuries to come. The first realistic quantitative analysis of the ionic wind had to wait for A.P. Chattock [4], whose work was extended over half a century later, in 1954 by E. Lob [5].

Even in the 20th century, there have been very few researchers working to analyse the mechanisms of the ionic wind and electrohydrodynamic (EHD) effects. Because of that, the phenomenon has not yet been fully investigated and therefore its full potential for practical applications remains undetermined. However, in the 21st century there has been a growing interest over researching electrohydrodynamic effects for various engineering applications, such as propulsion methods [6, 7], surface cooling [8], pollution control [9], cooling applications [10], and even agricultural applications [11].

One of the most promising applications of electrohydrodynamics is the creation of ion driven fluid pumps for thermal cooling configurations and or fluid thrust applications in general. Electro and Magneto Hydrodynamic propulsion methods hold great industrial interest because it does not require any moving parts which might lead to a mechanical failure and it generates no mechanical noise or vibrations, making it idyllic for cooling applications and micro-scale liquid pumping. The applications of the phenomenon do not stop there, as it has been proven that the EHD effect may also augment forced convection cooling systems [12] and miniaturized in order to locally cool minute components [13]; and these are cooling-related applications alone.

1.1 Aims & Objectives

The primary aim of this research project is the study of the EHD phenomenon, in order to improve the overall efficiency and performance of this promising technology. Fundamental research will take place via simulations, parametric analysis and experimental measurements, focused (but not limited to) improving the current state-of-the-art of EHD-based cooling methods and or proposing new methods and configurations based on the EHD phenomenon. With the study of the EHD technology and its extensions being still far from mature, there is great opportunity for both incremental and possibly even revolutionary developments.

With electronics and computers becoming integral parts of everyday life, demand for more efficient, smaller, silent and more reliable cooling solutions for electronic chips and circuits is rising beyond all expectations. Although they are yet far from a mature technology, EHD fluid pumps not only have no moving parts but the designs may reach microscopic proportions with relative ease. The industry is currently researching methods to reliably integrate cooling solutions inside portable and minute devices, as well as to create silent computer chip cooling solutions for everyday systems. EHD pumps can be used as an entirely silent cooling device of remarkable reliability for everyday computer systems and other devices, electronic or not, as well as scaled down to miniscule proportions for use in portable devices, microelectronics and microfluidic applications. Despite these advantages, very little research has been done to identify the characteristics, capabilities and weaknesses of this technology, thus leaving an extreme room for scientific exploration.

The study of experimental EHD pumps for cooling parts such as high power density electronic chips and their effect on they can have on today's computer systems should prove to be a scientifically interesting approach which may lead to interesting conclusions and generate numerous recommendations for future research and development.

1.2 Thesis Outline

To begin with, a thorough literature review will be presented, displaying the current state of the art on electrohydrodynamics, while highlighting the conflicts between different studies and areas that need future research. As shown in the literature review, the vast majority of current studies are experimental, using either simulation software or laboratory tests to produce empirical formulas and results.

Apart from very few approximating studies, there are no clear mathematical models that can be used to assess the primary characteristics of the corona discharge. These figures are also necessary for the understanding of EHD pump performance, as the EHD phenomenon is founded on corona discharge.

There are three major parameters that are considered to be necessary for the thorough description of an EHD device: Voltage, Current and Fluid Speed. All of these figures depend on the geometric characteristics of the electrodes, as well as on environmental parameters. The literature review reveals that there is a great number of electrode configurations that researchers have been experimentally working on, each with its own practical advantages and disadvantages. Therefore, a viable solution needs to be as universally applicable as possible, covering the widest possible range of applications. According to that literature review, the most common experimental setups include either wire or needle electrodes, usually facing a plane or a grid, depending on the application.

As such, this work focused on deriving solutions for these popular configurations. It begins from the presentation of a mathematical solution of the voltage potential and electric field gradient surrounding cylinder-plane and twin cylinder-cylinder electrode configurations. The presented model can be used to assess either of these two figures anywhere within the space surrounding the electrodes. Other useful parameters, such as the peak electric field and the field enhancement factors, are also being presented in this chapter. The results are being verified via the most advanced multiphysics simulation software currently available, COMSOL ver.4.3b.

With the voltage potential and electric field gradient known, the next critical parameter is the electric discharge current. A mathematical solution is presented for the analytical calculation of the unipolar saturation current for cylinder-plane and twin cylinder-cylinder geometries. As the mathematical solution of the unipolar saturation current is necessary for the performance characterization of EHD pumps and its adjustment to match other geometries is not as clear, it is being expanded to cover more electrode geometries, such as point-plane, twin point-point, sphere-plane and twin sphere-sphere. The formula can be adjusted depending on the size of the collector's electrode, allowing it to remain applicable regardless of the discharge gap. The solution is verified via laboratory experiments.

Finally, the last critical parameter of an EHD pump is the fluid velocity. Using part of the solution from the second chapter, regarding the formation of the electric field lines, another mathematical model is developed that allows for the assessment of the fluid velocity limit. The fluid velocity limit is not presented as an estimated average but as a precise solution applicable anywhere within the space surrounding the electrodes. The validity of this model is verified through laboratory experiments.

CHAPTER 2 - Literature Review

This chapter contains a literature review of the research regarding the electrohydrodynamic effects associated with corona discharges, from the first observation of the phenomenon to the most recent advancements on its mathematical modelling, as well as the advancements on specific applications, such as thrust, heat transfer improvement, boundary layer enhancement, drying, fluid pumping and cooling.

2.1 A brief history of the EHD effect - Early years

The earliest observation and recording of electrohydrodynamic (EHD) effects have been made in 1629 by Niccolo Cabeo, who noticed that sawdust would be attracted towards an electrified body, touch it and then be repelled [1]. Cabeo however was unable to realize that this behaviour was due to an EHD effect; thus the first official acknowledgement regarding the discovery of electrohydrodynamics has been given to Francis Hauksbee (1709), who recorded that he had experienced a weak wind blowing when holding a charge tube close to him. Hauksbee's work was continued by Isaac Newton [3], who baptized the phenomenon "electric wind" at the time, a name which lasted for centuries; however, nowadays the term "ionic wind" is far more common. Wilson [14] had even been successful at making practical use of the electric wind as a driving mechanism of a rapid rotary pinwheel. However, even though EHD effects had been observed, the scientists simply lacked the knowledge and technology to fully explain it at the time. The first qualitative theory of the phenomenon is owed to the Italian Tiberius Cavallo [15], who accurately described the electric wind while he was analysing the motion of a fly.

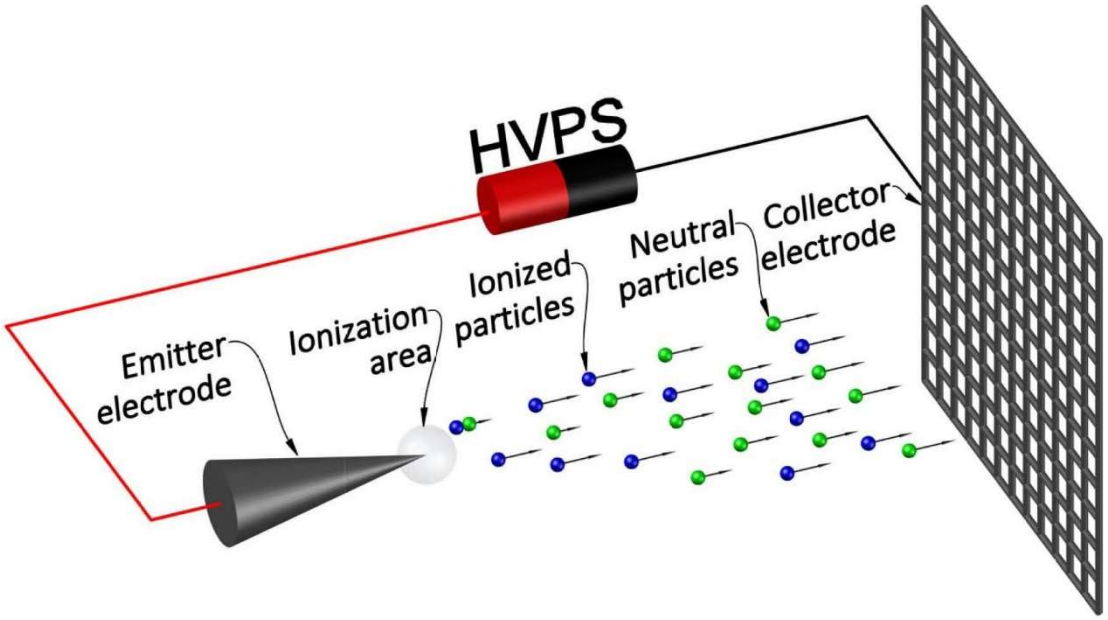

Figure 2.1. Particle stream of a DC electrohydrodynamic device

Significant progress was made several decades later, when Michael Faraday published his annotations on the electric wind [16]. Faraday described the electric wind as a process of momentum transfer, caused by friction or collision between charged and uncharged gas particles, properly identifying the reason behind the movement of the air. Figure 2.1 displays a basic graphic representation of the particle stream between two electrodes when high DC voltage is applied to the emitter.

250 years after the first observation of electrohydrodynamic effects, James Clerk Maxwell performed the first qualitative analysis of the electric wind mechanism [17]. Maxwell attached great importance to the study of the gaseous discharge despite his scarce knowledge in gaseous electronics, prophesizing that "when such processes are better understood, they will throw great light on the nature of electricity, as well as on the nature of gases". Despite the fact that not even rudimentary mathematical treatment could be applied on theories regarding gaseous electronics at the time, Maxwell's work set the basis for future research as it was the most complete at the time and still preserves much of its validity even today.

2.2 Quantitative research and the Befield-Brown effect

Near the end of the 19th century, the very first quantitative analysis of the ionic wind was performed by A .P. Chattock [4]. Chattock derived an experimentally verifiable relationship between pressure and electric current for a configuration of

parallel plane electrodes, setting the foothold for future research. Some years later F. W. Peek wrote one of the first books on high voltage engineering focused on dielectric phenomena, titled "Dielectric phenomena in high voltage engineering" [18]. The book provided a wealth of information at the time, including the properties of gaseous, liquid and solid insulations, methods useful for designing devices, transmission lines, high voltage parts and equipment, as well as methods to perform high voltage engineering experiments, measurement of high voltages, field sketching and explanations of various dielectric phenomena and experimental data. In his book, Peek provided vast information on corona-related effects and mechanisms which were of critical importance to future researchers.

Significant importance has also been given to the work of Thomas Townsend Brown, who noticed that net mechanical force was exerted from a Coolidge X-Ray tube when its asymmetrical electrodes were connected to a high voltage power source. Brown collaborated with Paul Alfred Biefeld and they published an article describing their findings in 1929, indicating that this was not due to a X-Ray effect but due to the ionized particles created by the high voltage electrode, which later came to carry the names of the scientists and become known as the Biefeld-Brown effect [19]. Despite their extensive work on the subject, there have been no scientific publications or books regarding their research, aside from some patents. Also, by reviewing the article and some of their first patents, it would appear that Brown initially misinterpreted the phenomenon for an anti-gravity effect which, among other parts of their work, has been scientifically disproved [20].

Interest on EHD phenomena resurged several years later, when E. Lob [5] investigated Chattock's study of the ionic wind and extended it to other geometries. The thrust properties of the phenomenon also became of interest to the military and Lob's work was soon enhanced by USAF Captain D.S. Harney [21]. Harney examined the electrical parameters of a corona discharge and the variations of particular aerodynamic parameters. Both Lob's and Harney's work has been summarized and expanded by Otmar Stuetzer [22], whose publications were the most complete to that time.

2.2.1 Governing Equations and the Mathematical Problem

The corona discharge in fluids is a complex physical phenomenon which is not yet fully understood. Nevertheless, the simplification of the mathematical problem is

conceivable when appropriate boundary conditions are set [23]. Poisson's equation describing the electric potential V (Eq. 2.1) may be combined with Gauss's law describing the electric field intensity E (Eq. 2.2).

$$\nabla^2 V = -\frac{\rho}{\varepsilon} \tag{2.1}$$

$$\boldsymbol{E} = -\nabla V \tag{2.2}$$

Where ρ_{sc} is the space charge density, ε is the dielectric permittivity of the fluid, μ is the average ion mobility of the fluid and V is the voltage potential of the emitter electrode. Taking into account the current continuity condition, the current density j may be described by Eq. 2.3:

$$\nabla \boldsymbol{j} = 0 \tag{2.3}$$

Current density j is derived from the combination of three parameters: a) the ions moving due to the electric field, b) the charges transported via the molecules due to the fluid flow and c) due to diffusion. Therefore, current density may be also described by Eq. 2.4.

$$\boldsymbol{j} = (\mu_\varepsilon \rho \boldsymbol{E}) + (\rho \boldsymbol{V_D}) - (D \nabla \rho) \tag{2.4}$$

Where μ_ε is the ion mobility, D is the ion diffusion coefficient and V_D is the velocity of the fluid flow.

The Navier-Stokes equation (2.5) describes the motion of the fluid:

$$\rho_{fd} \cdot \left(\frac{\partial \boldsymbol{V_D}}{\partial t} + (\boldsymbol{V_D} \nabla) \boldsymbol{V_D} \right) = -\nabla P + \mu_{dv} \nabla^2 \boldsymbol{V_D} - \rho \nabla V \tag{2.5}$$

Where ρ_{fd} is the density of the fluid, P is the pressure and μ_{dv} the dynamic viscosity of the fluid.

If the fluid flow is incompressible and the density is constant, then the continuity equation reduces to:

$$\nabla \boldsymbol{U} = 0 \tag{2.6}$$

Therefore, these equations can now be used, subject to proper boundary conditions, to provide a feasible solution of the mathematical problem. However, for any geometry where the voltage V is a function of two or more coordinates, the mathematics for solving the described problem may become quite complicated [23]. Consequently, the development and use of numerical techniques was necessary for the

calculation of the aforementioned electrical figures, which significantly impaired the advancement of EHD-related research at the time. Thus, the research interest in electrohydrodynamics resurged only recently, after the explosive development of computers, as the known numerical methods require high computing power.

2.2.2 Advances on the Modelling of the EHD Phenomenon

As soon as it became clear that a mathematical breakthrough would be necessary for the solution of the aforementioned equations, several engineers and scientists explored other methods in order to calculate electric field – related phenomena. The Finite Element Method (FEM) was being established roughly at the same time as the resurgence of the interest on electrohydrodynamics and scientists soon realized that it could lead to satisfactory results via relatively simple calculations [24, 25]. Simply put, FEM divides the domain of the unsolvable problem into numerous triangular elements, forming a mesh of minute subdomains, which subdomains can then be individually solved through consecutive partial differential equations and lead to an approximate solution. This mesh can be denser where finer accuracy is required and sparser in other areas. However, this method leads to massive algebraic systems once high accuracy is vital, even in very small systems, especially if the radii of the electrodes is very small.

Early attempts to utilize the FEM to compute the electrical figures of a corona discharge inside a minute, simple region have been made and the problem proved to be quite complex, even though only a quarter of it required an actual solution due to symmetry [26]. The computation of even basic geometries required immense processing power, which was not available at the time. The accuracy of such simulations was low and using the FEM for the calculation of complex configurations and or configurations using electrodes with very small curvatures remained a prohibitively time consuming procedure. Even several years later, FEM studies on corona discharges were being performed with a mesh formed by a few hundred elements and the computers available at the time would need about an hour to perform a two-dimensional simulation of a simple geometry [27]. In terms of comparison, modern computers can generate the mesh of a two-dimensional problem with hundreds of thousands of elements and solve it within a few minutes. Figure 2.2 shows a detail of a mesh as it has been calculated by a modern simulation software.

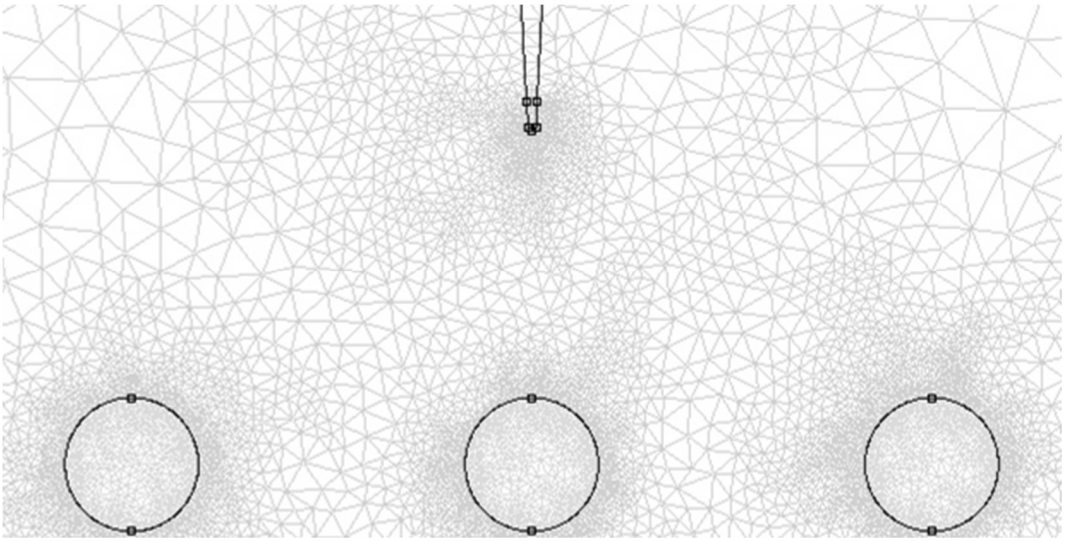

Figure 2.2. Detail of the elements mesh from a modern FEM simulation software (circular collector electrode radius = 1 mm, needle point radius = 32 μm) [28].

As the processing power of computers increased, several scientists began the development of more sophisticated algorithms to simulate complex electric fields in space, as well as flows generated by corona discharges. The first complete algorithm was developed by Morrow [29], who managed to analyse all of the major processes of the corona discharge in the time domain. Several improved algorithms were presented in the following years [30-32]; however, their common characteristic was the significant complexity and the requirement for high computing power. Most of these numerical models use a hybrid combination of multiple numerical methods, such as the boundary element method (BEM), the method of characteristics (MOC), the finite difference and finite volume methods, as well as the FEM.

There have also been numerical models developed via the application of commercial Computational Fluid Dynamics (CFD) software [33-36]. Nevertheless, FEM simulations display much higher popularity as they have been proven to be the most widely accepted computational method for the modelling of electromagnetic problems [37, 38]. Although both open and commercial software utilizing the FEM in order to model electrostatic problems has been available since the dawn of the 21st century [39, 40], the modelling of corona discharges and EHD flows met an explosive growth after 2007, due to the high processing required to reach fine spatial discretization, especially when electrodes with curvatures of very small radii are involved. Studies and models of basic geometries, such as wire-wire [41], cylinder-wire-plane [42], wire-cylinder [43] and needle-plane [44], can be found in

bibliography published during the past few years. However, most research concerning the ionic wind and EHD in general, is performed in order to evaluate specific practical applications rather than finding a universal solution.

2.3 Main Applications of the EHD Phenomenon

2.3.1 Thrust

Ever since the discovery of the Befield-Brown effect, a major part of the research regarding the phenomenon was focused almost entirely on thrust applications. Thomas Townsend Brown had filed several patents of apparatuses intended to be used as propulsion motors, based on his discoveries [45-47]; however, the patent filed by Seversky during the same period, baptized the vehicles propelled by EHD thrusters as "Ionocrafts" [48], clearly in an effort to differentiate his work from that of Townsend Brown and is likely much to blame for today's terms of "ion thruster" and "ionic wind". A few years later, Christenson published a paper with a basic experimental investigation of a multiple needle to plane EHD thruster, which reached an electric to kinetic energy conversion efficiency of approximately 1% [49]. Today, 40 × 40 × 20 mm and 60 × 60 × 20 mm electric fans have an electric to kinetic energy conversion efficiency of about 0.55% [50] and 0.62% [51] respectively. Still, the thrust levels of Christenson's experiments were disheartening for the size and weight of the apparatus.

Because of the complexity of the EHD phenomena that makes it difficult to reach analytical solutions, especially in complex geometries, research on atmosphere-based EHD thrusters has nearly been abandoned. Military research has been taking place from the U.S.A.F. and the S.A.F., which led to advancements on space thrusters during the "cold war", with the most notable achievement being the Hall Effect thrusters which the Soviets have been using to stabilize their satellites for decades [52]. Several EHD and electromagnetohydrodynamic (EMHD) designs have been developed since then for spacecraft propulsion but the involvement of the military withheld most scientific publications until after the dissolution of the U.S.S.R. [53-56]. Such designs require the presence of a gaseous or liquid propellant, usually Xenon gas due to its low ionization potential and heavy molecular weight and, despite the very low levels of thrust, EHD and EMHD space thrusters achieve much higher values

of specific impulse over chemical rockets and are today considered to be the only viable solution for long-term space travel.

Due to their very weak thrust and with no foreseeable technological breakthrough in sight, very few researchers even tried to assess the performance of EHD thrusters for applications in the atmosphere of Earth. As the understanding of the phenomenon grew in the past decade, researchers began by disproving the claims that the Biefeld-Brown effect is an antigravity effect and fully explained it through the simple theory that "the EHD effect uses only electrostatic forces and the transfer of momentum by multiple collisions with the air molecules" [20, 57]. Research followed on the "Ionocraft" [58], with researchers modelling the gas flow of the levitation apparatus, experimentally modelling the electrical and physical characteristics of the flyers [59, 60], as well as trying to optimize the design via the use of the latest FEM modelling software [61].

Aside from the research centred on the triangular lifter apparatus first designed by Townsend Brown, few researchers have tried to develop new methods and EHD thruster electrode geometries. However, the applicability of EHD thrusters in non-conductive liquid environments has been validated through the presentation of a functional micro-boat, propelled by a basic EHD micro thruster [62]. An alteration of the original levitation device was also presented in the form of an indoor surveillance blimp, where helium balloons keep the apparatus afloat without the need of any other levitation force and the EHD device is solely used as a thruster [63]. Although the concept was interesting, the overall size of the apparatus makes practical applications appearing unrealistic, as the balloons were about 1.5 m long and over 1 m wide for an EHD thruster of 106 gr to levitate. A relatively simple, one-dimensional model of ideal EHD thrusters has also been recently presented in [64], shedding some light on the calculations of the thrust and efficiency of EHD lifters, as well as their principal performance limits.

Despite the slow progress of research on atmospheric EHD thrusters, a thorough article was recently released by NASA on ionic wind propulsion, which explored both the same wire to fins geometry as the lifter designed by Townsend Brown and a needle to fins electrode design [65]. The scientists performed parametric experiments to compare the two geometries, optimize the number, distance and size of the electrodes, model the electrical characteristics of the thrusters and derive mathematical relationships for the optimized designs. Although the authors claimed

that the EHD thrusters in their current form did not appear to have any practical use, significant progress was made and they made several research suggestions, which inspired further research.

A recent study experimentally explored the potential of wire-cylinder EHD thrusters, as well as the performance of dual-stage three electrode wire-rod-cylinder EHD thrusters (Figure 2.3), which however did not meet the expected results as, according to the author, very high voltage were necessary in order to generate thrust between the intermediate and the collector electrode and also a reverse corona was being formed at the intermediate cylinder electrode [66].

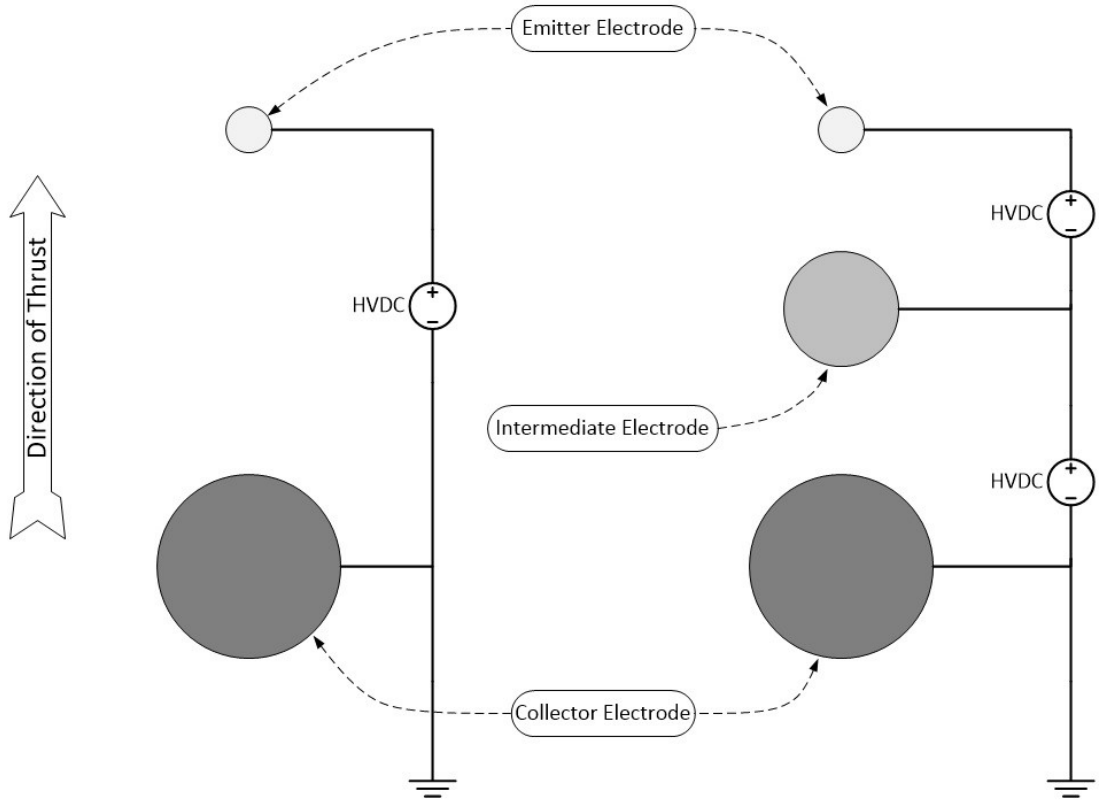

Figure 2.3. Wire-cylinder single stage (left) and wire-rod-cylinder dual stage (right) EHD thruster designs explored by the MIT [66].

2.3.2 Flow & Heat Transfer Enhancement

Research on the effects that EHD flow would have on the boundary layer of a fluid flow and on heat transfer via convection began at roughly the same time as the research on EHD thrust engines [67]. For the following years significant research took place regarding the alteration of the boundary layer by using corona discharges, thus improving forced convection heat transfer or reducing drag; however, most such research was focused on improving existing heat exchangers and known geometries

rather than creating stand-alone ionic wind pumps which would not require externally forced flow.

Due to the complexity of the EHD phenomena, research progress initially was very slow. Fernandez was first to validate that EHD could bring a significant improvement to forced convection inside tubes [68]. Thorough experimental testing of his work and validation of his finding came many years later [69], suggesting that the heat transfer rate could increase up to 20 times over using a concentrical wire to cylinder configuration, even though the pressure drop increase would only triple. Experiments for the same geometry have also been performed by Ohadi [70], who concluded that the maximum possible heat transfer enhancement was 215% for a single emitter electrode and 260% if two emitter electrodes were used; however, that enhancement would diminish as the Reynolds number increased. A recent study of the same configuration displayed that the heat transfer enhancement can reach up to 870% over natural flow [71]. The plane-wire-plane configuration was also explored a few years later, with the researchers' experiments displaying that a heat transfer enhancement of up to 600% is possible in rectangular channels, although the enhancement once again diminished at high Reynolds numbers [72]. Another research exchanged the flat plane for a wavy one and used multiple emitters, creating a multi-wire to wavy plane electrode configuration, which reached a performance enhancement ratio of 6:1 for low Reynolds numbers but, once again, the enhancement ratio fell below 2:1 for $Re \geq 500$ [73].

Significant research has been performed by Léger, Moreau and Touchard on the effect of a corona discharge on the boundary layer when bulk flow already exists, using a wire to plate electrode configuration, with several papers published on the subject [74-76]. The research displayed that there is a significant enhancement on the bulk flow velocity within the boundary layer for velocities up to 25 m/s, the ratio of which however decreases as the bulk flow velocity increases. Additional research on the same configuration has been carried out D. B. Go et al., exploring the enhancement of external forced convection on a heated flat plate [77]. Their experiments displayed that, for a bulk flow velocity of less than 1 m/s, the thermal performance enhancement was over 200%.

Scientists also explored the viability of using EHD to enhance the performance of widespread heat transfer applications. Significant research took place on the augmentation of the heat transfer coefficient in existing systems which were using air

as the cooling medium. Early research results were aligned, with the heat transfer coefficient being augmented by 250-320% [78-82]. However, Mizushina et al. noticed that the augmentation would diminish as the Reynolds number increased, dropping to 150% for *Re* = 2000 and there was little effect once the Reynolds number would be over 4000 [79]. Based on these results, Ohadi [83] proposed that the exploitation of EHD could enhance the efficiency of building HVAC systems, displaying impressive performance increase potential and possibly reducing the heat exchange area enough in order to make use of renewable energy sources, the use of which was cost-inhibitive due to the excessively large exchangers required. Aside from air, scientists also examined the heat transfer enhancement that EHD could offer to other cooling mediums. Early research was mostly based on gaseous heat transfer media, such as nitrogen [84, 85], argon, carbon dioxide and helium [86].

More recent research, however, has been mostly based on phase-changing fluids. The performance augmentation of systems using R113 has been explored first [87, 88], with researchers reporting an enhancement between 60% and 100%. A similar research claimed that the performance of a system using flat silver-plated electrodes and implementing R114 may be increased up to tenfold [89]. Nevertheless, future research on system using R114 as the heat transfer medium displayed performance enhancements as low as 8% [90]. An experimental research using a multiple wire to cylinder EHD apparatus and with R123 and R11 as the heat transfer medium has been performed, indicating that the fluid properties are critical to the EHD enhancement ratio, as there was an enhancement of over 9 times with R123 but negligible enhancement while using R11 [91]. The nowadays popular refrigerant R134a has also been examined with the use of a concentrical wire to cylinder electrode configuration. The first experiments were made with a steady high voltage applied to the emitter electrode [92] and a numerical analysis followed afterwards [93], both displaying that the augmentation of the heat transfer coefficient is significant when R134a is used but the pressure drop penalty was too great for the technology to become an industrially viable application. Recently, experiments were also performed with the same concentrical wire to cylinder geometry by applying a pulsating high voltage to the emitter electrode [94], displaying that the use of pulsed voltage can widen the range of heat transfer and pressure drop, making the systems more amenable to control through the frequency of the pulsations. Table 2.1 summarizes the research results on EHD-augmented heat transfer to this date.

Table 2.1. EHD-augmented heat transfer research results

Author(s)	Electrode geometry	Working medium	Heat transfer coefficient improvement
Robinson [78]	Platinum wire	Air	320%
Mizushima et al. [79]	Coaxial wire-tube	Air	150% (Re=2000) 300% (Re=700)
Velkoff and Godfrey [80]	Wire-plate	Air	≈250%
Tada et al. [81]	Plate-plate	Air	270%
Nelson et al. [82]	Coaxial wire-tube	Air	260%
Velkoff [85]	Coaxial wire-tube	Air, Nitrogen	100% (Re=3000)
Moss and Grey [84]	Coaxial wire-tube	Nitrogen	35% (Re=1200)
Grosu and Bologa [86]	Coaxial wire-tube	Air Helium Carbon dioxide Argon	200% (Air) 200% (He, 21 atm) 400% (CO2) 150% (Ar, 1.4 atm)
Choi [87]	Coaxial wire-tube	R113	100%
Seth and Lee [88]	Coaxial wire-cylinder	R113	60%
Holmes and Chapman [89]	Plate-plate (wedge)	R114	Up to 900%
Damianidis et al. [90]	Tube-plate	R114	8%
Karayiannis T.G. [91]	Rod-tube	R11 R123	≈0% (R11) 830% (R123)
Feng and Seyed-Yagoobi [93]	Coaxial wire-tube	R134a	≈100%

Finally, there has also been significant research regarding the EHD flow which develops in Electrostatic Precipitators (ESPs). EHD flow in ESPs is a by-product of their intended purpose, which is to induce an electrostatic charge on the particles of a flowing fluid, creating electrostatic attraction which will force them to move towards a grounded collector, thus effectively removing them from the stream. This flow of charged particles however, alongside the ionization of particles of the fluid itself, creates an EHD flow which may have a detrimental effect on the performance of the precipitator at low bulk fluid speeds, or is inconsequential at higher bulk fluid flow speeds [95, 96]. Niewulis et al. also hypothesized that the EHD flow affects the collection efficiency of ESP, with the effect being greater as the size of the particles decreases [97]. There have been numerous studies, both simulated and experimental, towards the evaluation of EHD flows inside ESPs of various electrode configurations [98-101]. Despite the degrading effect that EHD flow may have on the performance of ESPs however, recent studies showed that the ozone generation of the corona discharge in air can act as a catalyst, incinerating unwanted particulates in the gas flow [102, 103].

2.3.3 Drying & Evaporation

During experiments regarding the lethality of ions on microorganisms, Krueger discovered that the presence of ions in clean air increases the evaporation rate in droplets [104]. Three decades later, Barthakur, who was observing the progress on the enhancement that ionic wind can offer to heat transfer, investigated the influence that the presence of positive and negative ions could have on evaporation rates. Early studies displayed very promising results, significantly increasing the evaporation rates of thin layers of liquids [105], saline water [106] and soil samples [107]. Soon afterwards, it was also discovered that the ionic wind could significantly enhance the dehydration rates of potato slabs, which drew the attention of the agricultural and energy industries [108].

Over the past couple of decades, significant research has been performed over the enhancement of the evaporation rates that EHD could offer. Many researchers focused on the effect that the phenomenon would have on water [109-111]. Their results on the simplicity and efficiency of EHD drying has led to many researchers exploring the viability of EHD drying for specific industrial applications. After a team of scientists proved that EHD drying can be very effective for drying apple slices and offer great advantages over heat-based methods [112] and, in conjunction with the research on the water evaporation rates, there has been an explosion of articles exploring the effect of EHD drying on a variety of nutrients [113-119]. Each and every one of these studies concluded that the quality of the product, in terms of colour and appearance, has been greatly increased, in addition to their nutrient value due to the sustainment of vitamins and other high value ingredients which are usually destroyed by heat-based drying techniques. It has also been proved that EHD drying is a far more energy efficient method than any form of thermal drying and, in conjunction with the higher end-product quality due to the non-thermal drying process, is highly valuable to the food industry [116]. Research has also been performed on the EHD drying of non-edible materials, such as Agar Gel [120]. The energy industry began displaying great interest as well, as it was proved that EHD drying can enhance the quality of rapeseed [121], commonly used for the production of biofuels, for a lower energy cost than heat-based drying, which can lead to less costly and higher quality biofuels.

The research by the food industry has also brought about results regarding the performance of various electrode configurations. In 2002, the feasibility of a single wire emitter electrode design has been evaluated and displayed that significant drying

performance enhancements can be had even by this very simple electrode geometry [122]. A few years later, the same research team also published a paper on the performance of a drying apparatus using multiple needle emitters, the performance of which however appeared inferior to that of the single wire emitter [123]. Another experimental study has been performed by another research team with a multiple needle to plate electrode configuration which displayed excellent performance, even though it was not apparent that there has been any optimization regarding the geometry of the electrodes [124]. A drying apparatus using a wire-plate electrode configuration has also been experimentally tested, with the research team displaying that the fabrication of an entire functional drying system is fairly easy and can effortlessly be scaled to industrial applications [125]. Table 2.2 summarizes the research results on EHD-augmented drying to this date.

Table 2.2. EHD-assisted drying enhancement research results

Author(s)	Electrode geometry	Drying material	Evaporation rate improvement over ambient air drying
Barthakur and Arnold [109]	Needle-Plane	Water	≈300%
Lai et al. [110, 123]	Needle-plane	Water	Up to 126%
Lai et al. [110, 122]	Wire-plane	Water	Up to 240%
Alem-Rajabif and Lai [111]	Wire-plane	Water	Up to 270%
Barthakur and Bhartendu [105]	Needle-Plane	Water (100ml) Ethyl alcohol (100ml) Carbon tetrachloride (100ml)	≈400% max ≈250% max ≈350% max
N.N Barthakur [106]	Needle-Plane	Saline water	210 to 270% (depending on NaCl % concentration)
Barthakur and AL-Kanani [107]	Needle-Plane	Moisture (soil samples)	200% to 535% (depending on soil composition)
Chen and Barthakur [108]	Needle-Plane	Potato slabs	200% (15 min) 170% (45 min) 140% (180 min)
Hashinaga et al. [112]	Needles-plane	Apple slices	Up to 120%
Bajgai and Hashinaga [113]	Needles-plane	Spinach	Up to 300%
Cao et al. [114]	Needles-plane	Wheat	50% at 50 °C 60% at 35 °C 90% at 20 °C
Li et al. [115]	Needle-plane	Okara cake	Up to 220%
Bajgai and Hashinaga [117]	Needles-plane	Radish	Up to 470%
Esehaghbeygi and Basiry [118]	Needles-plane	Tomato slices	Up to 100%
Alemrajabi et al. [119]	Needles-plane	Carrot slices	Up to 420%
Goodenough et al. [116]	Wire-plane	Biscuits	Up to 450%
Bai et al. [124]	Needles-plane	Scallops	617%
Basiry and Esehaghbeygi [121]	Needles-plane	Rapeseed	Up to 275%
Isobe et al. [120]	Needle-plane	Agar gel	Up to 230%

2.3.4 Fluid Pumps

General Research on EHD Fluid Pumps

The first to suggest the possibility of designing a functional electrostatic blower (i.e. an EHD pump) were Robinson [126] and Stuetzer [127], during their research on the ionic wind. Both researchers examined the same geometry and, therefore, their conclusions were very similar. By experimentally testing a needle-ring electrode geometry, Robinson evaluated the conversion efficiency from electrical energy to mechanical energy via corona discharges but was disheartened by the mediocre results of his experiments, which displayed an efficiency of less than 1%; he did however explicitly mention that EHD pumps have several advantages over mechanical pumps, the main being the lack of moving parts, as a result of which there are no vibrations, no wear and tear, no lubrication requirements and no gyroscopic or rotational effects, as well as virtually no sound during operation.

The low electrical to mechanical energy conversion efficiency is one of the largest problems of EHD pumps and few steps have been taken towards its improvement, yet there have been a few experimental studies focused on improving the exit fluid velocity and efficiency of EHD pumps. However, we should note that due to the different equipment and methods that each researcher used in order to measure the fluid speed and calculate the efficiency of the experimental device, the results of these studies are not directly comparable to each other.

Important work towards this end has been performed by Eric Moreau and Gerard Touchard [128], who focused on improving the electrical to mechanical energy conversion efficiency of the needle-ring and needle-mesh electrode configurations. Furthermore, the researchers tested both positive and negative corona discharges, which occur when positive and negative high voltage potential is applied to the emitter electrode respectively, and their effect on various mesh configurations. It was determined that positive coronas are generally capable of producing higher air velocities, reaching a maximum air velocity of 8 m/s with a positive corona discharge, while a negative corona discharge would generate a maximum air velocity of 5 m/s. The researchers also determined that the air velocity and uniformity are being aided by a dense grid of thin collector electrodes. Regarding the electrical to mechanical energy conversion efficiency, the study clearly displayed that mesh collector electrode configurations are superior to ring collector electrodes, plus that positive coronas are

more efficient than negative ones. The optimal configuration generated an air velocity of 8 m/s with an efficiency of 1.72%, more than double the efficiency recorded in early studies of EHD phenomena. The higher efficiency of the positive coronas for EHD air pumps has also been verified by June et al [129], who experimentally tested the static efficiency of a similar 5 needle to mesh EHD pump prototype. The researcher found that the static efficiency of a positive corona may reach up to 14%, while the maximum static efficiency of a negative corona is less than 2%. J.D. Moon et al. [130] later presented a more complex needle to mesh EHD pump, with the emitter electrode surrounded by a ring at the same voltage potential. With this design the research team claims to have improved the electrical to mechanical conversion efficiency of EHD pump by 2.5 times compared to the needle-mesh electrode design, yet the efficiency of the conversion was parallel to that of the optimized needle to mesh design presented by Moreau [128]. Recently, a study once again investigated the conversion efficiency of the needle-grid geometry EHD pump (Figure 2.4), extending the research to a cascading design and for up to 6 consecutive stages [131]. Through a parametric study, the research team derived that the wind speed is a linear function of the voltage applied to the emitter, as well as a function of the square root of the current multiplied with an empirical constant.

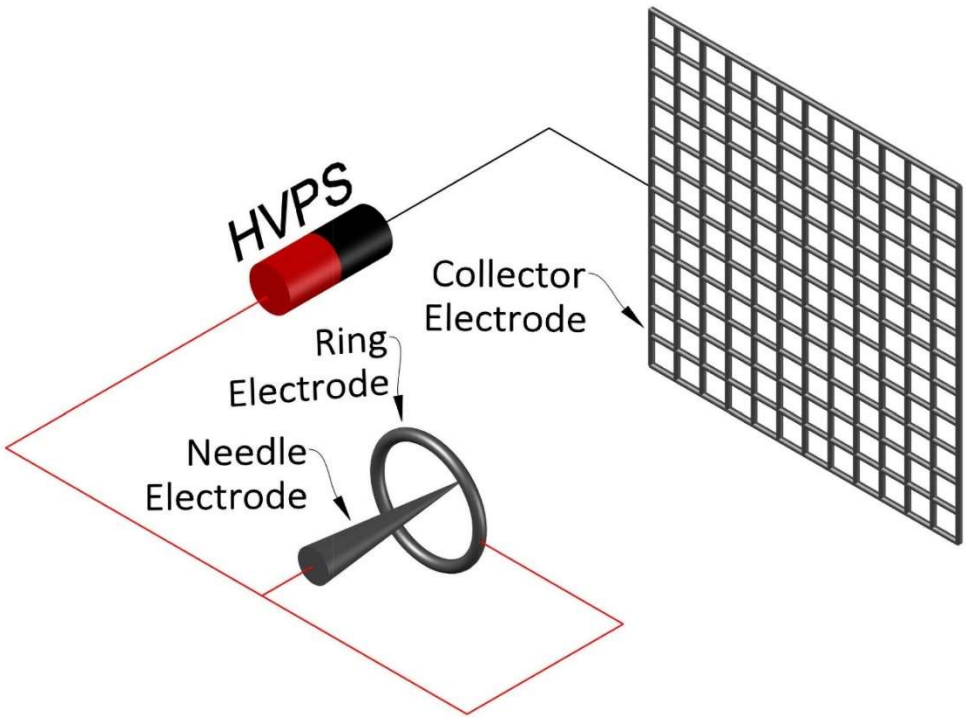

Figure 2.4. Schematic of the needle/ring to mesh experimental setup [130].

As the efficiency of EHD pumps is proportional to the velocity of any existing bulk flow [132], it was also proven that cascading EHD pumps increase not only the exit wind velocity of the EHD pump but the overall efficiency of the device as well.

Noteworthy research on needle-based emitter electrode configurations has been performed by Asano and Yatsuzuka [133], who experimentally tested the performance of multiple EHD pump geometries by using needles as the emitter electrodes and several different collector electrodes (Figure 2.5). The study gave very useful conclusions regarding the dependence of air pressure to the applied voltage and concluded that the radius of the needle is a vital factor for the overall performance of the EHD pump. Strangely however, the authors mentioned that there was no pressure creation with positive polarity during their experiments, while later research proved that not only the positive corona is capable of producing flow but it is more efficient as well, even with a similar needle-mesh electrode configuration [128].

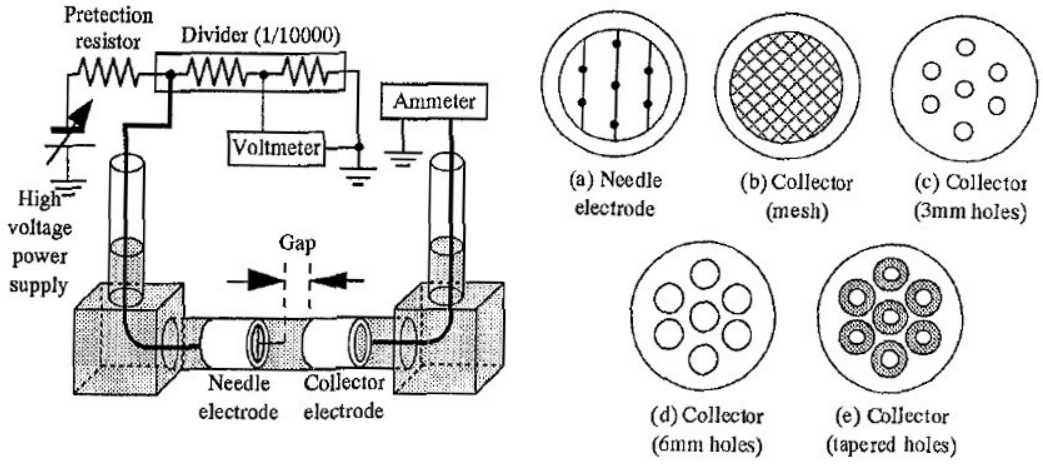

Figure 2.5. The experimental configuration and the summary of electrode configurations used to assess the needle emitter based EHD pumps [133].

A later study, assessing the effect of the voltage on the wind velocity using a needle to ring electrode configuration, displayed that the EHD pump operated properly with positive voltage applied to the emitter, reaching exit air velocities in excess of 2 m/s [134]. Future research by the same author offered further optimization of the design, which enhanced the performance of the EHD pump by implanting the collector electrode to the tube walls and also explored the performance of a cascading design for up to 7 stages [135]. The design was further enhanced by the change of the simple needle electrode to a wet porous point electrode, which the author experimentally tested to be 95% more efficient for positive corona discharges and 30% more efficient

for negative and AC corona discharges [136]. Another study has been performed to analyze the ionic wind velocity of a needle to cylinder electrode EHD gas pump [137]. However, although the study included very detailed results on the experimental design's performance and efficiency, neither the experimental setup appeared to be optimized nor any useful data on how to optimize such an electrode configuration have been disclosed. The effect of the number of stages of a multiple needle-mesh EHD pump prototype on the performance of the device has also been recently examined, indicating that an average flow velocity of 7.39 m/s is possible from a 20 mm wide experimental device with a five stage cascading configuration [138]. However, the authors also indicated that the efficiency of the design decreased as the number of stages increases [139], which is in complete contradiction with the findings of previous researchers [131].

Despite that the needle-mesh electrode configuration remained by far the most popular for years, during the past decade researchers also began exploring EHD pumps based on different electrode configurations. A mathematical model for the needle to plate EHD air pump has been developed, verified by a parallel experimental study using a needle to mesh EHD air pump, reaching an exit air velocity of 4 m/s with an applied voltage of 13 kV and suggesting that the results are similar when using either a plate or a dense mesh as a collector electrode [140]. Further experimentation with Laser-Induced Phosphorescence velocimetry revealed the profile of the ionic wind velocity of the needle to plate electrode configuration, which reached 20 m/s near the tip of the emitter electrode when the applied voltage was 10 kV [141].

A following publication, describing a multiple needle-mesh EHD pump, demonstrated that an anode voltage of higher than 26.5 kV for a 2.5 cm gap and higher than 29 kV for a 3.0 cm gap was required for the wind velocity to reach a measurable value [142]. In this particular study however no information was given regarding the energy conversion efficiency of the apparatus, electrode current, mesh size, precise electrode curvatures or even the detailed number of needles which create the emitter electrode. Apparently, the configuration was far from optimized, generating an electric field too uniform for the generation of a workable air flow, as no electro-rheological effects are observed in uniform electric fields [143]. The effect of the number of emitter electrodes on the performance of the EHD pump has been studied some years later [144], with the author seeking to optimize the number of electrodes within a rectangular flow duct but without offering a universal solution.

A plate-plate configuration has also been explored via an experimental design, with the apparatus reaching speeds of nearly 1 m/s at the end of the 170 mm long and 25 mm wide collector electrode [145]. Although the positive corona discharges were becoming more and more popular, a study of the negative corona discharge with a wire-cylinder EHD pump has also been presented, focused on the power consumption of the experimental setup; however, the conversion efficiency was very low, at about 0.138% for an approximate average exit wind speed of 1.4 m/s [146].

Even though most researchers have been investigating the performance of positive corona discharge EHD pumps, a study of the efficiency that a wire-cylinder EHD pump would have under negative corona discharge has also been studied [147]. The apparatus had a diameter of 20mm and reached a maximum air velocity of 1.7 m/s with an emitter voltage of -13kV, while it displayed higher efficiency than that of a mechanical fan of equivalent diameter.

Other studies include a saw-tooth emitter to mesh design which has been experimentally tested and optimized, finally reaching a maximum exit air velocity of 1.6 m/s with a 12 kV 1.2 kHz AC voltage applied to the emitter [148] and a wire to plate system displaying the velocity profile of EHD flow enhancers in absence of external bulk airflow [149]. A newer study took a more complex approach, examining the properties of a EHD pump (Figure 2.6) with a wire-cylinder-plate electrode configuration [150]. In this study, the emitter wire electrode of the pump was connected to a 14 kV voltage source, the middle cylinder electrodes were grounded and the collector electrodes were connected to an adjustable 0 to -8 kV adjustable voltage source. This design essentially decoupled ionization and particle acceleration, using the wire emitter for ionization and the field developed between the cylinders and the plate for acceleration. The results were positive, displaying a mechanical power increase of up to 78% and an overall efficiency increase of 0.4% (from 0.9% to 1.3%) over wire-plate configurations.

Owsenek [151] was one of the first to experiment with the direct applicability of a stand-alone EHD air pump, exploring the cooling performance of a simple needle-plane EHD pump, which increased heat transfer over free (passive) convection by 25 times. Similar studies have also been performed by Kalman and Sher [152], who reported an increased heat transfer rate of up to 250% by using a wire to planes EHD pump, and Shooshtari et al. [153], who reported an increased heat transfer rate of up to 200% by using a wire-plane EHD pump inside a confined area. A more recent

application study has also been performed, for the design of an EHD pump driving a sampling system to be installed on a vehicle to be sent to Mars, experimenting with the prototype in Earth conditions and discussing the changes which will apply on the much different environment of another planet [154].

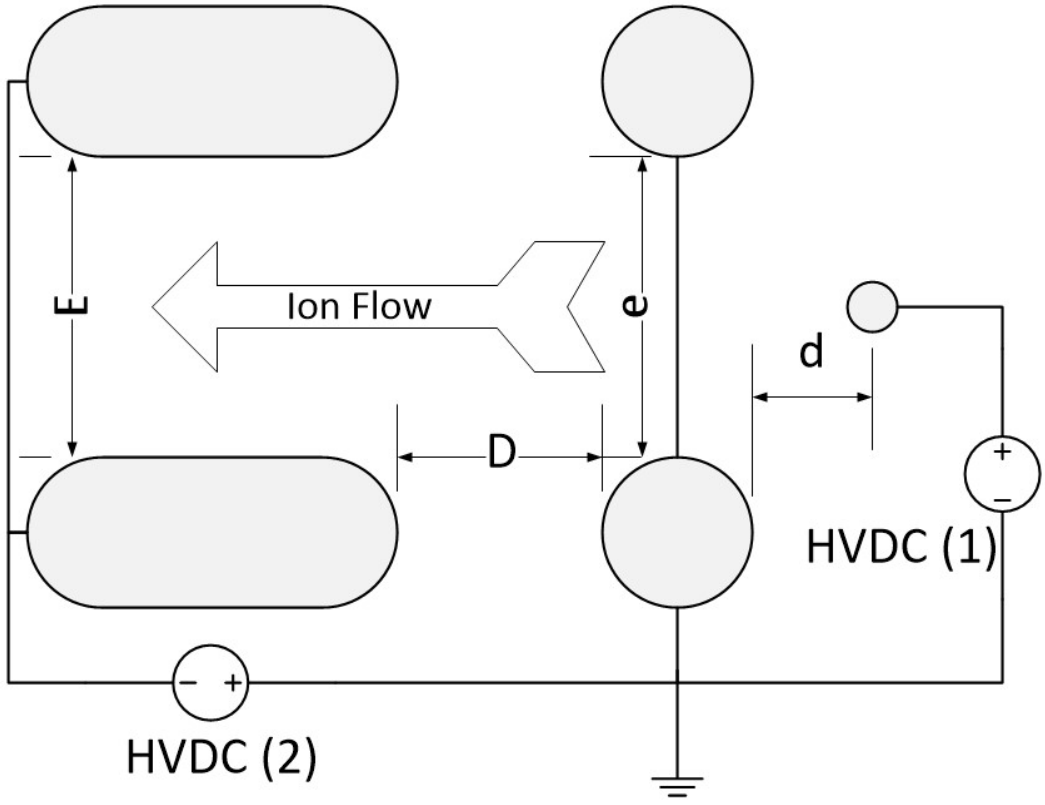

Figure 2.6. Schematic of the wire-cylinder-plate EHD pump presented by [150].

Researchers also explored a distinct advantage offered by EHD pumps; that of scaling. EHD pumps have no moving parts, therefore fabrication to a scale of μm or even lower is possible. The first to explore such a possibility was Bart [155] and other researchers soon followed [156]. The authors used opposed electrode grids and were able to pump most organic solvents. Richter and Sandmaier also described that there is a correlation between the electrode distance and the driving voltage, as well as mentioned that the stacking of several EHD micro pumps is a possibility for increased pressure. A wire-plate EHD micro pump was also presented a few years later, with the prototype reaching an air flow of up to 4 mm/s [157].

Aside from EHD air pumps, Crowley [158] was the first to publish an experimental study on the behaviour of multiple working fluids using a simple rectangular duct EHD pump with a parallel strip-strip electrode geometry (Figure 2.7). The paper listed the maximum velocity and efficiency of no less than 20 working

fluids, concluding that there are vast differences on the maximum velocity that different fluids may achieve, ranging from 0.38m/s to 6.62m/s in this particular study, as well as that the maximum efficiency is not dependent on the maximum velocity of a given fluid.

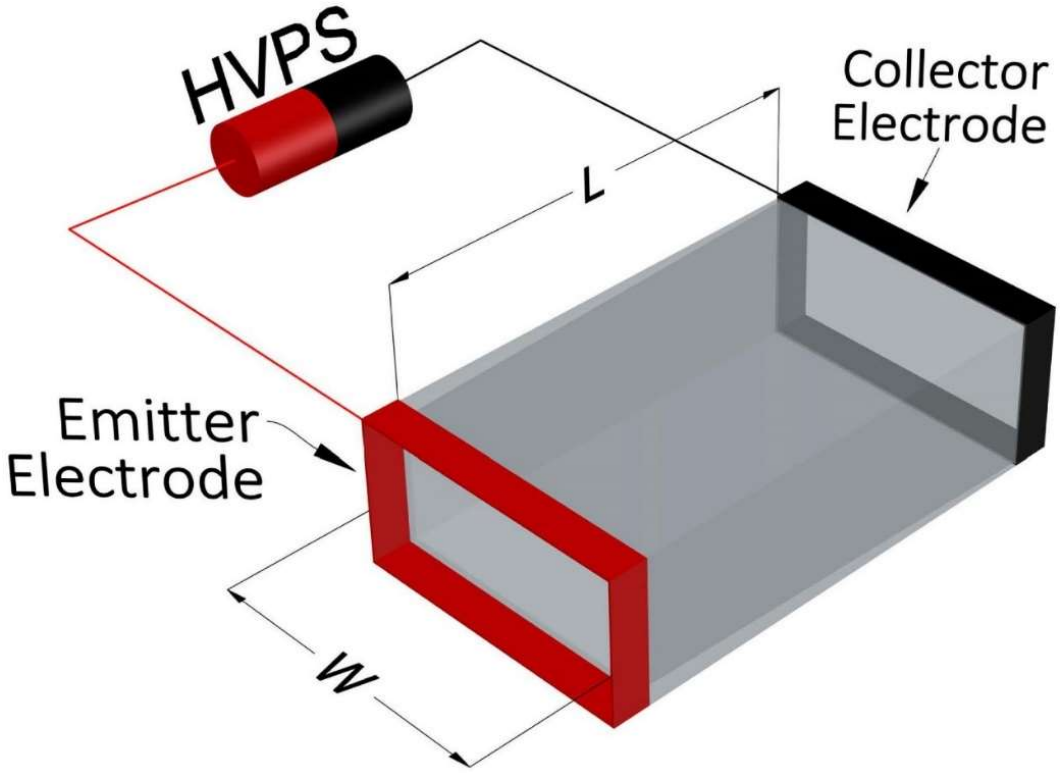

Figure 2.7. The EHD pump geometry which Crowley used to determine the properties of different working fluids [158].

Among the first studies regarding the use of a medium other than air has been performed by Sharbaugh and Walker [159], who explored the direct application of EHD pumps inside a transformer. Their results were promising but not practical, as the generated liquid flow of about 9.5 cm/s was satisfactory but the collector electrode, which also acted as a filter, was soiled by residue after a few hundred hours of operation. Many years later, a multistage EHD pump design was presented with transformer oil being the working fluid, suggesting that EHD pumps could become a practical solution for the cooling of electrical machinery [160, 161]. An experimental research using a wire-wire EHD pump has also been presented, using dielectric fluid (Dibutyl Sebacate, an organic plasticizer) as the medium, both as a single stage [162] and as a multiple stage configuration of the same geometry [163].

Fruh et al also explored the viability of pumping high conductivity fluids [164], as well as water solutions [165] and, by performing experiments with a EHD

micropump using a multiple plane to plane electrode geometry, proved that the practicality of EHD pumping is not limited to low conductivity fluids, concluding that it could have significant applications in bioscience and on chemical engineering. For application to cryogenics, an EHD micropump design using liquid nitrogen as the cooling medium has also been presented [166]. The saw tooth emitter to plane collector EHD micropump achieved a flow rate of 2.3 gr/min and a pressure head of 5 Pa with 1 kV applied to the emitter. A few years later, it received a design upgrade and the pressure head reached 13 Pa with a 50 μm electrode spacing and 1 kV applied to the emitter, while a pumping head of up to 26 Pa with 650 V applied to the emitter proved to be possible but at a reduced 20 μm electrode spacing and over twice the number of pumping stages [167].

Table **2.3** summarizes the research results on EHD air pumps to this date.

EHD pumps designed for semiconductor cooling

Even though the first fabricated and experimentally tested EHD micropump design is considered to be that of Richter and Sandmaier [156], development of EHD pumps specifically for cooling purposes began with the presentation of a micropump designed for integration in Micro Electro Mechanical Systems (MEMS) [168]. The EHD micropump was developed using laser micromachining technology and was capable of inducing a pressure head of 287 Pa with the application of 120 V over a 50 μm spacing with propanol being the working fluid. During the same period, a similar, relatively simple EHD micropump using parallel planar electrodes, was tested by another research team, using ethyl alcohol as the heat transfer working medium [169].

Another similar micropump was developed and fabricated a few years later by J. Darabi et al. [170] for the exact same purpose, using R-134a as the working fluid and capable of supplying a pressure head of 250 Pa with the application of 150 V over a 50 μm spacing. Soon afterwards, a research team led by the same author investigated the performance of different electrode geometries, comparing the performance of an EHD micropump, based on the simple parallel planar electrode design, against designs which introduced saw-tooth emitter electrodes [171]. The team derived that the saw-tooth emitter electrode design could yield a significantly higher pressure head and with a notably lower voltage applied to the emitter, reaching a pressure head of about 750 Pa with a power consumption of 4 mW and a distance of 50 μm between the electrodes, while the parallel planar electrode design required over 80 mW to reach a pressure

head of 580 Pa over the same distance. During the same year, a similar pump with HFE-7100 as the working fluid but with significantly better performance at lower voltages was presented [172].

Table 2.3. Reported performance of EHD air pump designs[1]

Author	Electrode Geometry	Velocity measurement method	Fluid velocity	Efficiency
Moreau and Touchard [128]	Needle-grid	Pitot tube 2 mm after collector electrode	8 m/s max (d=15 mm, I_d=12 μA, positive corona)	1.72% max (d=1.7 mm, I_d=12μA)
Moon et al. [130]	Needle/ring-grid	Anemometer 10 mm after collector electrode	4.54 m/s max (d=15 mm, V=+15 kV)	7.25% (d=15 mm, V=+15 kV)
Moon et al. [136]	Needle-grid	Anemometer 35 mm after collector electrode	2.75 m/s max (d=15 mm, V=-19 kV)	≈0.934% max (d=15 mm, V=+18 kV)
Kim et al. [131]	Needles-ring, 1 to 6 stages	Hot-wire anemometer 34 mm after collector electrode	1 Stage: 2.5 m/s max (V=29.8 kV) 6 Stages: 6 m/s max (V=29.8 kV)	1 Stage: 0.38% max (V=29.8 kV) 6 Stages: 0.92% max (V=29.8 kV)
Rickard et al. [134]	Needle-ring	Particle image velocimetry 3 mm after the collector electrode	1.2 m/s mean, 2.1 m/s max (d=9.5 mm, V=10.3 kV)	≈0.0245% (d=9.5mm, V=10.3 kV, I_d=71.6μA)
Nakamura and Ohyama [137]	Needle-ring	Particle image velocimetry	1.6 m/s mean (d=10 mm, V=10 kV)	≈0.0167% (d=10mm, V=10 kV, I_d=5μA)
Qiu et al. [138]	Needles-mesh, 1 to 5 stages	Anemometer 2 mm after the collector electrode	1 stage: 4.9 m/s mean (d=13mm, V=17 kV) 4 stages: 7.39 m/s mean (d=8.5mm, V=33 kV)	1 stage: ≈0.65% 4 stages: ≈0.8%
Wei et al. [139]	Needles-mesh, 1 to 33 stages	Anemometer 2 mm after the collector electrode	1 stage: 4.4 m/s mean (d=11mm, V=-13 kV) 25 stages: 16.1 m/s mean (d=11 mm, V=33 kV)	1 stage: ≈0.55% (d=11 mm, V=-9 kV) 25 stages: ≈2.2% (d=11 mm, V=-9 kV)
Zhao and Adamiak [140]	Needle-mesh	Hot wire anemometer 1.6 mm after the collector electrode	4.1 m/s max (d=20 mm, V=13 kV)	No current or power information disclosed
Karakas et al. [142]	Needles-mesh	Anemometer 50 mm after the collector electrode	1.75 m/s mean (d=30 mm, V=30 kV)	No current or power information disclosed
Zhang and Lai [144]	Wire/Needles-ring	Hot-wire anemometer 25.4 mm after the collector electrode	0.8 m/s mean (d=3.8mm, V=30 kV)	36 L/sW (V=20 kV) 4 L/sW (V=28 kV)
Komeili et al. [146]	Wire-cylinder	Hot-wire anemometer 8 mm after the collector electrode	1.9 m/s mean (V=-16 kV, d=12.6 mm)	≈0.3644% (V=-16 kV, d=12.6 mm)
Takeuchi and Yasuoka [147]	Wire-Cylinder	Hot-wire anemometer 145 mm after the collector electrode	1.7 m/s mean (V=-13 kV, d=13 mm)	≈1% max (V=-13 kV, d=13 mm)
Moon et al. [148]	Needles-grid	Anemometer 10 mm after collector electrode	1.65 m/s mean (V=12.4 kV A/C, f=1.2 kHz, d=12.6 mm)	<0.001%
Colas et al. [150]	Wire-cylinder-plate	Pitot tube 2mm after collector electrode	7m/s to 9m/s max (V=14 kV, d=3 mm)	0.9% (no secondary acceleration) 1.3% (with secondary acceleration)

[1] *Where d is the distance between the collector and emitter electrodes, I_d is the corona discharge current and V is the voltage applied to the emitter*

A further improvement of the design has been presented a few years later, with a chip-integrated cooling device capable of reaching a cooling rate up to 35 $W \times cm^{-2}$ and which could yield a static pressure of 320 Pa, but which also required a voltage of 400 V over a distance of 20 μm in order to reach those figures [173]. Another similar design for chip-integrated cooling demonstrated that a pressure head of 700 Pa with the application of 450 V over a 20 μm spacing is also possible, again with HFE-7100 as the working fluid [174].

Aside from EHD micropumps using parallel planar and saw tooth-planar electrode designs, an EHD micropump with a parallel micro-pillar electrode design has also been presented, which displayed significantly increased performance, reaching a static pressure of 620 Pa with an applied voltage of 300 V and a 40 μm distance between the electrodes [175]. A more recent study of an EHD micropump, again with parallel planar electrodes and using HFE-7100 as the working fluid, displayed that a pressure head of 268 Pa is possible with only 90 V if the emitter electrode is made of gold instead of copper [176]. The same design with a copper electrode required over twice the voltage to produce the same performance.

Darabi and Rhodes have also published a paper specifically focused on the CFD modeling of EHD micropumps [177]. The paper presented a two-dimensional numerical model of a cross section of the device, which was based on the assumptions that:

a. The flow is laminar, linear and incompressible,
b. The electrodes are planar strips on the bottom substrate,
c. There is no end effect on either side of the channel and
d. There is only one type of ion present in the liquid

The model displayed very good fit against experimental data derived from a micropump which had been previously fabricated and tested by the same author [171]; however, two-dimensional modelling is ineffective for the numerical analysis of more complex EHD micropump geometries. Table 2.4 summarizes the research results on experimentally tested EHD micropumps to this date.

Table 2.4. Summarized performance of experimentally tested EHD micropumps

Author	Working medium	Electrode Spacing	Pressure head
Richter and Sandmaier [156]	Ethanol	140 μm	600 Pa at 280 V 1250 Pa at 480 V 2480 Pa at 700 V
Wong et al. [168]	Propanol	50 μm	45 Pa at 60 V 150 Pa at 90 V 287 Pa at 120 V
Si-Hong and Yong-Kweon [169]	Ethyl alcohol	100 μm	45 Pa at 40 V 120 Pa at 70 V 245 Pa at 110 V
Darabi et al. [170]	R-134a	50 μm	40 Pa at 50 V 120 Pa at 100 V 250 Pa at 150 V
Chowdhury et al. [172]	HFE-7100	20 μm	50 Pa at 40 V 145 Pa at 80 V 190 Pa at 120 V
Chowdhury et al. [172]	HFE-7100	100 μm	45 Pa at 200 V 125 Pa at 300 V 175 Pa at 350 V
Darabi et al. [171]	HFE-7100	50 μm	Planar emitter: 100 Pa at 600 V 175 Pa at 750 V 580 Pa at 1000 V Sawtooth emitter: 50 Pa at 130 V 200 Pa at 200 V 700 Pa at 250 V
Darabi and Ekula [173]	HFE-7100	20 μm	60 Pa at 100 V 180 Pa at 250 V 320 Pa at 400 V
Benetis et al. [174]	HFE-7100	20 μm	220 Pa at 200 V 300 Pa at 300 V 660 Pa at 450 V
Benetis et al. [174]	HFE-7100	50 μm	250 Pa at 200 V 380 Pa at 300 V 600 Pa at 500 V
Lee et al. [175]	HFE-7100	40 μm	160 Pa at 150 V 250 Pa at 200 V 640 Pa at 300 V
Yu et al. [176]	HFE-7100	20 μm	120 Pa at 50 V (Au electrode) 268 Pa at 90 V (Au electrode) 230 Pa at 200 V (Cu electrode)
Zhao and Lawler [166]	LN2	50 μm	≈5 Pa at 1000 V
Foroughi et al. [167]	LN2	20 μm	22 Pa at 500 V 26 Pa at 650 V

The first experimental approach on the cooling of high power density electronic chips implementing ionic wind took place in Israel a decade ago [178], examining a wire-plates (wings) electrode configuration (Figure 2.8). The particular configuration had the advantage of being isolated from the cooled components; therefore the components would not have to be constructed from metallic materials

and would not be subject to a strong electric field. The author determined the optimal angles and dimensions (a=b=90°, θ=34.5°, H=50 mm) for this particular configuration. It was determined that the heat transfer rate has been augmented three times over the free convection heat transfer coefficient. The author also suggested that ionic wind blowers can be used for cooling electronic components and acclaimed their noiseless operation and high reliability. Unfortunately, although the author clearly mentioned that the ionic wind generator requires high power, no results regarding the electrical to mechanical energy conversion efficiency and/or power consumption of the system were presented.

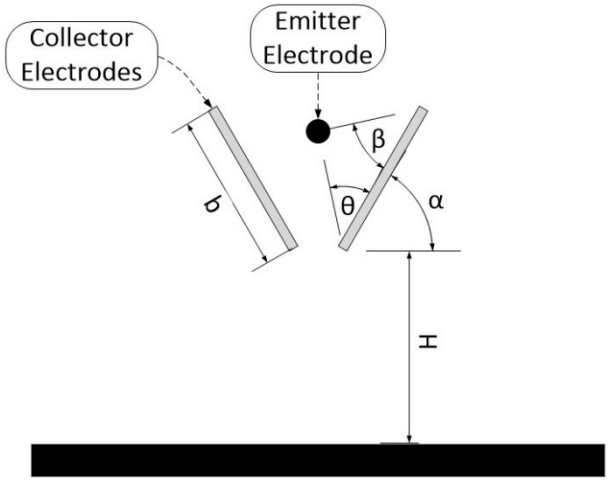

Figure 2.8. Geometry of the wire-wings electric blower [178].

Soon afterwards, a needle-vertical plate electrode design EHD air pump, designed for cooling of high power density electronic chips, was presented [179]. The authors used an experimental setup and determined several aerodynamic and key performance characteristics. Under 11 kV electrode voltage, the experimental setup managed to reach an average air velocity of about 3.0 m/s over a diameter of 60 mm and a maximum velocity of 4.1 m/s, performance figures greater than several of the mechanical blowers available at the time; however, the energy conversion efficiency was lower than 0.35 CFM/W. According to the same study, a rotary mechanical fan of similar (3.4 m/s) output velocity had an efficiency of 7.78 CFM/W, more than 22 times higher. However, the authors also determined that increasing the corona electrode voltage further had minimal impacts on efficiency, while the air velocity remained linearly dependent on the corona electrode voltage, implying that higher voltage would increase air velocity without a significant reduction of energy efficiency. In this study it was also determined that as the emitter electrode voltage

increases beyond the corona onset voltage, the collector electrode current grows exponentially which is known to reduce the efficiency of the system. The outcome of this research, in conjunction with the discovery that conversion efficiency also improves as the velocity of the air increases [132], indicates that there might be good development potential for multiple stage EHD pumps. Three years later, part of the same team published a detailed paper on how their initial model has been designed and optimized, as well as simulations and optimization techniques for EHD pumps in general [180]. Schlitz and Vishal, [181], also experimentally tested several prototypes of different electrode configurations and suggested specific designs for integration into mobile devices and general use on electronic chips. The best design presented, using multiple wires as emitter electrodes and multiple wavy fins as collector electrodes, reached an average air velocity of 1.6 m/s with a configuration allegedly compact enough to fit inside a laptop; however, the exact measurements of the device were not made known.

The first practical application of utilizing an EHD pump to cool high power density electronic components was introduced in early 2009, with an EHD pump retrofitted inside a laptop [182]. The experimental pump utilized a wire-dual plate design, with the grounded collector electrodes acting as the electronic chip heatsinks; therefore, the heat is drawn from the electronic chip on the collector electrode, which in turn is removed by the ionic wind generated by the configuration.

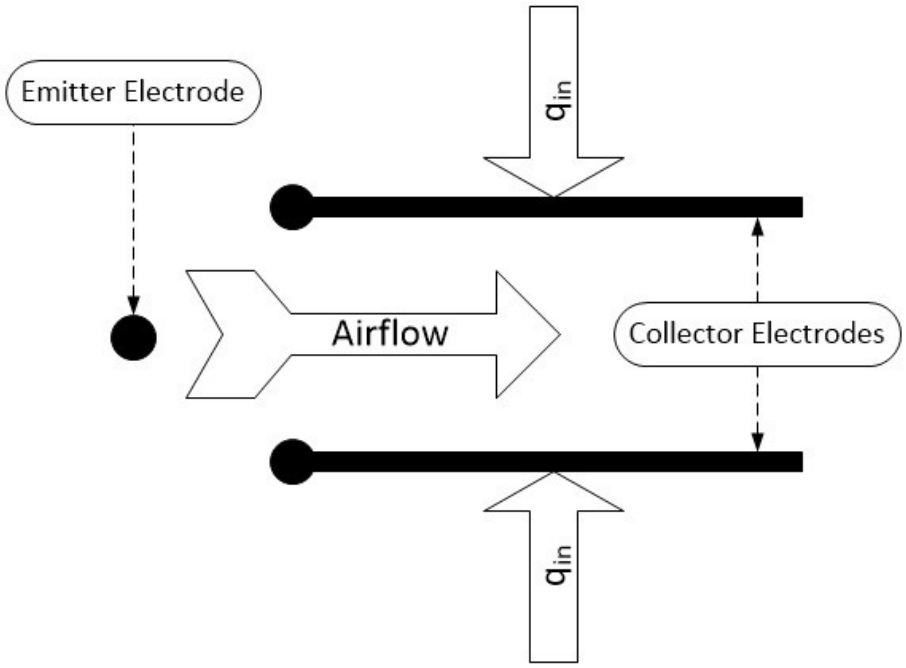

Figure 2.9. Geometry of the laptop EHD pump developed by Tessera [182].

Unfortunately, the paper did not disclose thorough experimental data, most likely because the company intended the commercialization of the design, as it can be derived from the multitude of patents which soon followed (e.g. [183-185]). The paper stated that the electronic high voltage power supply had been installed into the mechanical fan cavity alongside the EHD air pump, yet no data on the power supply specifications, voltage and/or current output and/or the electrical to mechanical energy conversion efficiency of the system was given. Only temperature comparison data between the stock mechanical fan and the EHD air pump has been shared, with the EHD air pump appearing able to deliver similar performance to that of the stock cooling fan. Since the laptop was a commercial product which had been retrofitted, the cooling system understandably was designed to optimize the performance of the stock mechanical fan. After receiving such results, the authors decided to further improve the EHD air pump by removing the constraints of fitting the EHD system inside the mechanical fan's cavity. No more information than that was given on this new design.

A similar study has been performed at the University of Purdue, assessing the possibility of exploiting the ionic wind phenomenon to help improve the cooling of smaller electronic chips, mainly used in portable platforms [77]. Although the research team emphasised their research on enhancing fluid flows generated by mechanical fans, this particular study also included performance results without an existing air stream over a wire-ribbon electrode configuration EHD pump. The experiments were conducted by heating the 14.5 cm^2 substrate with the use of a thin-film heater producing 1375 $Wm^{-2}K^{-1}$ and the study derived that the ionic wind was capable of enhancing the flow generated by a mechanical fan and decrease the temperature rise over the ambient by 2-3 °C degrees, limiting it to 28 °C degrees above ambient; however, the EHD pump alone could cool the quartz substrate and limit the temperature rise over the ambient to 40 °C without the presence of a mechanical fan, reaching a performance comparable to that of the standard fan-based cooling system. According to the research results, this experimental EHD pump was capable of cooling a chip with a Thermal Design Power (TDP) value of 2 W while draining a mere 16.4 mW.

A wire to plate EHD pump of capillary design has also been proposed for the cooling of microelectronics, with the experimental prototype, which was 35 mm tall and 17.6 mm wide, reaching a maximum exit wind speed of 1.7 m/s at 8.4 kV [186,

187]. The diameter of the pump outlet, however, was only 5mm, thus the average exit wind speed of the device may considerably degrade over larger diameters.

An EHD pump based on a rod-mesh electrode design (Figure 2.10) and making use of a negative corona discharge has also been presented recently [188].

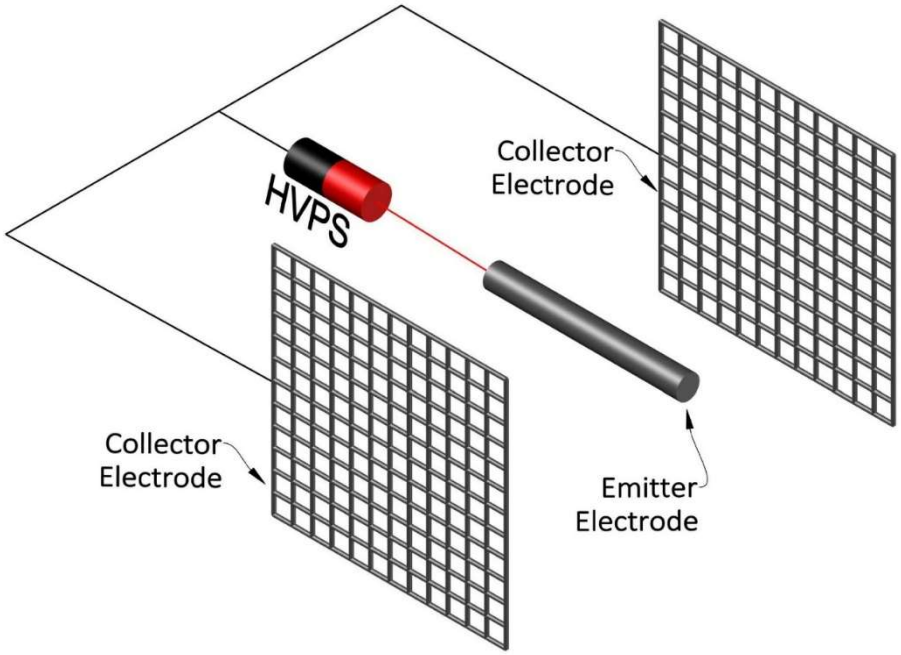

Figure 2.10. Rod-mesh electrode design presented in [188].

It was noted that positive corona gave inferior performance results with that particular configuration. After the optimization of their design, the authors noted that the experimental EHD pump reached a Coefficient of Performance (COP) of 26.5 with just -760 V but no results regarding the wind velocity have been presented.

Recently, another study examined the exploitation of multiple electrode configurations for the cooling of LEDs [189]. All of the configurations utilized a needle emitter electrode but the collector electrode was either a needle, a line (wire) or a mesh. Positive and negative coronas were also tested, with the authors indicating that a positive corona discharge is more efficient and offers better performance, even though the operational range is slightly narrower. With thermal resistance being the sole benchmarking factor, the experimental setup using a mesh collector electrode displayed the best performance, which slightly increased for smaller mesh apertures.

Only one study has been presented on reliability concerns with EHD cooling systems. A primary concern regarding EHD based cooling systems is dust, since the collector electrode displays behaviour similar to that of a high voltage electrostatic

precipitator. N.E. Jewell-Larsen et al. [190] investigated the amount and characteristics of dust collected by a novel EHD system, similar to the one the team had proposed a few years earlier for cooling laptop computers. The study concluded that the majority of the dust was collected in two locations on the collector plate, with the high percentage of large dust particles (above 10 micron) collected on the first half of the collector. Regrettably, the study itself offers no advice on how to reduce the accumulation of dust. Nevertheless, the simulations developed are valuable for investigating and optimizing the longevity of EHD pumps.

2.4 Chapter Conclusion

Today, electrohydrodynamics is rapidly evolving as a scientific discipline with immense research potential in multiple disciplinary fields. Industrially, electrohydrodynamics have practical applications in several businesses, such as in food, pharmaceutical, mechanical, space and electronic industries.

Development of EHD thrusters is still at an early stage. As they are considered to be the only currently viable solution for long-term space travel, research on EHD thrusters is mostly being performed for use in space, generally by organizations related to the exploration of space and the control of satellites. Research on atmospheric thrusters has been very slow and mostly around the “Ionocrafts” presented nearly a century ago. Advancing and improving the performance of EHD thrusters has great research headroom, especially on the control of the field geometry in order to reduce cosine losses from particle collision momentum transfers.

Significant research has been performed in order to explore the effect that EHD flows would have on the boundary layer, for both the reduction of drag and for the enhancement of heat transfer via convection. The heat transfer enhancement ratio for several working mediums has been explored; however, the number of configurations which remains unexplored is immense, as is the possibility of further augmentation via the application of AC or pulsed DC instead of simple DC voltage. Research on the possible performance enhancement that the reduction of drag could offer to specific widely-used engineering applications, such as airplanes and wind turbines, could also lead to the augmented performance and or reduced fuel consumption.

Research on EHD drying has been significant and it was proven that EHD drying can be a highly viable alternative to oven drying, especially for drying materials and food products sensitive to heat, reducing energy requirements and dramatically

enhancing the end quality of the products. However, research has almost been exclusively focused on the removal of water from the medium. There has been little to no research on the interaction of the charged particles with the biochemical substances of nutrients. Furthermore, the vast majority of the experimental studies has been performed using simple needle to plane configurations; as such, there is a large research headroom on the development of more advanced electrode configurations and or experimentally exploring the performance of electrode configurations presented in the past years. Finally, there have been virtually no studies comparing the performance of EHD dryers to RF dryers, which should also be explored.

Most of the recent research on practical devices based on the EHD effect has been focused on designing fluid accelerators (pumps), which may then be used on a wide variety of applications, the most notable of which being drying and cooling. There have been numerous experimental studies on various electrode configurations, yet there still are several configurations which ought to be explored, such as the use of AC or pulsed DC voltage and the performance of cascading electrode configurations. Due to their scaling ability, EHD pump configurations appear ideal for use in confined spaces, very small electronic devices and even as standalone on-chip cooling solutions; therefore, there also is great research opportunity on how the performance characteristics of known and or new electrode geometries scale in relation to their physical size.

Finally, the focus on experimental and empirical studies has created large gaps on the theoretical analysis of the phenomenon. With the vast majority of the proposed models being approximate and or experiential, the development of mathematical models describing at least the basic parameters of common electrode geometries appears to be of utmost priority. Based on this conclusion, this work has been focused on the development of mathematical models for the assessment of the dominant physical figures describing EHD fluid pumps (Voltage, Current and Fluid Velocity).

CHAPTER 3 - Mathematical modelling

The literature review of chapter 2 suggests that a) mathematical modelling of corona discharges and, in extend, EHD arrangements is currently insufficient and b) the vast majority of experimental EHD setups are using point-plane, cylinder-plane or cylinder-cylinder geometries. Therefore, the primary focus of this research is to contribute to the mathematical modelling of these main electrode geometries and, where possible, to expand and cover other possible electrode geometries.

As it can be seen from the governing equations described in chapter 2.2.1, the physical problem can be assessed if simple models for the electric potential V, electric field intensity E and current density j could be developed. Solutions for these figures that have been presented in the past were limited to very simple geometries, where the voltage potential can be expressed as a function of just one coordinate [18, 191], or were greatly simplified geometrically in order to reach a solution [192]. Furthermore, experimental extraction of these figures in the space surrounding voltage application electrodes is usually difficult and inaccurate due to the interference of the measuring devices with the electric field.

The following chapters present analytical mathematical models for the estimation of the electric field potential, electric field intensity and current density for cylinder-plane and twin cylinder-cylinder configurations. Furthermore, as the current density j is the most important characteristic of EHD pumps, the mathematical model has been expanded to include sphere-plane, twin sphere-sphere, point-plane and twin point-point configurations, as well as numerous electrode combinations that may be derived.

3.1 Calculation of the Electrostatic Field in Cylinder-Plane and Cylinder-Cylinder Electrode Configurations

3.1.1 Methodology

It is known that the electric field distribution around two parallel cylindrical conductors of infinite length with identical cross-sections, can be calculated by assuming the presence of two equivalent line charges of infinite length and charge densities of opposite signs $+q_l$ and $-q_l$, each placed within a conductor. Due to longitudinal symmetry, the solution of the problem can be minimized in two

dimensions, since the electric field is only depending on the distance perpendicular to the conductors, thus remaining unchanged along the longitudinal dimension. This model can be extended to solve cylinder to plane and twin cylinder to cylinder system configurations. In the case of a cylinder to plane configuration, the grounded plane can be assumed the plane of symmetry formed between two identical cylindrical conductors. Then, according to the theory of image charges [193], the problem can be solved by replacing the grounded plane with an equivalent negative image line charge -q placed eccentrically behind the plane, at equal distance to the positive line charge +q representing the cylindrical electrode, as shown in Figure 3.1.

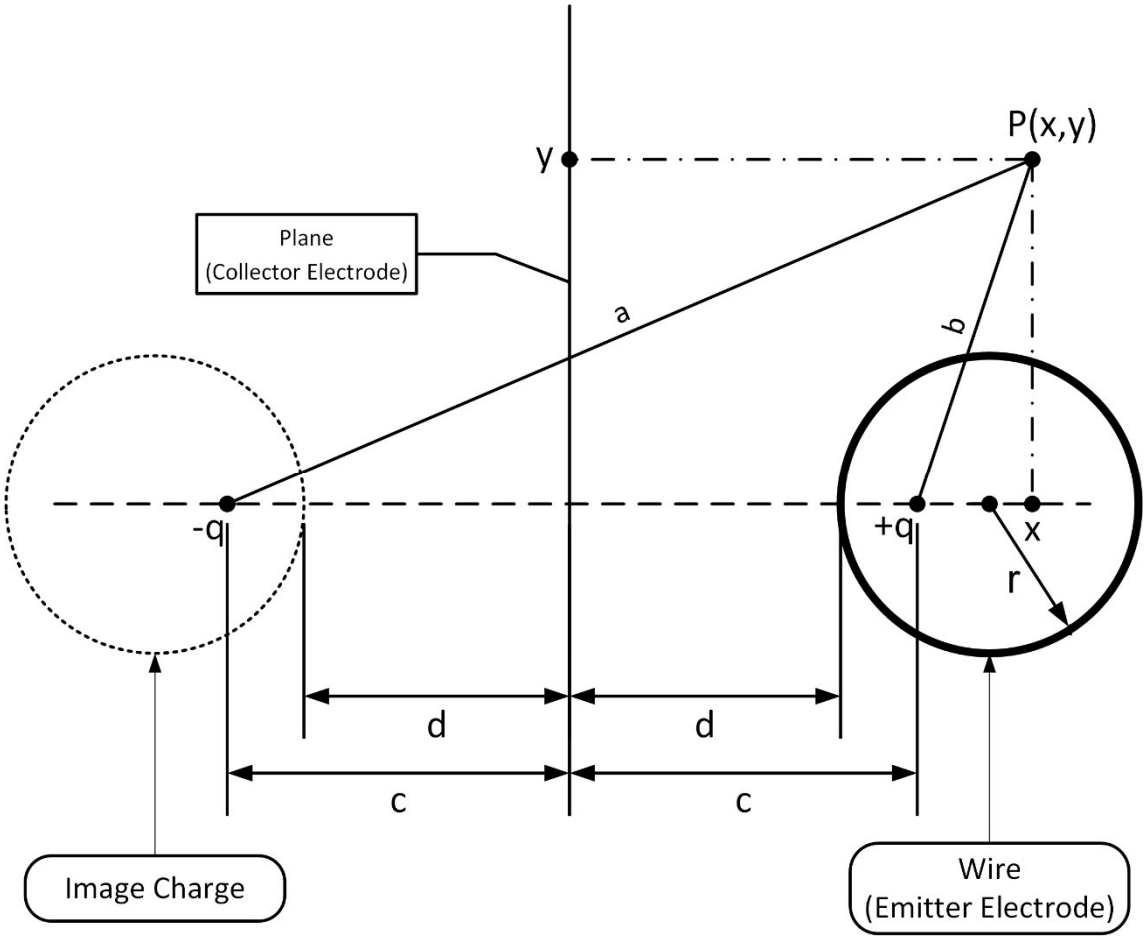

Figure 3.1. Geometrical illustration of a wire-plane configuration assuming the formation of an image charge.

Assuming air environment, the field intensity due to the presence of line charges can be found using the principle of superposition (Eq. 3.1).

$$P_{el}(x,y) = \frac{-q_l}{2\pi\varepsilon_0} \ln\left(\frac{b}{a}\right) + Z \tag{3.1}$$

Z is a constant defined from boundary conditions. For equal line charges of opposite polarity representing a wire-plane configuration, the potential at the plane should be zero (plane is grounded), therefore $Z = 0$.

On the other hand, in the case of twin cylindrical conductors, the plane of symmetry is at a voltage potential of $V/2$, where V is the voltage difference between the two electrodes. As such, the constant Z equals $V/2$.

The geometric parameters a and b can be easily found:

$$a = \sqrt{(x + c)^2 + y^2} \tag{3.2}$$

$$b = \sqrt{(x - c)^2 + y^2} \tag{3.3}$$

It can be noticed that the formation of equipotential lines in any case is a set of circles, ranging from a pair of circles with radius r, representing the equipotential surface of each cylindrical conductor, to a circle of infinite radius, practically representing a line which coincides with the plane of symmetry. The centre of those circles is always on the x axis. Therefore, the electric field intensity and the potential within the space surrounding the electrodes in the aforementioned configurations could be easily determined, provided the circle equations representing the equipotential lines are known.

3.1.2 Equipotential Lines

Assuming that:

$$A = \frac{-q_l}{2\pi\varepsilon_0} \tag{3.4}$$

and replacing Eq. 3.2, 3.3 and 3.4 into Eq. 3.1, we have that, in the case of a wire-plane configuration ($Z=0$), the equipotentials satisfy the condition:

$$\ln\left(\frac{(x - c)^2 + y^2}{(x + c)^2 + y^2}\right) = \frac{2}{A} P_{eq} \tag{3.5}$$

where P_{eq} is a number that denotes different sets of equipotentials.

Similar methodology can be applied for the determination of equipotentials in the case of two parallel cylindrical conductors (wire-wire configuration) with potential difference V. In this case we have that $Z \neq 0$ in Eq. 3.1, so 3.5 takes the following form:

$$\ln\left(\frac{(x-c)^2+y^2}{(x+c)^2+y^2}\right)=\frac{2}{A}(P_{eq}-Z) \tag{3.6}$$

Rearranging Eq. 3.5 we get:

$$\left[x-\left(\frac{1+e^{\frac{2}{A}P_{eq}}}{1-e^{\frac{2}{A}P_{eq}}}\right)c\right]^2+y^2=c^2\left(\frac{1+e^{\frac{2}{A}P_{eq}}}{1-e^{\frac{2}{A}P_{eq}}}\right)^2-c^2 \tag{3.7}$$

The previous equation shows that all equipotential lines are in fact circles, with centres lying on the *X* axis. The abscissa of the centres of different equipotentials x_{eq} and the corresponding radius r_{eq} may be given as follows:

$$x_{eq}=\left(\frac{1+e^{\frac{2}{A}P_{eq}}}{1-e^{\frac{2}{A}P_{eq}}}\right)c \tag{3.8}$$

$$r_{eq}^2=c^2\left(\frac{1+e^{\frac{2}{A}P_{eq}}}{1-e^{\frac{2}{A}P_{eq}}}\right)^2-c^2={x_0}^2-c^2 \tag{3.9}$$

Eq. 3.8 and 3.9 can be also written as:

$$x_{eq}=c\coth\left(-\frac{P_{eq}}{A}\right) \tag{3.10}$$

$$r_{eq}=\sqrt{x_0^2-c^2} \tag{3.11}$$

The above formulas define the centres and radii of equipotential lines provided the distance c between the plane of symmetry and the image line charges (Figure 3.1), as well as the magnitude *q* of the line charges, are both known.

For a twin cylinder configuration, Eq. 3.10 now becomes:

$$x_{eq}=c\coth\left(-\frac{P_{eq}-Z}{A}\right) \tag{3.12}$$

The distance c can be easily found by considering the fact that the cylindrical conductor's surface is equipotential, thus satisfying Eq. 3.10 for $r_{eq}=r$ and $x_0=d+r$. Accordingly, we get:

$$c=\sqrt{d^2+2dr} \tag{3.13}$$

Eq. 3.13 defines c as a function of the already known geometrical parameters d and r (Figure 3.1).

Now the line charge density q_l needs also to be defined. This may be done by using (3.1) for the electric potential at suitable points, $X_1(d,0)$ and $X_2(-d,0)$, on the surface of the cylindrical conductors of Figure 3.1, where the potential is already known (V and $-V$ respectively in the case of a wire-plane configuration where the grounded plane is equivalently substituted by the image charge $-q_l$ located inside the image cylinder at the left side of Figure 3.1). Substituting in (3.1) for $P_{eq}=0$ we finally get:

$$P_{el}(X1) = A\ ln\left(\frac{\sqrt{(d-c)^2}}{\sqrt{(d+c)^2}}\right) = A\ln\left(\pm\frac{d-c}{d+c}\right) \tag{3.14}$$

and:

$$P_{el}(X2) = -A\ ln\left(\frac{\sqrt{(-d-c)^2}}{\sqrt{(-d+c)^2}}\right) = -A\ln\left(\pm\frac{-d-c}{-d+c}\right) \tag{3.15}$$

where:

$$P_{el}(X1) = -P_{el}(X2) = V \tag{3.16}$$

Combining Eq. 3.16 with 3.14 and 3.15 results to four possible equation combinations. By solving them, it can be found that only one case yields an acceptable solution (the detailed solution can be read in Appendix A):

$$V = A\ln\left(\frac{c-d}{c+d}\right) \tag{3.17}$$

Substituting Eq. 3.4 in 3.17, we receive a solution for the charge q_l in the case of a wire-plane configuration, based only on known physical parameters.

$$q_l = \frac{-2\,\pi\,\varepsilon_0\,V}{\ln\left(\frac{c-d}{c+d}\right)} \tag{3.18}$$

In the case of twin cylinders, the estimation of q_l becomes:

$$q_l = \frac{-\pi\,\varepsilon_0\,V}{\ln\left(\frac{c-d}{c+d}\right)} \tag{3.19}$$

In either case, the number P_{eq} serves to specify the position of each equipotential circle. If one conductor is grounded, then the number P_{eq} defines the equipotential circle at potential $V = P_{eq}$. If the cylindrical conductors are at different potential with constant difference V, but neither of them is grounded, then the number P_{eq} defines the equipotential circle at potential $V = P_{eq}+V_{min}$ where V_{min} represents the lower potential between the two conductors. For $P_{eq}=V/2$ the equipotential circle diminishes into a line positioned midway between the conductors ($R \rightarrow \infty$).

Figure 3.2 illustrates the formation of equipotential lines of a cylinder - plane configuration for V = 1 kV, d = 5 cm and r = 0.5 cm, with a P_{eq} from 100 to 900, in steps of 100. These results were also successfully validated by comparing the output of the mathematical model to that of the FEA software.

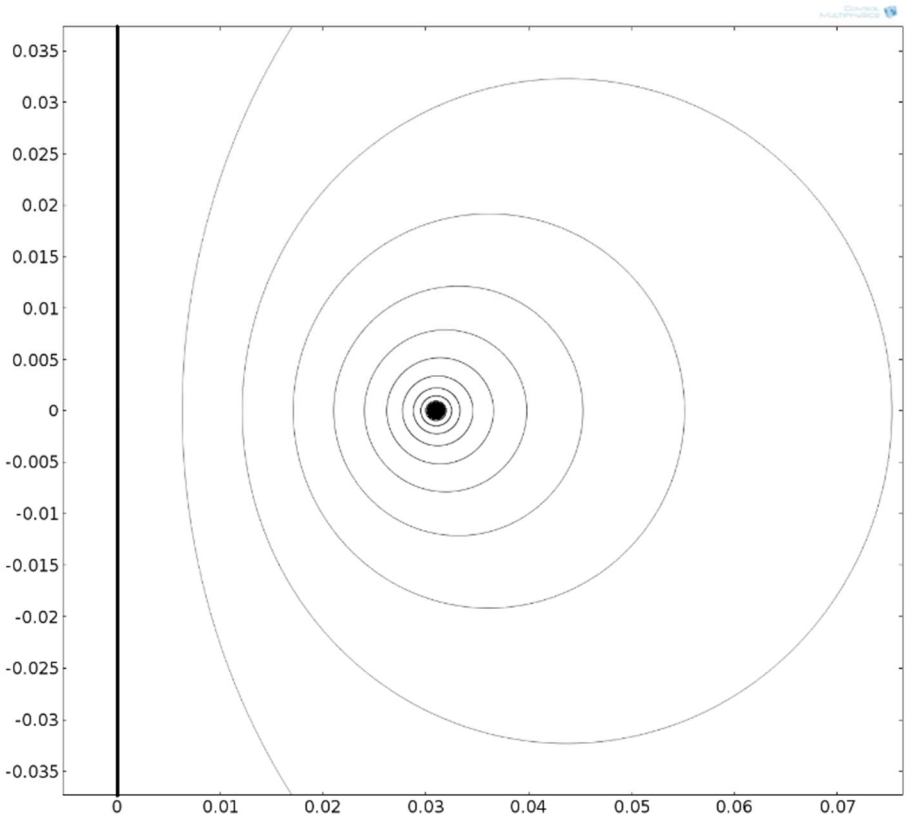

Figure 3.2. Formation of equipotential lines surrounding a cylindrical conductor facing a grounded plane electrode, for V = 1 kV, d = 3 cm and r = 0.5 cm in 100V steps.

3.1.3 Electric Field Analysis

Cylinder-plane configuration

According to the analysis presented in chapter 3.1.2 and with reference to Figure 3.1, the electric potential for a cylinder-plane electrode set, at any point with Cartesian coordinates (*x,y*), may be defined by combining Eq. 3.1, 3.2 and 3.3 as follows:

$$\begin{aligned} P_{cp}(x,y) &= A_{cp}\ \ln\left(\frac{\sqrt{(x-c)^2+y^2}}{\sqrt{(x+c)^2+y^2}}\right) \\ &= \frac{A_{cp}}{2}[\ln((x-c)^2+y^2) \\ &\quad -\ln((x+c)^2+y^2)] \end{aligned} \tag{3.20}$$

where A_{cp} is derived by combining Eq. 3.4 and 3.17:

$$A_{cp} = \frac{V}{\ln\left(\frac{c-d}{c+d}\right)} \tag{3.21}$$

The corresponding electric field strength at point (*x,y*) is defined as the gradient of potential:

$$\begin{aligned} \boldsymbol{E_{cp}(x,y)} &= -\nabla P_{cp}(x,y) \\ &= A_{cp}\left[\left[\frac{-(x-c)}{(x-c)^2+y^2}+\frac{(x+c)}{(x+c)^2+y^2}\right]\boldsymbol{i}\right. \\ &\quad \left.+\left[\frac{-y}{(x-c)^2+y^2}+\frac{y}{(x+c)^2+y^2}\right]\boldsymbol{j}\right] \end{aligned} \tag{3.22}$$

Combining Eq. 3.21 and 3.22 we finally get:

$$E_{cp}(x,y) = -\frac{V}{\ln\frac{(c-d)}{(c+d)}}\ \frac{|2c|}{\sqrt{c^4+2c^2(y^2-x^2)+x^4+y^4}} \tag{3.23}$$

Assuming that *y=0* and *x=d*, then we get the peak electric field of the geometry:

$$E_{cp\,max} = -\frac{V}{\ln\frac{(c-d)}{(c+d)}}\ \frac{2c}{c^2-d^2} \tag{3.24}$$

Expanding, the Field Enhancement Factor can be calculated by dividing the average electric field of the geometry ($E_{avg} = V/d$) with the result of Eq. 3.24. For

inhomogeneous geometries that induce corona currents, the Field Enhancement Factor will always have a value lower than 1.

Cylinder-cylinder configuration

For a cylinder-cylinder configuration, Eq. 3.20 takes the form:

$$P_{cc}(x,y) = \frac{A_{cc}}{2}[\ln((x-c)^2+y^2) - \ln((x+c)^2+y^2)] + Z \qquad (3.25)$$

where:

$$A_{cc} = \frac{V}{2\,ln\left(\frac{c-d}{c+d}\right)} \qquad (3.26)$$

The corresponding electric field strength is defined as:

$$E_{cc}(x,y) = -\frac{V}{\ln\frac{(c-d)}{(c+d)}} \frac{|c|}{\sqrt{c^4+2c^2(y^2-x^2)+x^4+y^4}} \qquad (3.27)$$

Similarly, the peak electric field of the geometry now is:

$$E_{cc\,max} = -\frac{V}{\ln\frac{(c-d)}{(c+d)}} \frac{c}{c^2-d^2} \qquad (3.28)$$

3.2 Calculation of the Unipolar Saturation Current

3.2.1 Methodology

The proposed model for the determination of the ionic unipolar saturation current is based on the estimation of the contribution of every single electric field line emerging from the emitting electrode and reaching the collector. The main complication in these cases is the treatment of the generated space charges with affect the electric field distribution. On the other hand, all different charged species which affect the total space charge distribution should be considered. Subsequently, the general equations for the space charge density and the electric discharge current are in fact nonlinear integro-differential expressions, which are very difficult to be solved even for relatively simple geometries [23]. Thereby, an approximation is made in order to simplify this complex problem; unipolar ions drifting without diffusion with constant mobility μ are considered. This is realistic in the case of electrical coronas where ionization is only confined in a small volume around the emitting electrode where the electric field is high, while, on the other hand, ions move towards the collecting electrode crossing the drift region, where the electric field is comparatively low [194]. In fact, ions coming from the ionization region are "injected" into the drift region which is characterized by Ohmic behaviour, regarding the current flow. So, assuming unipolar ions of positive polarity (positive coronas) with constant mobility μ, drifting with space charge density $\rho(t)$ versus time, we can get to the unipolar charge drift formula which is valid along any field line connecting the electrodes [192]:

$$\frac{1}{\rho(t)} - \frac{1}{\rho_0} = \frac{\mu}{\varepsilon_0}(t - t_0) \tag{3.29}$$

Where $\rho_0=\rho(t_0)$ is the charge density at the ionization zone.

Considering a single ion flow tube corresponding to such a line of length L_R, the saturation unipolar ion density $\rho_{SR}=\rho(t_0+T)$ is obtained at the line's end, at its point of incidence on the collector's surface after the drift time T required for the ions to cross the gap between the electrodes. For a given voltage drop V along the line, these ions travel along it with average velocity $\bar{v} = \mu \bar{E} = \mu V/L$, moving under the field force ($\bar{E}$ is the average field). Since ρ_0 at the ionization region is in all cases much greater than ρ we have that ρ_0-$\rho \approx \rho_0$, so substituting in Eq. 3.29:

$$\frac{1}{\rho_{L_R}} - \frac{1}{\rho_0} = \frac{\mu \cdot T}{\varepsilon_0} \quad \overset{\rho_0=0}{\Longrightarrow} \quad \rho_{L_R} = \frac{\varepsilon_0}{\mu \cdot T} \tag{3.30}$$

There is a saturation limit j_s to the unipolar drift current density along any field line of length L_R, crossing a gap of voltage V [192, 194]. As $j_s = \rho_L \cdot \bar{v}$, substituting from Eq. 3.30 we finally get:

$$j_s = \mu \, \varepsilon_0 \frac{V^2}{L^3} \tag{3.31}$$

Where μ is the average ion mobility of the fluid in the gap and ε_0 the vacuum permittivity. The average ion mobility in air is usually considered to be 1.8 - 2.2 × 10^{-4} $m^2V^{-1}s^{-1}$, with references indicating that it can be as low as 1.3 × 10^{-4} $m^2V^{-1}s^{-1}$ and as high as 2.6 × 10^{-4} $m^2V^{-1}s^{-1}$ [195-198].

In fact, the former equation represents the contribution of every single field line to the total corona drift current between the electrodes and can be used as a simplified approximation for the estimation of the current density distribution over the collecting electrode. Finally, the total corona drift current is easily estimated by integrating the current density over the whole surface of this electrode.

Field lines are perpendicular to equipotentials. These equipotential shave been previously calculated. According to their equations, they form symmetrical pairs at both sides of the plane. This means that field lines being by definition perpendicular to the equipotentials should belong to circles centred on the Y-axis. For parallel cylinder electrode configurations, the field lines can be described as arcs belonging to circles that are perpendicular to the surface of the emitter electrode and all equipotentials having their centre placed on the Y-axis. In the case of a cylinder to plane configuration, assuming a mirror symmetry, the Y-axis coincides with the surface of the collector electrode. We need a solution for X_R, which would have infinite solutions if there were no boundary conditions. By limiting the solution for an emitter electrode with its centre always on the X-axis ($y_0 = 0$) and knowing that the centre of the circles illustrating the field lines will always be on the Y-axis ($x_0 = 0$), the distance $Y_0(\varphi)$ and the radius $R(\varphi)$ of the circle corresponding to each angle φ can now be calculated. Finally, since the circle illustrating the field line is perpendicular to the surface of the emitter electrode, the angle formed at the point of the radius r is always 90°. The geometric configuration of the aforementioned problem can be seen in Figure 3.3.

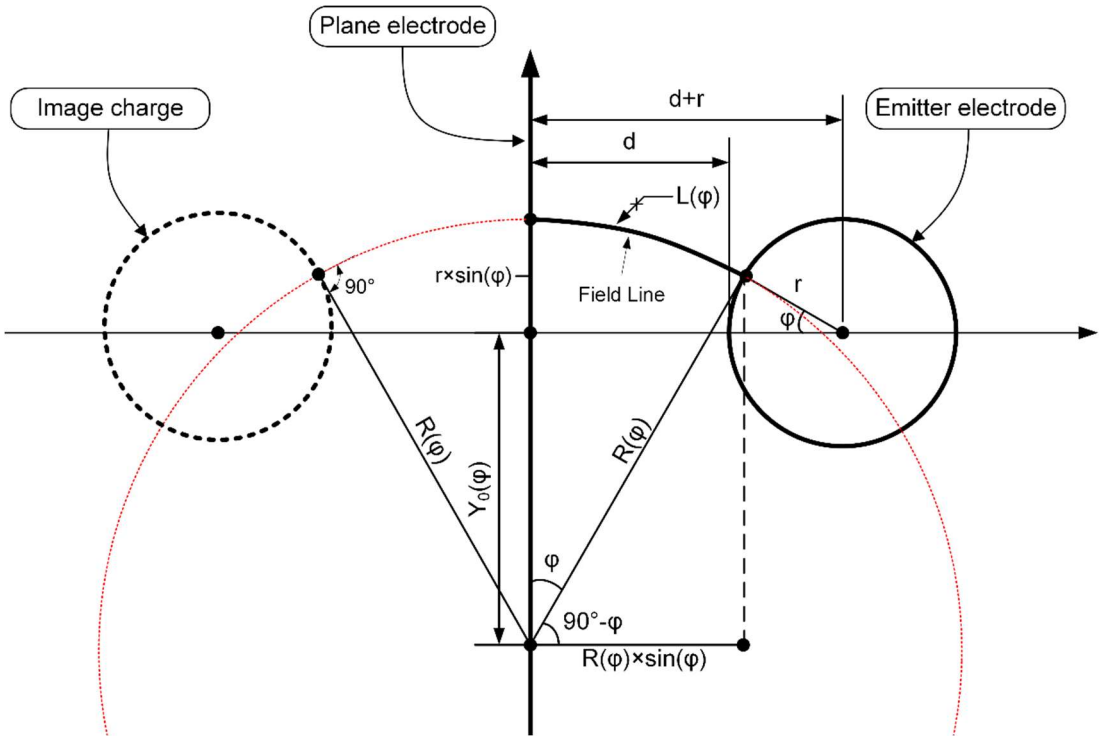

Figure 3.3. Parallel cylinders/Cylinder to plane electrode configuration, field lines formation.

3.2.2 Numerical Model

Cylinder-Plane configuration

We have that:

$$Y_0(\varphi) = R(\varphi)\cos(\varphi) - r\sin(\varphi) \tag{3.32}$$

And, solving for *R(φ)*:

$$R(\varphi) = \frac{x_0 - r\cos(\varphi)}{\sin(\varphi)} \tag{3.33}$$

Where $x_0 = d + r$.

By combining Eq. 3.32 with 3.33 and simplifying, we finally get:

$$Y_0(\varphi) = x_0\cot(\varphi) - r\,csc\,(\varphi) \tag{3.34}$$

Therefore, for any given field line emerging from the emitter with angle φ, the position of the corresponding cycle centre on the *Y* axis and its radius are known.

The arc that corresponds to the field line, from the emitter electrode to the collector electrode, for an emission angle φ in degrees, is described by the arc length L, which is equal to:

$$L(\varphi) = \frac{\varphi\,\pi}{180} R(\varphi) \tag{3.35}$$

Figure 3.4 illustrates the formation of three field lines for V = 1 kV, d = 5 cm and r = 0.5 cm, for an angle φ from 0 to 90 degrees, in 30 degree steps.

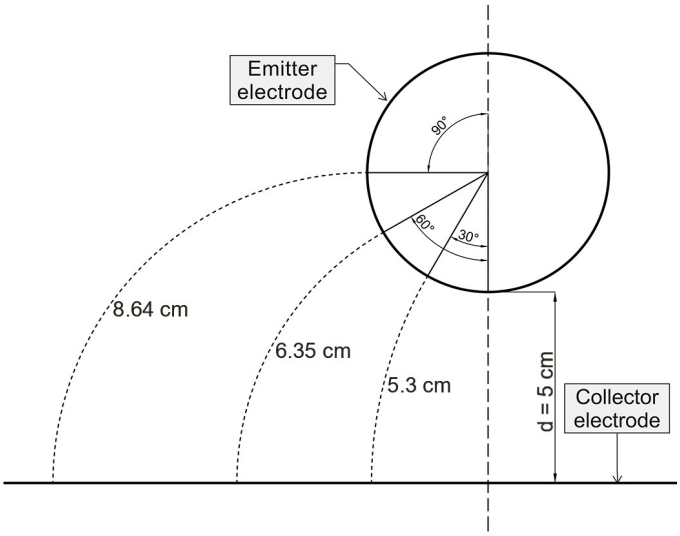

Figure 3.4. Field lines formation for V = 1 kV, d = 5 cm and r = 0.5 cm in 30° steps, up to 90°.

It can be simply proven that the arc $L(\varphi)$ is perpendicular to the surface of the electrodes and, in extend, to all of the equipotentials, by applying the Pythagorean theorem. As seen in Figure 3.5, for a field line to emit perpendicularly from the point A, we should have a right triangle with:

$$OA \perp AB \;\Rightarrow G(\varphi) = \sqrt{R(\varphi)^2 + r(\varphi)^2} = \sqrt{Y_0(\varphi)^2 + X_0(\varphi)^2} \tag{3.36}$$

It can be easily derived that $\measuredangle AOB$, formed by the tangential $R(\varphi)$ and the circle's radius, always is a right triangle and that the field line $L(\varphi)$ is perpendicular on the surface of the emitter electrode. The same stands for all of the equipotential circles formed. The full solution can be found in Appendix B.

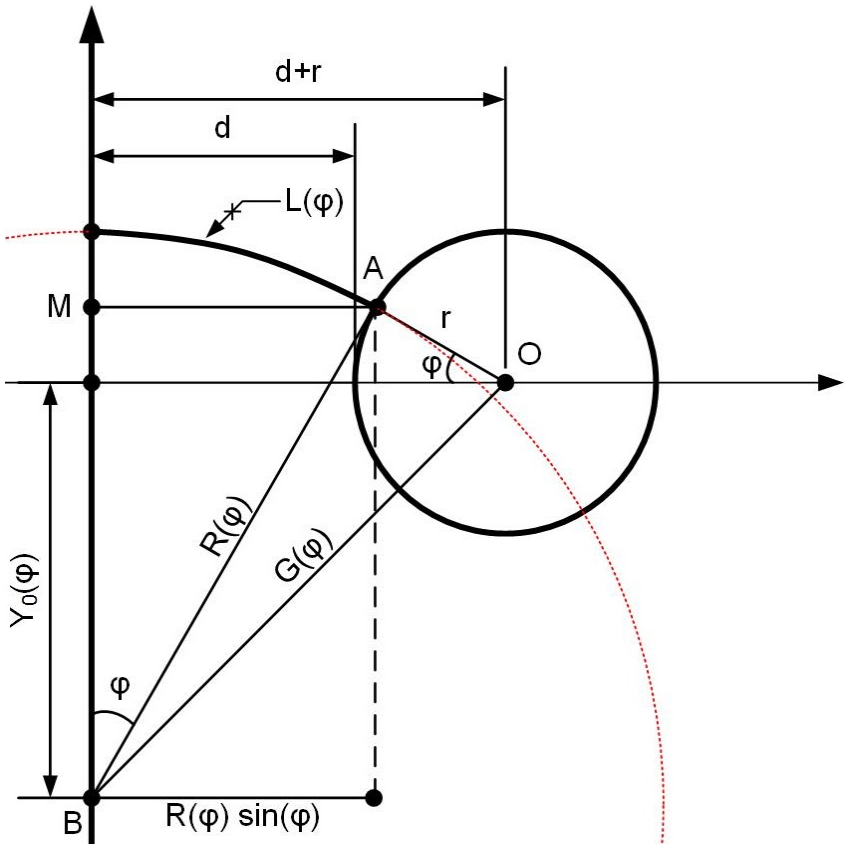

Figure 3.5. Investigation on the trajectory of the field lines on a cylinder to plane electrode configuration.

For a cylinder-plane configuration, the insertion of Eq. 3.35 into 3.31 results to:

$$j_s(\varphi) = \mu\, \varepsilon_0\, V^2 \frac{\sin^3(\varphi)}{\varphi^3 (d + r - r\cos(\varphi))^3} \left(\frac{A}{m^2}\right) \tag{3.37}$$

where φ is the field line emission angle, as seen in Figure 3.3. For this geometric arrangement, the maximum saturation current limit I_s per unit length of the emitting cylinder is equal to:

$$I_{s\,c-p} = 2\int_0^{\pi} d\Delta(\varphi)\, j_s(\varphi) d\varphi \left(\frac{A}{m}\right) \tag{3.38}$$

Where the distance $\Delta(\varphi)$ can be calculated geometrically by Eq. 3.39:

$$\Delta(\varphi) = R(\varphi) - Y_0(\varphi) = (d + 2r)\frac{(1 - cos(\varphi))}{\sin(\varphi)} \tag{3.39}$$

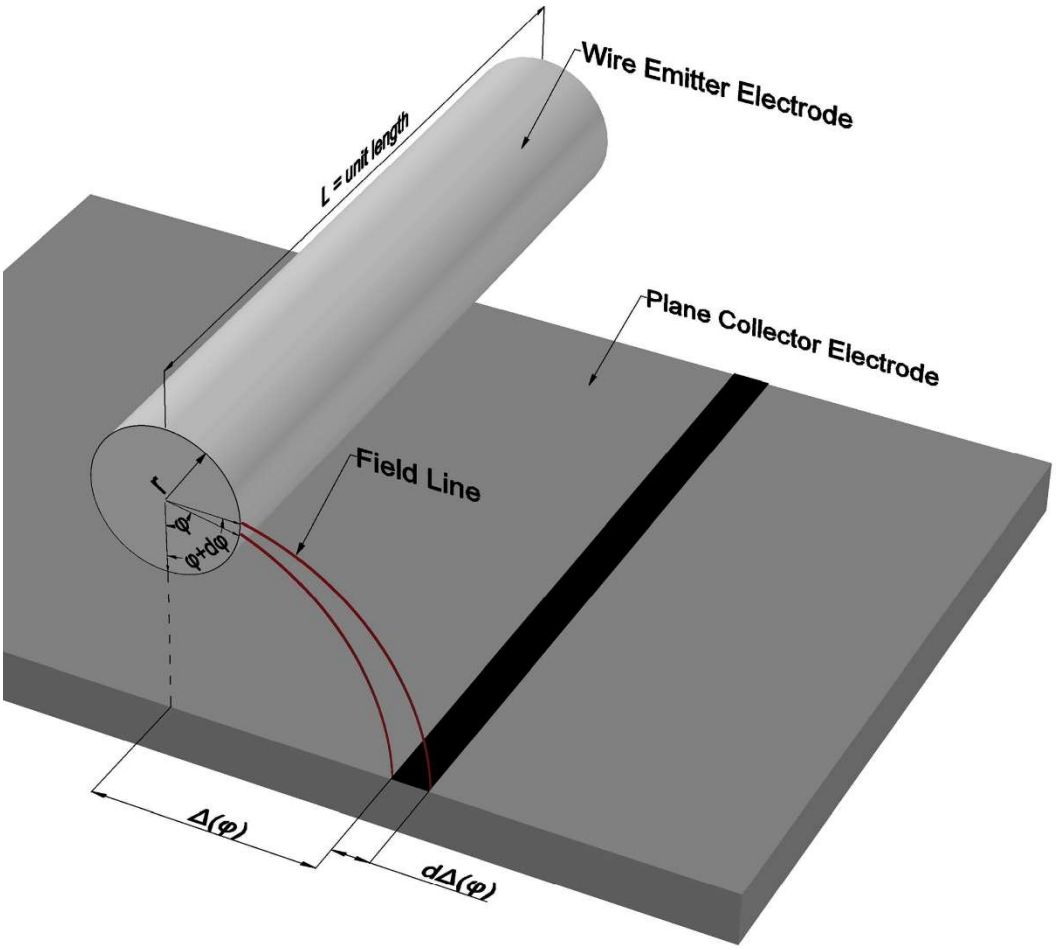

Figure 3.6. Indicative schematic, Eq 3.38.

Therefore, the unipolar saturation current limit of a cylinder-plane electrode configuration is given by Eq. 3.40.

$$I_{s\,c-p} = 2\,\mu\,\varepsilon_0\,V^2 \int_0^{\pi} \frac{d+2r}{1+\cos(\varphi)} \frac{\sin^3(\varphi)}{\varphi^3(d+r-r\cos(\varphi))^3}\,d\varphi\left(\frac{A}{m}\right) \qquad (3.40)$$

The unipolar saturation current limit I_s represents the maximum possible current flow between the electrodes, assuming that the current flow is in its entirety unipolar, i.e. during normal corona flow. There are situations, such as near the breakdown voltage of a geometry, where it is possible for the actual current to surpass the saturation current limit due to the formation of phenomena such as bipolar conduction and streamers [192].

Note that Eq. 3.40 assumes that the collecting plane electrode extends at least a distance of $\Delta(\pi)$ to either side of the emitting electrode. If the surface of the collecting electrode is smaller, then the integration can be limited to the angle φ_{max},

which is the emission angle for the field line ending at the edge of the collecting electrode. This emission angle can be easily calculated by Eq. 3.39, assuming that the maximum usable distance $\Delta(\varphi_{max})$ is known.

This concludes all the required steps to the full mathematical solution of this specific electrode geometry. Based on the same methodology, the solutions for several more electrode configurations can be easily derived as well.

Twin Cylinder-Cylinder configuration

For a twin cylinder-cylinder configuration, Eq. 3.35 is doubled. The maximum unipolar saturation current limit *Is* per unit length is now equal to:

$$I_{s\,c-c} = 2\int_0^{\pi} r\, j_s(\varphi)\, d\varphi \quad \left(\frac{A}{m}\right) \tag{3.41}$$

Consequently, the total unipolar saturation current of a twin cylinder-cylinder electrode configuration per unit length is:

$$I_{s\,c-c} = 2\,\mu\,\varepsilon_0\,V^2 \int_0^{\pi} r\,\frac{\sin^3(\varphi)}{2\,\varphi^3(d+r-r\cos(\varphi))^3}\,d\varphi\,\left(\frac{A}{m}\right) \tag{3.42}$$

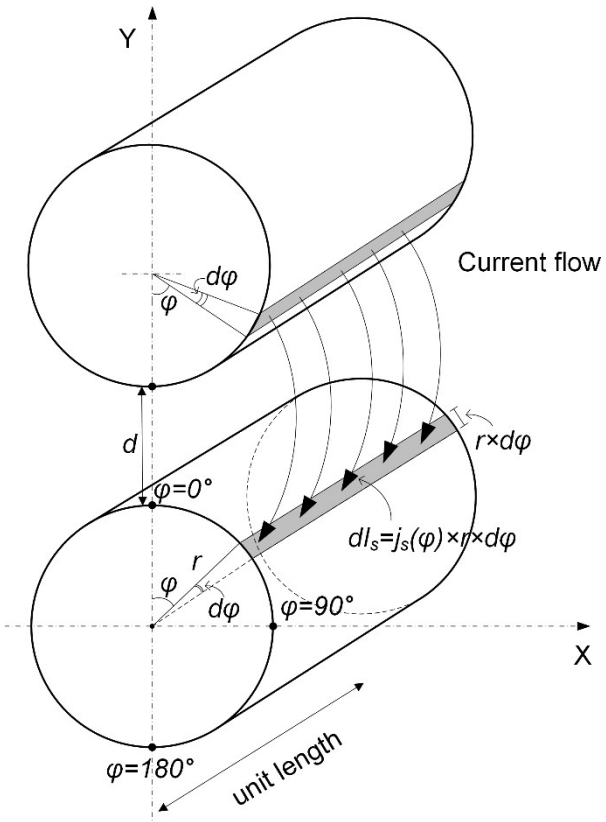

Figure 3.7. Indicative schematic, Eq. 3.41.

Sphere-Plane and Twin Sphere-Sphere Configurations

The solution of the sphere-plane and twin sphere-sphere configurations is similar to that of the corresponding cylinder-plane and twin cylinder-cylinder configurations. The mere difference is that all three dimensions of the geometry are now known, therefore the result is not expressed per unit length anymore. The maximum saturation current limit for the sphere-plane configuration is now expressed as:

$$I_{s\,s-p} = 2\,\pi \int_0^{\pi} \Delta(\varphi)\, d\Delta(\varphi)\, j_s(\varphi)\, d\varphi \quad (A) \tag{3.43}$$

By inserting Eq. 3.31 to 3.43, we have the total saturation current of a sphere-plane electrode configuration:

$$I_{s\,s-p} = 2\,\pi\,\mu\,\varepsilon_0\,V^2 \int_0^{\pi} \Delta(\varphi)\frac{d+2r}{1+\cos(\varphi)}\frac{\sin^3(\varphi)}{\varphi^3\big((d+r)-r\cos(\varphi)\big)^3}\, d\varphi\ (A) \tag{3.44}$$

Note that Eq. 3.44 assumes the collecting electrode to be a surface with an area of at least $2\,\pi\,\Delta(\pi)$. Similarly, the maximum saturation current limit for the twin sphere-sphere configuration is:

$$I_{s\,s-s} = 2\,\pi\,r \int_0^{\pi} r\, j_s(\varphi)\, d\varphi \quad (A) \tag{3.45}$$

The length of the field lines derived from Eq. 3.35 are now doubled. After the insertion of Eq. 3.31 into 3.45, we have the total saturation current of a twin sphere-sphere electrode configuration:

$$I_{s\,s-s} = 2\,\pi\,r\,\mu\,\varepsilon_0\,V^2 \int_0^{\pi} r\,\frac{\sin^3(\varphi)}{2\,\varphi^3\big((d+r)-r\cos(\varphi)\big)^3}\, d\varphi\ (A) \tag{3.46}$$

Point-Plane & Twin Point-Point Configurations

A similar model can also provide a good approximate solution with point-plane geometries. As it can be seen from Figure 3.8, by assuming that the tip of the emitting electrode is a hemisphere and that the body of the pin/needle is perpendicular to the collector electrode, then the maximum unipolar saturation current limit of the particular geometry can be described by the following simple modification of Eq. 3.40.

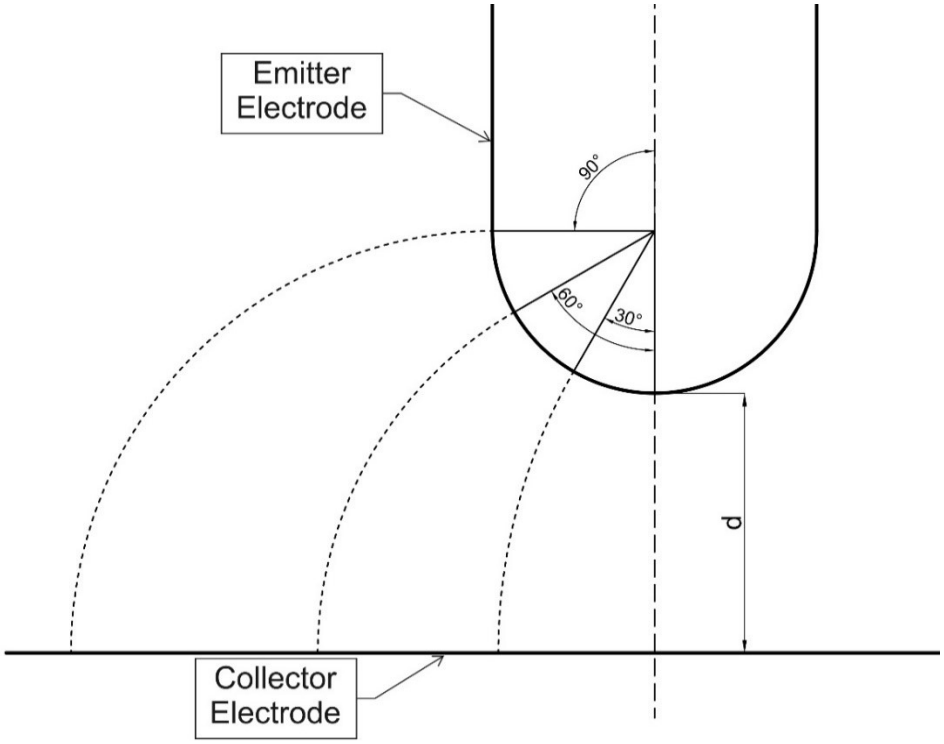

Figure 3.8. Point-Plane configuration schematic.

Sigmond developed an approximate model for this geometry in the past, assuming that the field lines are not arcs but straight lines instead [192]. Adapting Eq. 3.44 to a hemisphere, we have:

$$I_{s\,pt-p} = 2\,\pi\,\mu\,\varepsilon_0\,V^2 \int_0^{\frac{\pi}{2}} \Delta(\varphi)\frac{d+2r}{1+\cos(\varphi)}\frac{\sin^3(\varphi)}{\varphi^3\left((d+r)-r\cos(\varphi)\right)^3}\,d\varphi\ \ (A) \qquad (3.47)$$

Likewise, an approximate solution regarding the maximum saturation current limit for a twin point-point configuration can be based on Eq. 3.48.

$$I_{s\,pt-pt} = 2\,\pi\,r\,\mu\,\varepsilon_0\,V^2 \int_0^{\frac{\pi}{2}} r\,\frac{\sin^3(\varphi)}{2\,\varphi^3\left((d+r)-r\cos(\varphi)\right)^3}\,d\varphi\ \ (A) \qquad (3.48)$$

Note that Eq. 3.47 assumes that the collecting electrode is a surface of area equal or greater to the distance $\Delta\left(\frac{\pi}{2}\right)$, where the field line with an emission angle $\varphi\left(\frac{\pi}{2}\right)$ collides on the collector electrode, multiplied by 2π, forming a circular surface. If the collector electrode is smaller, the integration angles may be reduced to the emission angle φ' that corresponds to the field line reaching the edge of the

collector electrode. Again, this can be calculated through Eq. 3.39, assuming that the maximum usable distance $\Delta(\varphi')$ is known.

3.3 Calculation of the EHD Velocity Limit

3.3.1 Energy and Momentum Transport in Unipolar Coronas

The charged particle flow in atmospheric density coronas is completely viscous, dominated by the collisions between the fluid's particles [199, 200]. Fundamentally, all of the energy and momentum induced by the electric field onto the ions is transferred to the neutral gas molecules. For each ionized particle created within the ionization region, an electron will impact on the emitter and a positive ion will reach the collector electrodes respectively. Absorbing energy and momentum from the electric field, the positive ion will traverse the drift region, possibly interacting with the neutral fluid particles, transferring energy and momentum to them or attaching to them and transporting them towards the collector electrode. The relative importance of these effects can be estimated as follows [199].

The total electric energy input per ion is given by Eq. 3.49.

$$W = V\, q_{el} = 10 \text{ keV} \tag{3.49}$$

The kinetic energy limit of the drifting ion is given by the Wannier formula and is at most [201]:

$$W_i = \frac{1}{2}\left(m_g + m_i\right) V_D^2 + \frac{3}{2}\, k\, T_g \tag{3.50}$$

where m_g, m_i respectively are the gas and ion molecular masses, T_g is the gas temperature in Kelvin and V_d is the ion drift velocity, given by Eq. 3.51.

$$V_D = \mu\, E = \left(\mu\, n_g\right)\left(\frac{E}{n_g}\right) \tag{3.51}$$

Approximating the phenomenon by a planar system, we have an average current density j_i and an average electric field of E/n_g. The force per unit volume of the fluid is given by Eq. 3.52.

$$F_e = q\, n_i E \tag{3.52}$$

Therefore, the acceleration is:

$$a = \frac{q\, n_i E}{m_g\, n_g} \tag{3.53}$$

while the n_i is:

$$n_i = \frac{j_i}{q\, \mu\, E} \tag{3.54}$$

The time for the gas to cover the gap distance d is:

$$\mathrm{t_g} = \sqrt{2\, \frac{d}{a}} = \sqrt{\frac{2\, d\, m_g\, n_g}{q\, n_i\, E}} \tag{3.55}$$

The directed kinetic energy acquired by the gas is:

$$W_g = q\, n_i\, E\, d \tag{3.56}$$

while the energy spent by the electric field for the same time period is:

$$W = V\, j_i\, t_g = d\, E\, j_i\, t_g \tag{3.57}$$

Combining Eq. 3.54, 3.56 and 3.57, we have that:

$$\frac{W_g}{W} = \frac{q\, n_i\, E\, d}{d\, E^2 n_i\, q\, \mu\, T_g} = \frac{t_i}{t_g} = \sqrt{\frac{j_i\, d}{2\, (\mu\, n_g)^3\, \left(\frac{E}{n_g}\right)^2\, m_g}} \tag{3.58}$$

Assuming a stable unipolar point-plane corona discharge without streamers, for a discharge gap d = 10 mm, applied voltage V = 10 kV, saturation current of j_i = 40 μA/cm^2, $E/n_g \approx 40\times10^{-21}$ Vm^2, $\mu n_g \approx 5\times10^{21}$ (Vms)$^{-1}$ and $m_g = 29 \times 1.67 \times 10^{-27}$ kg:

$$\frac{W_g}{W} = 1.4\% \tag{3.59}$$

and:

$$V_D = \sqrt{2\, d\, a} = \sqrt{\frac{2\, d\, j_i}{m_g\, \mu\, n_g}} \approx 6\, \frac{m}{s} \tag{3.60}$$

Therefore, we can conclude that the bulk of the electrical energy input causing a unipolar corona discharge goes to fluid heating, as the positive ions cannot excite

neutral particles in the low field drift region. Only a small fraction goes into directed gas motion.

3.3.2 Current-based Empirical Models

The first expression of the ionic wind velocity was derived by Robinson [126]. His model is expressed by Eq. 3.61:

$$V_D = K_{ge}\sqrt{\frac{I}{\rho_{fd}\,\mu}}\left(\frac{m}{s}\right) \tag{3.61}$$

where ρ_{fd} is the density of the fluid in kg/m^3, K_{ge} is a function of the geometry (m$^{-1/2}$) and I is the corona discharge current in A.

From experimental data regression, cylinder to plane geometries display a fairly good fit for a geometrical function of:

$$K_{ge} = \frac{1}{\sqrt{L}} + 95 \tag{3.62}$$

More recently, Sigmond and Lagstadt evolved Robinson's model by removing the geometrical function and introducing it as a function of the discharge gap d (m) and the discharge cross section area A_{cs} (m^2) [200]. Their model is described by Eq. 3.63.

$$V_D = \sqrt{\frac{I\,d}{\rho_{fd}\,\mu\,A_{cs}}}\left(\frac{m}{s}\right) \tag{3.63}$$

However, Eq. 3.63 is not useful for arrangements where the electric field is not uniform along the axis of the gap. Considering that all efficient EHD fluid accelerators comprise of highly asymmetric geometries, it cannot be effectively used for quick or accurate assessments.

Both of these ionic wind velocity models suggest that the corona discharge current is known and that an empirical assessment of an unknown geometrical function is made. Even with the calculation of the unipolar saturation current limit via the mathematical models presented in chapter 3.1.3, the geometrical function K_{ge} demands empirical assessment. Therefore, a mathematical model allowing for the assessment of the ionic wind velocity without reliance on empirical figures is necessary for the complete modelling of the EHD fluid accelerators.

3.3.3 Proposed Space Charge Distribution Model

It is known that the ionic wind is the result of charged ions colliding with neutral air molecules and atoms as they traverse along the electric field lines, transferring their momentum via collisions. Although the ions will be neutralized once they reach the collector electrode, the neutral particles will continue their movement.

As the length and trajectory of the electric field lines for the majority of geometries used for EHD fluid accelerators is now known via the mathematical models described in 3.1.3, the EHD Velocity Limit V_D can be calculated via the space charge density distribution.

The space charge across a field line is given by Eq. 3.64 [192]:

$$\rho(t) = \frac{\varepsilon_0 \, \rho_0}{\mu \, \rho_0 \, t + \varepsilon_0} \quad \left(\frac{C}{m^3}\right) \tag{3.64}$$

where ρ_0 is the space charge density at the field line emerging point (within the ionization area), ε_0 is the dielectric permittivity of vacuum and t is the time that an ion requires to traverse a field line.

The radius of the ionization area is given by Eq. 3.65 [18]:

$$r_{ion} = r_{em} \, \delta \left(1 + \frac{0.301}{\sqrt{\delta \, r_{em}}}\right) \quad (m) \tag{3.65}$$

where r_{em} is the radius of the emitter electrode and δ is a factor depending on environmental conditions:

$$\delta = 3.92 \, \frac{P}{T} \tag{3.66}$$

where P is the pressure (cm/mg) and T is the temperature in K.

Therefore, the volume of the ionization area for cylindrical and spherical emitters is known:

$$v_i = L \, \pi \, (r_i^2 - r_w^2) \quad (m^3) \tag{3.67}$$

$$v_i = \frac{4}{3} \, \pi \, (r_i^3 - r_w^3) \quad (m^3) \tag{3.68}$$

Consequently, the space charge density within the ionization area is given by Eq. 3.69:

$$\rho_0 = v_i \, N \, e^+ \ \left(\frac{C}{m^3}\right) \tag{3.69}$$

where N is the concentration of the molecules and e^+ is the charge of each molecule for one lost electron (1.6×10^{-19} C). The concentration of molecules N can be found through bibliographical research. Loschmidt's constant is 2.6×10^{25} mol/m^3 for an ideal gas and he appears to have calculated a value of 1.81×10^{24} mol/m^3 for air [202]. Maxwell is citing a figure of 1.9×10^{25} mol/m^3 [203].

Finally, the time t that an ion requires to traverse a field line is:

$$t = \frac{L^2}{\mu \, V} \ (s) \tag{3.70}$$

If the current density is known, the ionic wind velocity at the collision point of a field line can be calculated by:

$$V_L = \sqrt{\frac{j_L \, L}{\rho_{fd} \, \mu}} \ \left(\frac{m}{s}\right) \tag{3.71}$$

where the current density j_L for a given field line is:

$$j_L = \rho_t \, \mu \, E_{av} = \rho_t \, \mu \, \frac{V}{L} \ \left(\frac{A}{m^2}\right) \tag{3.72}$$

By combining Eq. 3.71 and 3.72, we also get:

$$V_L = \sqrt{\frac{\rho_t \cdot V}{\rho_{fd}}} \ \left(\frac{m}{s}\right) \tag{3.73}$$

Hence, the EHD velocity limit at the end of each field line's trajectory can be calculated via Eq. 3.73, considering that only the spatial characteristic of the geometry, the physical characteristics of the fluid and the applied voltage are known, whereas previous models required knowledge of the corona discharge current and/or empirical - and frequently unknown - constants. Furthermore, another advantage over previous models is that the velocity limit can be found at the end of every field line and not only for the straight field line across the gap, allowing more comprehensive fluid flow calculations.

CHAPTER 4 - Experimental Investigation

The following chapters are dedicated to the experimental investigation for the verification of the mathematical models developed in the previous chapter. In order to verify the mathematical models, a wide combination of simulations and experiments were performed. Numerical simulations were performed to validate the electrostatic field model, whereas laboratory experiments were undertaken to verify the validity of the saturation corona current and the fluid velocity models. Each experimental setup and procedure is thoroughly described in their respective section.

4.1 Electrostatic Field Model

4.1.1 Experimental Configuration

In order to verify the validity of the mathematical model, the results were compared to that derived via finite element analysis (FEA), which today is the most widely accepted computational method for solving similar problems. On that purpose, COMSOL Multiphysics 4.3b has been used. Specifically, the simulations have been performed using the electrostatics module. In order to minimize any end-effects, the simulations were performed within a square boundary box of 80 cm, with the cylindrical emitter facing a 60 cm wide plane collector. The maximum simulation distance between the electrodes is 5 cm and the emitter electrode is always at the exact centre of the boundary box. Table 4.1 displays the main software settings. Figure 4.1 displays the geometric representation of one of the FEA models that are being used to simulate the system.

Table 4.1. COMSOL Multiphysics 4.3b main software settings

Mesh element size on particle trajectories	1 μm maximum
Mesh element size in air domain	50 μm maximum
Resolution of curvatures	0.005
Maximum element growth rate	1.1
Resolution of narrow regions	0.01
Solver type	Stationary, MUMPS
Solver relative tolerance	0.001
Pivot Threshold	0.1

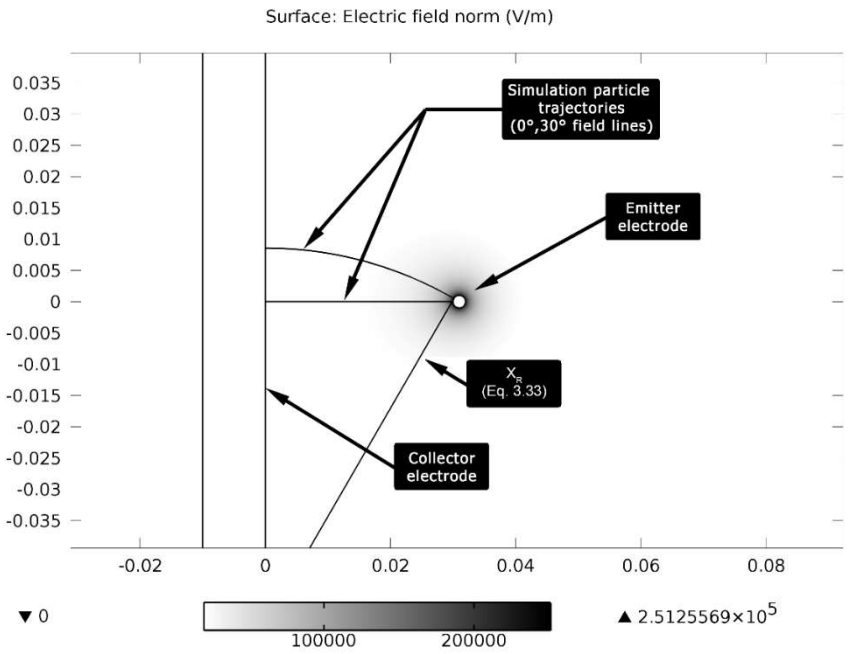

Figure 4.1. Output of a demonstrative FEA model, displaying the electric field in the space between a cylinder-plane electrodes set in air. (d = 3 cm, r = 1000μm).

To check the correlation between the results of the mathematical model and the FEA software output, three statistical functions are used. The first is the mean absolute percentage error (MAPE), described by Eq. 4.1.

$$MAPE = \left[\frac{1}{n}\sum_{i=1}^{n}\left|\frac{E_{sim} - E_{eq}}{E_{sim}}\right|\right]100\% \tag{4.1}$$

where n is the number of data points, E_{sim} is the simulated electric field strength and E_{eq} is the calculated electric field strength using the mathematical model described in chapter 3.1.3.

The second statistical function is the mean absolute deviation (MAD), shown in Eq. 4.2.

$$MAD = \frac{1}{n}\sum_{i=1}^{n}\left|E_{sim\,i} - E_{eq\,i}\right| \tag{4.2}$$

The third statistical function is the weighted-MAPE, also known as the MAD/Mean ratio, which assumes that the absolute error of each item is equally important [204]. Therefore, due to the very large scale of the electric field intensity, weighted MAPE is greatly affected by any errors very close to the top of the scale. The weighted MAPE is described by Eq. 4.3.

$$WMAPE = \left[\frac{\sum_{i=1}^{n}\left|E_{sim\,i} - E_{eq\,i}\right|}{\sum_{i=1}^{n} E_{sim\,i}}\right] 100\% \quad (4.3)$$

4.1.2 Results & Discussion

Initial testing displayed that the FEA software results would constantly get closer to the output of the proposed mathematical model as the mesh size and error tolerance decreased. This is an expected aftereffect for a valid analytical model, as the results of FEA software are naturally approximate and become more accurate as the size of the elements and the error tolerance decrease. Therefore, in order to compare the proposed mathematical model with the computed results of the FEA software, we assume that the product of the proposed mathematical model is ideal and we compare the output of the FEA software to it.

Multiple configurations of varying cylinder radius have been explored, as it can be seen from Table 4.2, which displays the MAD between the developed mathematical model and the results of the FEA software across the gap between the cylinder-plane electrode pair. Table 4.3 correspondingly displays the WMAPE error of the same configuration. To verify the validity of the mathematical model, its results across other field lines were examined as well, using the field lines trajectory model developed in chapter 3.2.2.

The trajectory of a particle leaving an emission angle φ (Figure 4.2) is inserted into the model and the electric field intensity and voltage potential results across that trajectory are being compared to that derived using the mathematical model. This trajectory coincides with the field line for an emission angle φ, which is perpendicular to both the surface of the emitter and the plane of symmetry.

Table 4.2. Electric field gradient MAD between the mathematical and simulated models, cylinder-plane configuration, $\varphi = 0°$

d (cm)	*r (μm)*			
	50	500	1000	5000
1	46.87 V/m	19.92 V/m	17.85 V/m	8.09 V/m
2	46.63 V/m	39.81 V/m	12.75 V/m	25.96 V/m
3	59.76 V/m	59.60 V/m	58.52 V/m	45.72 V/m
5	92.60 V/m	97.45 V/m	97.54 V/m	85.82 V/m

Table 4.3. Electric field gradient WMAPE between the mathematical and simulated models, cylinder-plane configuration, $\varphi = 0°$

d (cm)	*r (μm)*			
	50	500	1000	5000
1	0.046%	0.020%	0.018%	0.008%
2	0.091%	0.079%	0.025%	0.052%
3	0.176%	0.178%	0.175%	0.137%
5	0.454%	0.486%	0.487%	0.429%

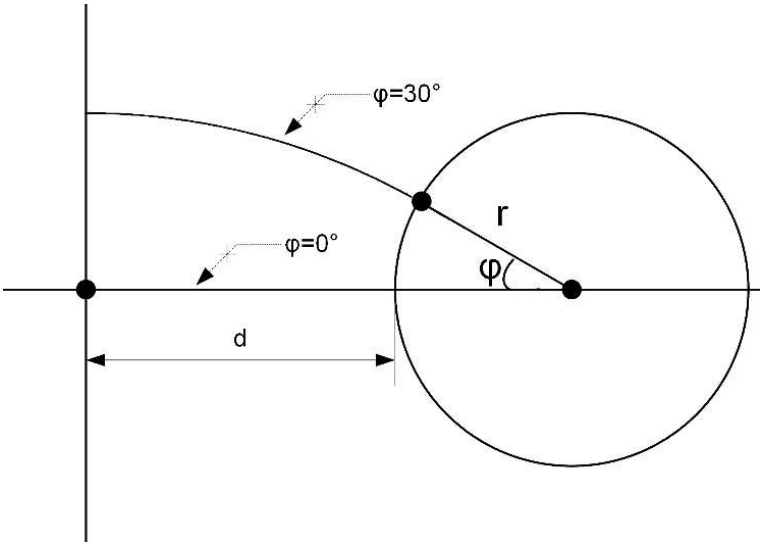

Figure 4.2. Particle trajectories (field lines) for emission angles $\varphi = 0°$ and $\varphi = 30°$

Similarly as before, Table 4.4 and Table 4.5 respectively display the MAD and the WMAPE between the presented mathematical model and the results of the FEA software across the field line for an emission angle of 30°.

Table 4.4. Electric field gradient MAD between the mathematical and simulated models, cylinder-plane configuration, $\varphi = 30°$

d (cm)	*r (μm)*			
	50	500	1000	5000
1	58.18 V/m	21.54 V/m	19.82 V/m	14.08 V/m
2	53.19 V/m	40.74 V/m	40.17 V/m	33.62 V/m
3	63.56 V/m	60.32 V/m	60.45 V/m	54.13 V/m
5	91.31 V/m	32.60 V/m	99.31 V/m	95.01 V/m

Table 4.5. Electric field gradient WMAPE between the mathematical and simulated models, cylinder-plane configuration, $\varphi = 30°$

d (cm)	*r (μm)*			
	50	500	1000	5000
1	0.060%	0.023%	0.021%	0.016%
2	0.111%	0.086%	0.085%	0.073%
3	0.198%	0.190%	0.191%	0.174%
5	0.475%	0.513%	0.521%	0.504%

Furthermore, simulations were run for cylinder - cylinder configurations as well. Table 4.6 and Table 4.7 respectively display the MAD and the WMAPE between the presented mathematical model and the results of the FEA software across the field line for an emission angle of 0°, for a cylinder-cylinder configuration. The distance d_s is the distance of each electrode from the plane of symmetry.

The MAPE error of all configurations is deliberately omitted, as it was too small and virtually incalculable for every configuration that has been tested. All of the calculated errors are minimal and caused by the computing capabilities of the software performing the calculations. For example, decreasing the solver's tolerance and or reducing the mesh element size in COMSOL Multiphysics increases the convergence between the mathematical model and the simulation results even further, yet at the substantial expense of computing time. In addition to the above, Microsoft Excel is being used for the calculation of the mathematical model. Using an arbitrary precision arithmetic calculator for the mathematical functions may increase the accuracy of the mathematical results even further, yet they will not coincide with the results of a FEA model perfectly, which are also limited by the capabilities of the software.

Table 4.6. Electric field gradient MAD between the mathematical and simulated models, cylinder-cylinder configuration, $\varphi = 0°$

d_s *(cm)*	*r (μm)*			
	50	500	1000	5000
1	18.20 V/m	2.51 V/m	2.14 V/m	0.91 V/m
2	10.54 V/m	4.63 V/m	1.46 V/m	2.93 V/m
3	9.62 V/m	6.88 V/m	6.72 V/m	5.20 V/m
5	11.62 V/m	11.36 V/m	11.34 V/m	9.88 V/m

Table 4.7. Electric field gradient WMAPE between the mathematical and simulated models, cylinder-cylinder configuration, $\varphi = 0°$

d_s (cm)	r (μm)			
	50	500	1000	5000
1	0.036%	0.005%	0.004%	0.002%
2	0.042%	0.018%	0.006%	0.012%
3	0.057%	0.041%	0.040%	0.031%
5	0.116%	0.114%	0.113%	0.099%

As mentioned in the previous section of this paper, near the end of the equipotential modelling chapter, valid P_{el} figures range from zero to V. Each number P_{el} describes a specific equipotential line, the electric potential of which is equal to P_{el}. Therefore, if the radius r of the emitter electrode, the distance d from the emitter electrode to the plane of symmetry and the potential V applied to the emitter electrode are all known, the exact formation of the equipotential lines is known as well. Figure 4.3 illustrates the formation of equipotential lines of a cylinder - plane configuration for $V = 1$ kV, $d = 5$ cm and $r = 0.5$ cm, with a P_{el} from 100 to 900, in steps of 100. These results were also successfully validated by comparing the output of the mathematical model to that of the FEA software.

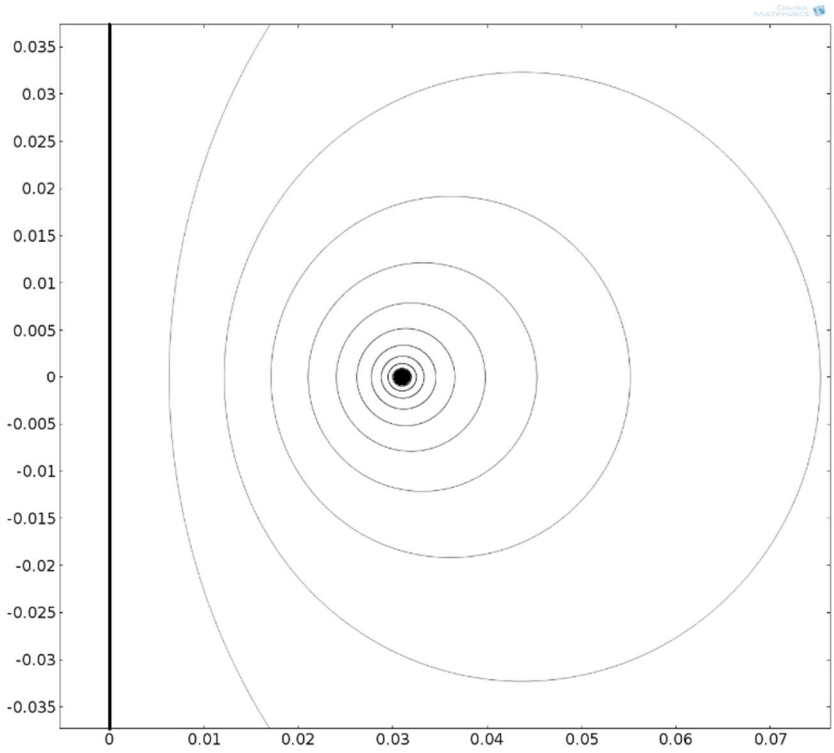

Figure 4.3. Formation of equipotential lines surrounding a cylindrical electrode facing a grounded plane electrode, for V = 1 kV, d = 3 cm and r = 0.5 cm in 100V steps.

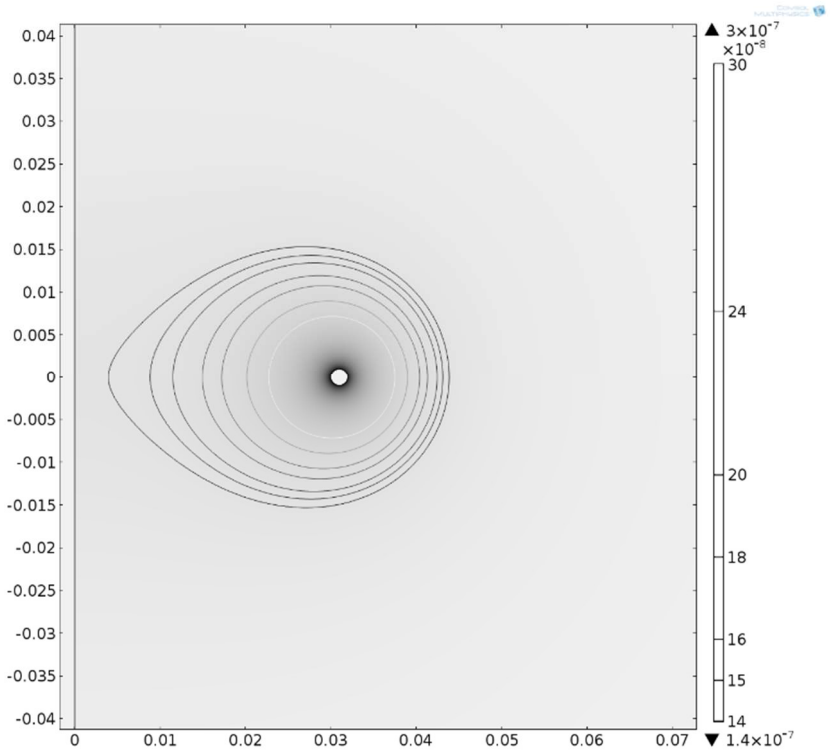

Figure 4.4. Electric Field surrounding a cylindrical electrode facing a grounded plane electrode, for V = 1 kV, d = 3 cm and r = 0.5 cm.

4.2 Unipolar Saturation Current Model

4.2.1 Experimental Configuration

In order to verify the validity of the mathematical model described in chapter 3.2, measurements have been carried out in order to specify the total corona current flowing between the electrodes at different voltage levels before breakdown occurs. Experiments are performed with a wire-plane configuration. The experimental results are to verify the proposed model for the estimation of the unipolar saturation current density. On that purpose, Ni-Cr wires of appropriate diameter are used as emitters above a flat plane collector electrode. Both the emitter and the collector electrodes are 30 cm long, while the plane collector is 58 cm wide. The corona discharge current is being measured for different distances between the electrodes (1 to 3 cm) and for various emitter electrode radiuses (30 μm to 140 μm). To ascertain that the electric field will not be disturbed, the wire emitter is secured on wooden supports and attached to a plastic tensioner. A simplified schematic of the wire-plane experimental setup is given in Figure 4.5.

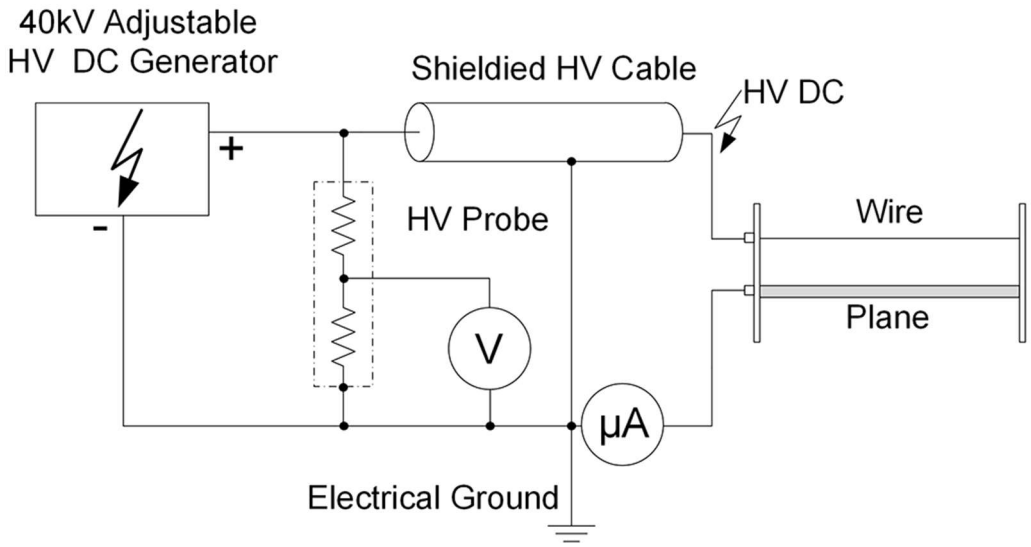

Figure 4.5. Wire-plane experimental setup for the measurement of the total corona discharge current.

The required high voltage was supplied by an adjustable high voltage power source (Matsusada Precision W Series). A voltmeter combined with a Coline HV40B 40 kV 1000:1 high voltage probe was used for measuring the DC high voltage applied to the emitter electrode, with an accuracy of 1%. Current readings (corona current) have been acquired by a high precision Thurlby 1503 ammeter with 1 nA sensitivity.

All the experiments were performed in atmospheric air, with temperature ranging from 25 to 27 °C, and relative humidity between 45 and 52 %.

For the additional validation of the mathematical model, the contribution of each field line incident on the collector electrode to the total saturation current density I_s was examined as well. For that purpose, a plane collector electrode was equipped with a thin conductive strip on its surface, electrically isolated from the remainder of the plane. The strip is movable across the length of the collector, allowing the measurement of the saturation current density for specific field lines and the assessment of the saturation current density distribution. As the height of the strip is less than 30 μm, an insignificant figure in comparison to the gap *d*, its effect on the overall electric field can be considered to be negligible. The unipolar saturation current corresponding to that strip is defined by Eq. 4.4, which represents the field lines ending on it (see theoretical analysis, chapter 3.2.2):

$$I_s = 2\,\mu\,\varepsilon_0\,V^2 L_s \int_{\varphi_1}^{\varphi_2} \frac{d+2r}{1+\cos(\varphi)}\,\frac{\sin^3(\varphi)}{\varphi^3(d+r-r\cos(\varphi))^3}\,d\varphi \quad (A) \qquad (4.4)$$

Where L_s is the length of the strip and φ_1, φ_2 are field line emission angles that land at the beginning and at the ending edge of the strip respectively. The strip is precisely 2.5 mm wide and 30 cm long. As the current going through the strip is very small, a resistor is connected between the strip and the electrical ground, with a precision Mastech MS8218 voltmeter measuring the voltage drop. Figure 4.6 displays a graphical representation of the experimental setup.

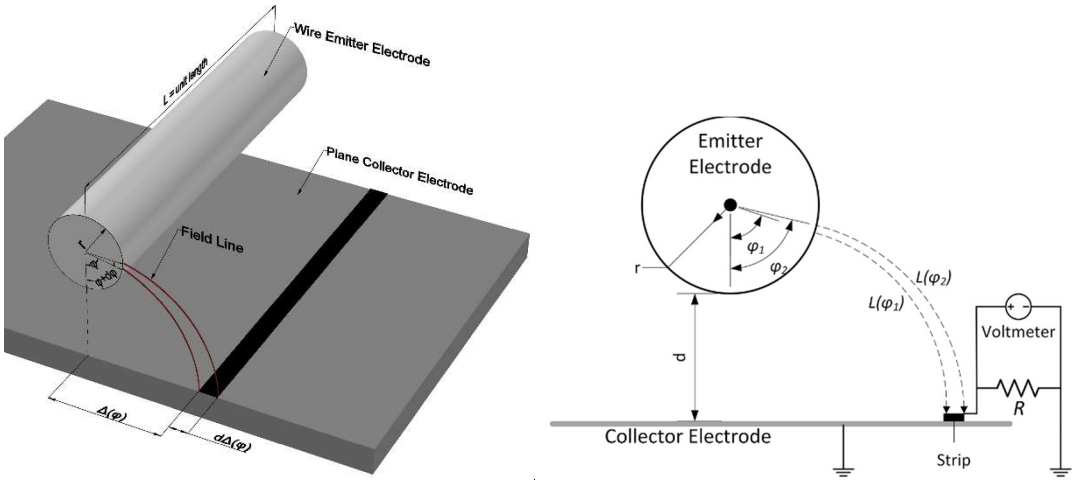

Figure 4.6. Graphical representation of the wire-plane strip experimental model.

4.2.2 Results & Discussion

Full Plane Saturation Current Limit

As the value of the ion mobility μ in air varies in bibliography, we demonstrate the saturation current density limit as an area formed by the results calculated with an ion mobility between 1.8×10^{-4} $m^2V^{-1}s^{-1}$ and 2.2×10^{-4} $m^2V^{-1}s^{-1}$, which are the most widely used values for air [195, 196].

As it can be seen in Figure 4.7 and Figure 4.8, the corona current tends to approach and or slightly exceed the saturation current limit near the breakdown point of the geometry. This is the natural development of the phenomenon, as the ionic drift region outside the ionization region acts as an impedance and is what gives the corona discharge its characteristic intrinsic stability [205].

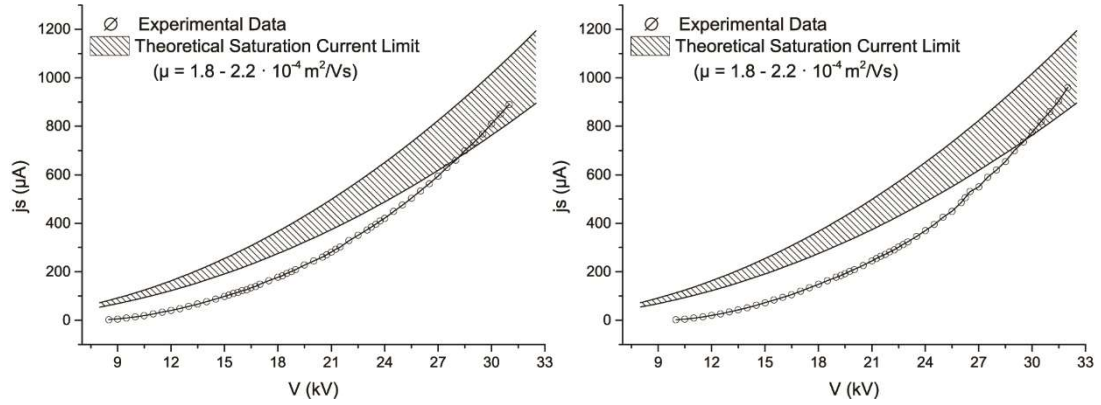

Figure 4.7. Comparison between the corona current and the calculated saturation current limit for d = 3 cm, r = 100 μm (left) and d = 3 cm, r = 140 μm (right).

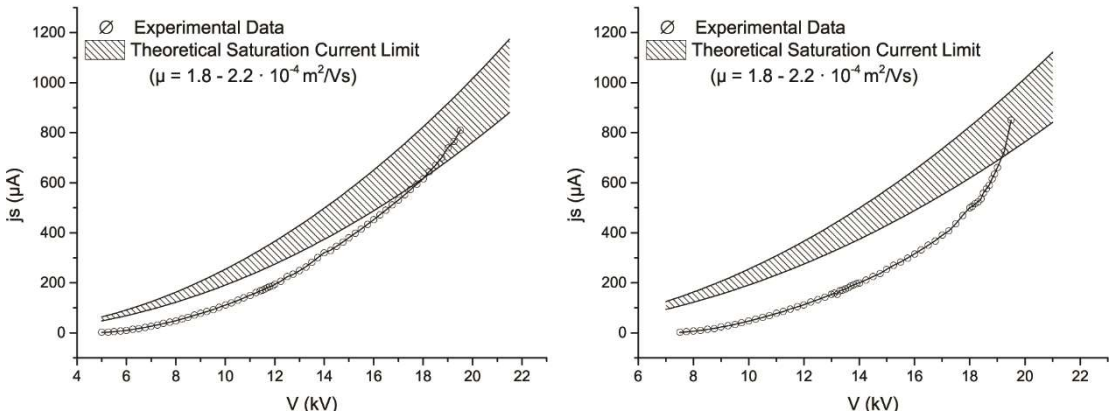

Figure 4.8. Comparison between the corona current and the calculated saturation current limit for d = 2 cm, r = 40 μm (left) and d = 2 cm, r = 100 μm (right).

For formations with a very small electrode gap d, the saturation current limit tends to be considerably higher than the actual corona current (Figure 4.9). On the contrary, Figure 4.10 depicts that configurations with large gaps but very small electrode radius can result to a corona current higher than the unipolar saturation current limit.

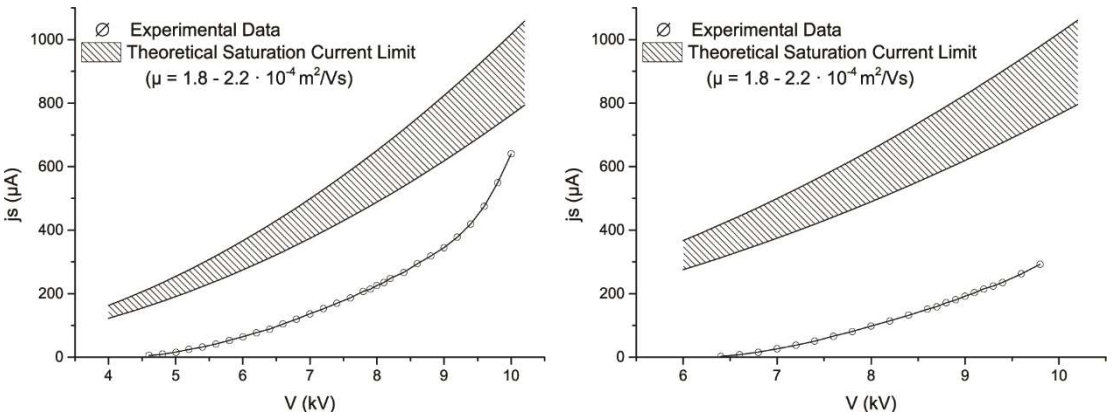

Figure 4.9. Comparison between the corona current and the calculated saturation current limit for d = 1 cm, r = 40 μm (left) and d = 1 cm, r = 100 μm (right).

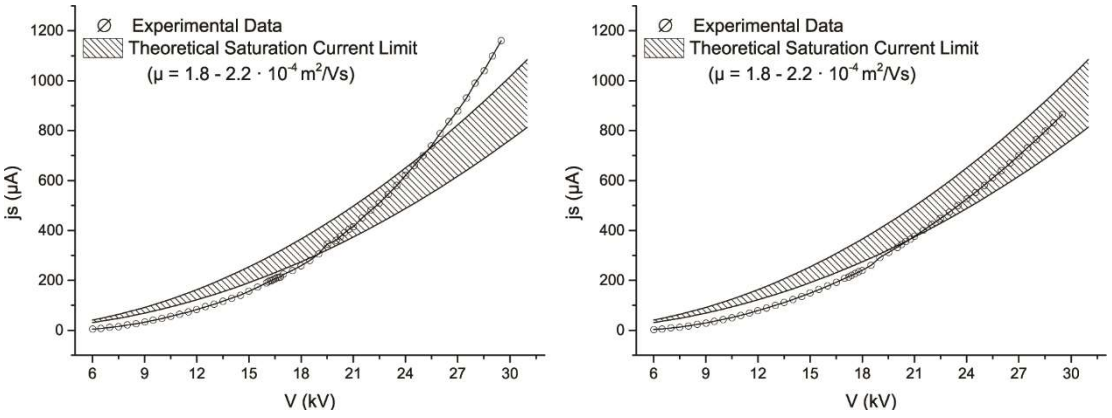

Figure 4.10. Comparison between the corona current and the calculated saturation current limit for d = 3 cm, r = 30 μm (left) and d = 3 cm, r = 40 μm (right).

Corona currents are strongly dependent on the electric field strength [18, 205]. Therefore, higher electric field strengths are naturally expected to generate greater corona currents. However, in the case of Figure 4.9, the high electric field strength and relatively small ionic drift region in the space between the electrodes creates a situation where the corona discharge loses its stability and results to a breakdown long before saturation can be achieved. This effect becomes more apparent as the radius of the

emitter increases, which results to higher saturation current limits due to the large theoretical drift region formed by the long field lines, yet the short space and very strong electric field within the space directly between the electrodes ($\varphi = 0°$) brings the geometry to breakdown far before high corona currents may be realized. On the other hand, larger gaps and very small electrode radii are expected to generate high corona currents. Assisted by the high impedance of the now expanded drift region between the electrodes, the emitter's voltage can be increased while maintaining fair corona current flow stability. In this case, the strong electric field and high inhomogeneity affecting the space between the electrodes may result to ions with higher mobility than anticipated, as well as to the formation of bipolar conduction phenomena (e.g. streamers), producing corona currents higher than the anticipated unipolar conduction limit [192, 205, 206].

Strip Saturation Current Limit Distribution

This section examines the corona current flow through narrow (2.5 mm) sections of a plane collector. Due to the very small currents that need to be measured, a resistor is added between the strip and the electrical ground. By measuring the voltage drop across the resistor, the exact current can be calculated. In order to verify the validity of this procedure, we performed a set of tests for a geometrical configuration that natively produces a current high enough for our high precision ammeter to measure, comparing the results of the direct current reading to those of converted voltage readings across several resistors. The results can be seen in Figure 4.11. In summary, there was virtually no error between the reading of the ammeter and the calculated current via the voltage drop across most of the resistors. The only configuration that stood apart from the others is the one making use of a 1.04 kΩ resistor, which generated very low voltage readings (1 - 63 mV) and thus the accuracy was limited by the capabilities of the voltage meter.

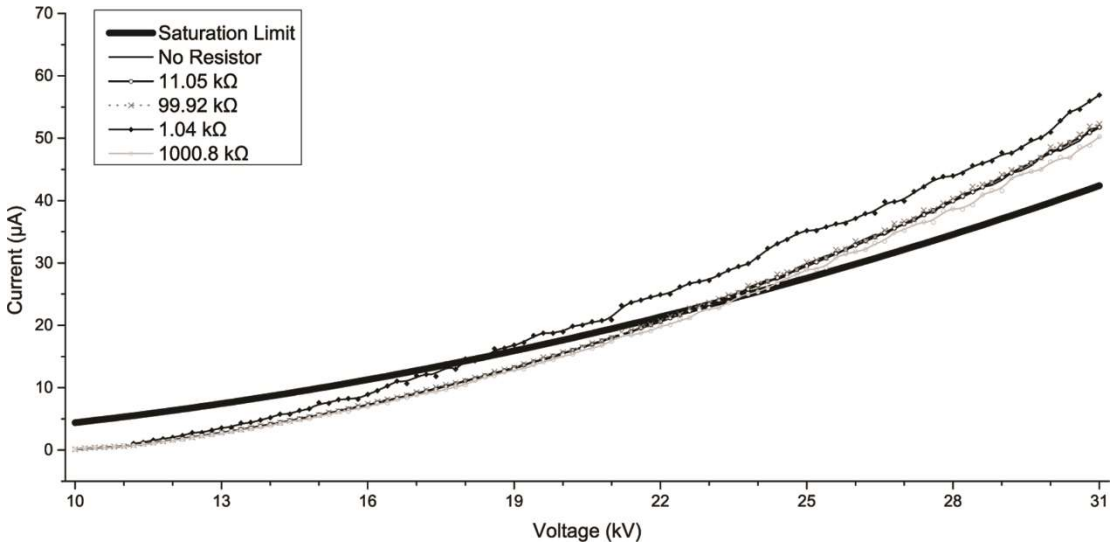

Figure 4.11. Theoretical saturation current limit and measured corona current via different resistors on a 2.5 mm strip for d = 3 cm, r = 140 μm (φ_1 = 0°, φ_2 = 9.45°).

Generally and as depicted in Figure 4.12, the corona current is greater for a given distance d and voltage V as the radius of the emitter decreases. This is in good agreement with the known theory of corona discharge, as the stronger and more inhomogeneous electric field generates a greater current flow. Still, the relatively small radii difference of the emitter compared to the distance d results to field lines of about equal length. As a result, the normalized contribution of each field line for different radiuses r is nearly identical (Figure 4.13). The electrode gap d has a significantly greater effect on the contribution of the field lines in relation to the emission angle φ, as the length of the field lines increases significantly. As it can be seen in Figure 4.13, the greater the electrode gap is, the greater the contribution of small emission angles is. On the other hand, smaller electrode gaps reduce the contribution of large emission angles. Figure 4.14 displays the experimentally measured corona current on the strip positioned across the plane electrode for different voltages V. The distribution is closely following Warburg's distribution, which has been experimentally observed for other geometries [207, 208].

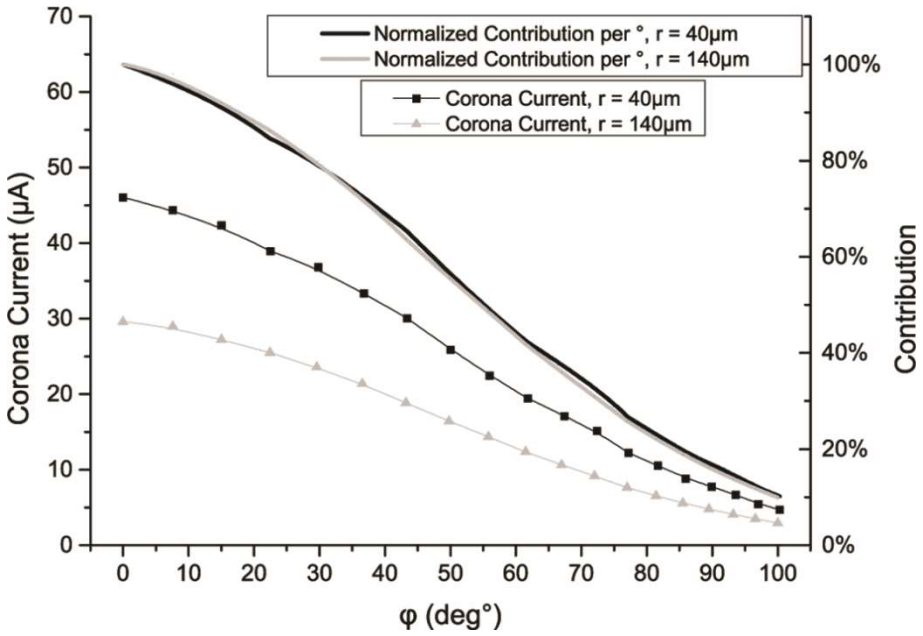

Figure 4.12. Corona current across the collector plane electrode per emission angle φ for $d = 3$ cm, $V = 25$ kV.

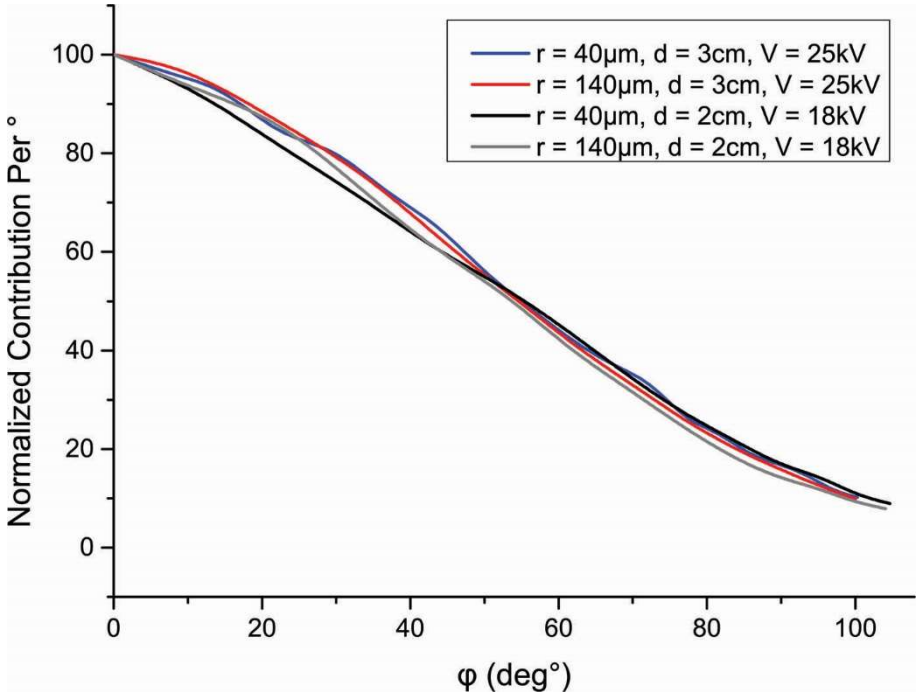

Figure 4.13. Fitted field line corona current contribution reduction in relation to the emission angle.

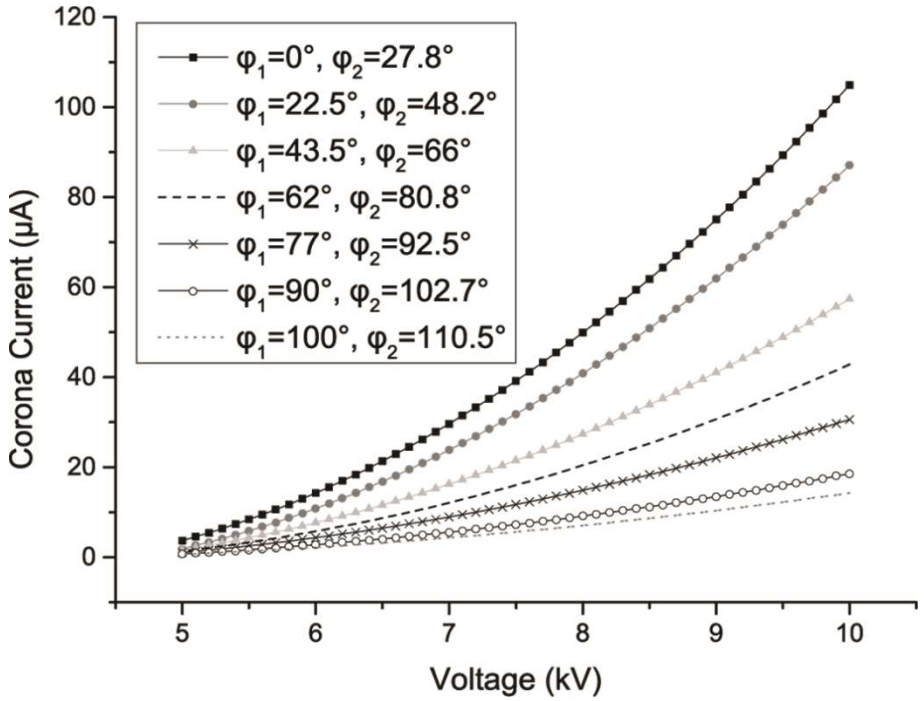

Figure 4.14. Measured corona current versus emission angle φ, for a 2.5 mm strip across the collector plane electrode for d = 3 cm, r = 140 μm.

According to theory, it is expected that field lines emanating from smaller emission angles will have a greater contribution towards the total corona current. The shorter ion flight path through the high impedance drift region and the stronger electric field between the electrodes makes it easier for higher mobility ions to appear and favours the formation of bipolar transport phenomena. This is in good agreement with the developed mathematical model and the experimental results. Figure 4.15 indicates that the majority of the total current (≈90%) is contributed by the field lines with an emission angle up to 100° and that the current distribution is virtually unaffected by the voltage.

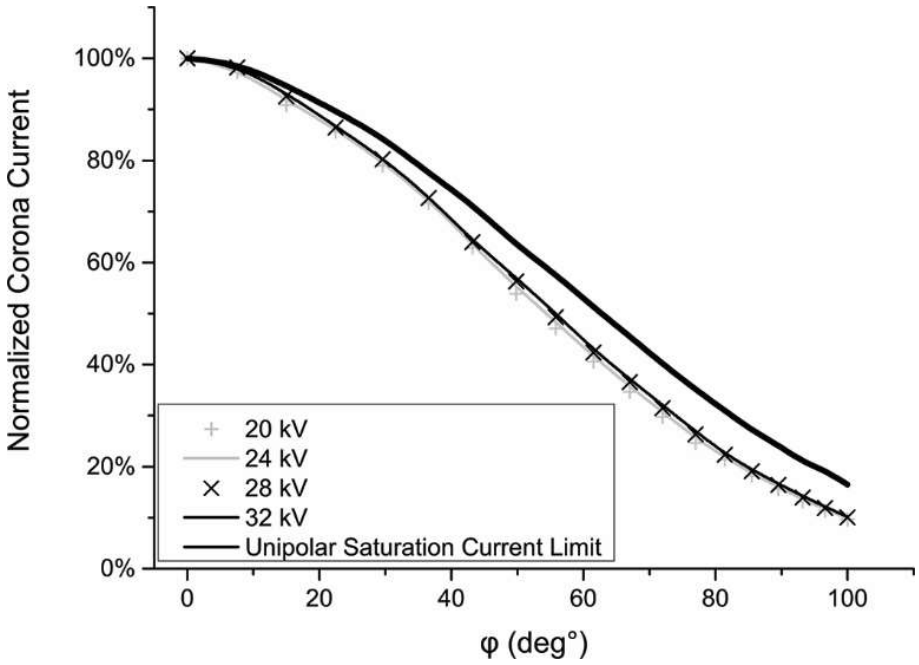

Figure 4.15. Corona current density on a plane collector electrode for varying voltage, d = 3 cm, r = 140 μm.

In comparison to the theoretical unipolar saturation current limit of the geometry, it would appear that the actual contribution to the total corona current leans towards the shorter field lines. As it can be seen in Figure 4.16, small emission angles contribute the most to the overall corona current but may also override the saturation current limit significantly before the breakdown voltage of the geometry, while large emission angles may not surpass it at all. The base reason of this is that the field lines emanated from smaller emission angles are shorter and travel through a drift region where a stronger electric field is present, while field lines emanated from greater emission angles travel through a longer drift region with greater overall impedance. The very high current with smaller emission angles at high voltages indicates the presence of free electrons and the strong formation of bipolar conduction phenomena in the space between the electrodes.

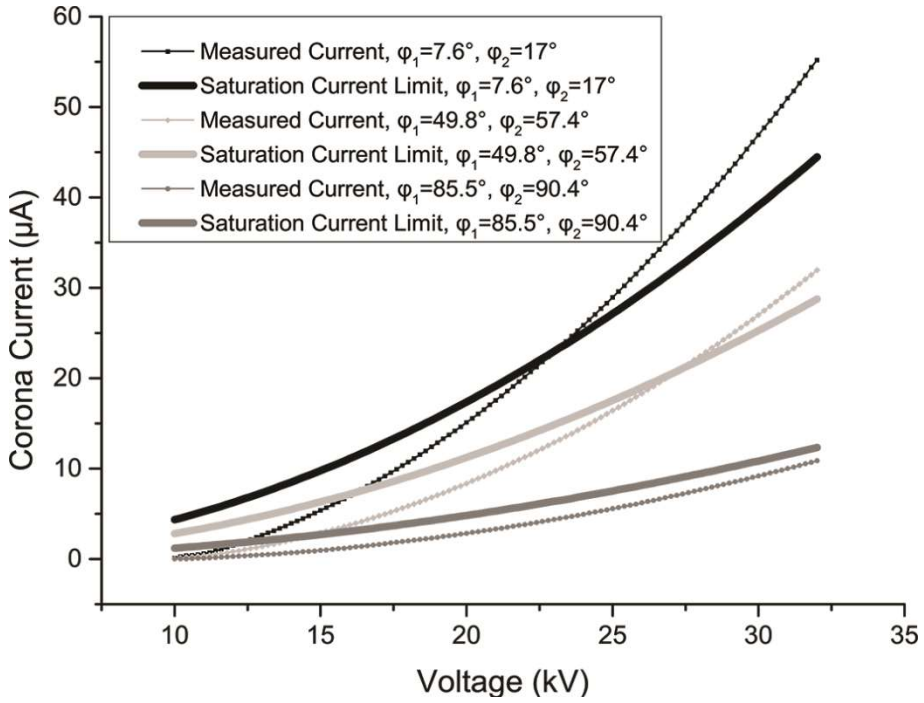

Figure 4.16. Theoretical saturation current limit and measured corona current for three different positions on a plane collector electrode. 2.5 mm strip, d = 3 cm, r = 140 μm, $\mu = 1.8 \times 10^{-4}$ m^2/(V s).

4.3 EHD Velocity Model

4.3.1 Experimental Configuration

In order to verify the validity of the developed mathematical models, experiments were performed using various wire-plane and needle-grid configurations. The wire-plane setup is used to verify the application of the model described in chapter 3.3.3 for the assessment of the maximum velocity limit. The maximum velocity will appear at the end of the shortest field line, which is emanated from φ=0° and is a straight line across the gap d.

On that purpose, Ni-Cr wires of appropriate diameter are used as emitters above a flat plane collector electrode, which has a pitot tube inserted beneath it. In this case, the maximum velocity limit of the geometry would be:

$$V_{D_{max}} = \sqrt{\frac{j_L\, d}{\rho_{fd}\, \mu}}\ \frac{m}{s} \tag{4.5}$$

The emitter and the collector electrodes are 30 cm long and the plane collector is 58 cm wide. To ascertain that the electric field will not be disturbed, the wire emitter is secured on wooden supports and attached to a plastic tensioner. The EHD velocity limit is being measured for different distances between the electrodes (1 to 3 cm) and for various emitter electrode radiuses (30 μm to 140 μm).

A simplified schematic of the experimental setup is given in Figure 4.17. An opening of 2.6 mm, exactly the radius of the tube's point, is drilled on the surface of the plane electrode directly beneath the emitter wire, at the exact centre of the collector. Figure 4.18 displays an indicative 3D illustration of the wire-plane geometry.

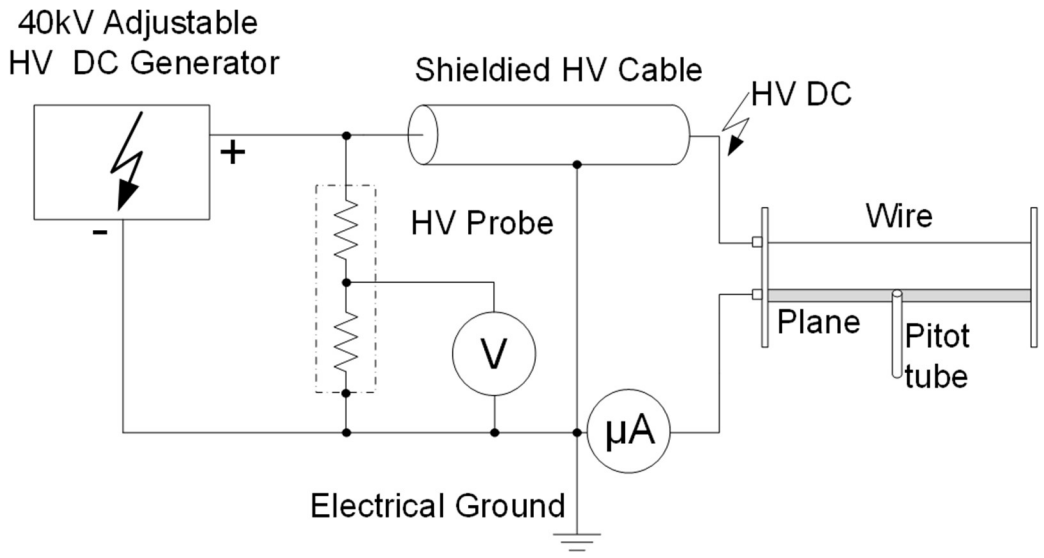

Figure 4.17. Wire-plane experimental setup for the assessment of the EHD velocity limit.

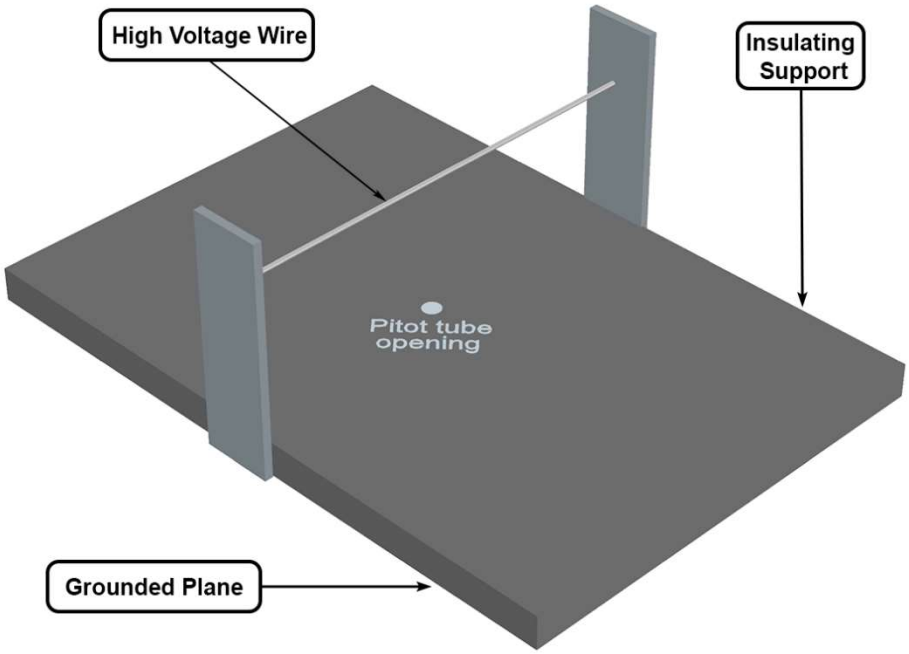

Figure 4.18. Indicative 3D illustration of the wire-plane electrode configuration used for the assessment of the EHD velocity limit.

For the estimation of the average EHD velocity limit, a needle-grid configuration was used. The setup is inserted into a cylindrical PVC tube that forms the boundaries of both the mathematical and experimental assessment, simplifying the problem, while its material has virtually no effect on the formation of the electric field. A vane type anemometer is attached at the exit of the tube, three centimetres after the grid, measuring the wind velocity and volume of the EHD setup.

The experimental tube has been selected to be of exactly the same diameter as the anemometer's rotary sensor (74 mm). A single steel needle with a tip radius r = 32 μm is used as an emitter and a steel grid made of wires with radius R = 520 μm is used as a collector, with a nominal aperture of 66%. Figure 4.19 displays an indicative 2D schematic and a 3D illustration of the needle-grid geometry. In this case, the average velocity limit of the geometry would be:

$$V_{D_{pt}} = \frac{2}{r_c^2}\int_0^{\varphi_{max}} \Delta(\varphi)\, d\Delta(\varphi) \sqrt{\frac{j_{S_R}(\varphi)\, S_R(\varphi)}{\rho_{fd}\, \mu}}\, d\varphi \quad \left(\frac{m}{s}\right) \tag{4.6}$$

Where r_c is the radius of the tube and φ_{max} the maximum emanation angle from the tip of the needle. As the tip of the needle resembles a hemisphere, this angle has a maximum of 90°. Depending on the distance d between the electrodes and the radius of the tube, the maximum angle may be limited to the angle that satisfies the condition $\Delta(\varphi) = r_c$. This model is an approximation that ignores the contribution of the needle's body. However, considering that the bulk of the corona current flow comes from emission angles up to 90°, the results should be very close to those acquired via the experiments [192].

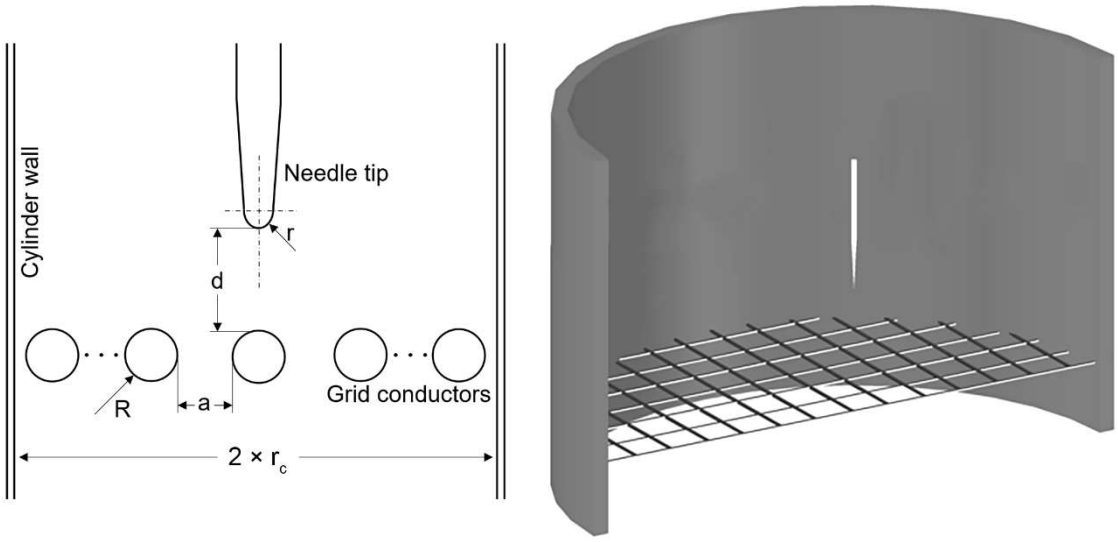

Figure 4.19. Indicative 2D schematic and 3D illustration of the needle-grid electrode configuration.

The required high voltage was supplied by an adjustable high voltage power source (Matsusada Precision W Series). A voltmeter combined with a Coline HV40B 40 kV 1000:1 high voltage probe were used for measuring the DC high voltage applied to the emitter electrode, with an accuracy of 1%. Current readings (corona current)

have been acquired by a high precision Thurlby 1503 ammeter with 1 nA sensitivity. The Pitot manometer is an Extech HD350 and the anemometer is an Extech AN200. All the experiments were performed in atmospheric air, with temperature ranging from 25 to 27 °C, and relative humidity between 45 and 52 %.

4.3.2 Results and Discussion

Wire-plane electrode setup

As seen from Figure 4.20, the actual maximum velocity tends to reach and surpass the theoretical velocity limit at higher voltages. The theoretical approach is based on the assumption of unipolar current flow and thus it is expected that the calculated EHD velocity limit will be aligned with the unipolar saturation current flow limit. The unipolar current flow limit can be expressed in relation to the length of the field line and is given by Eq. 3.31. The total unipolar saturation current limit for a wire-plane electrode geometry is given by Eq. 3.38.

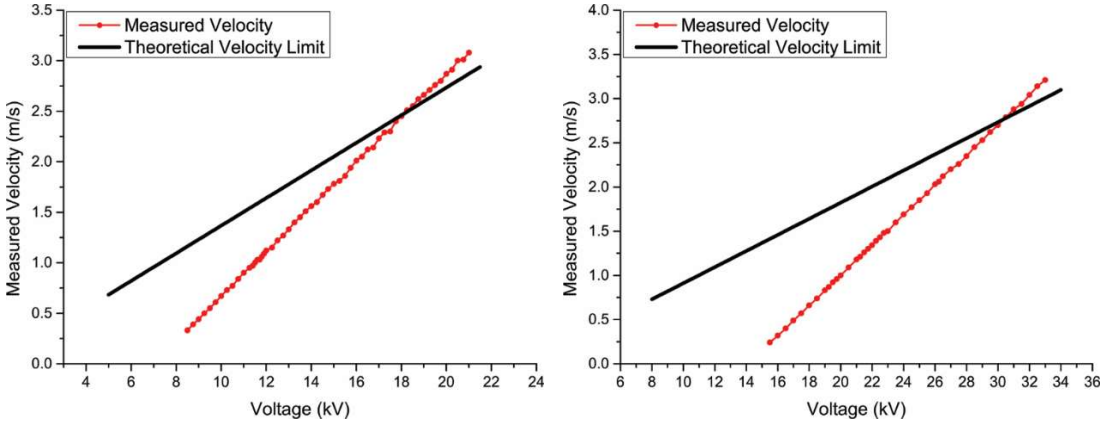

Figure 4.20. Comparison between the measured maximum velocity and the calculated velocity limit of a wire-plane configuration for $d = 2$ cm, $r = 40$ μm (left) and $d = 3$ cm, $r = 140$ μm (right).

Figures 36 and 37 display the comparison between the unipolar saturation current and the EHD velocity limit for various geometries. The average ion mobility in air is considered to be 1.8 10^{-4} $m^2V^{-1}s^{-1}$. It can be seen that the corona current tends to approach and or slightly exceed the saturation current limit near the breakdown point of the electrode setup. The closing difference between the experimental and the theoretical velocity limit displays the expected development of the phenomenon, as the ionic drift region outside the ionization region acts as an impedance and is what gives the corona discharge its characteristic intrinsic stability [205]. The graphs of

Figure 37 show that the voltage levels at which the measured current crosses the corresponding unipolar saturation current limit, or the measured air velocity crosses the theoretical velocity limit, are very near or coincide.

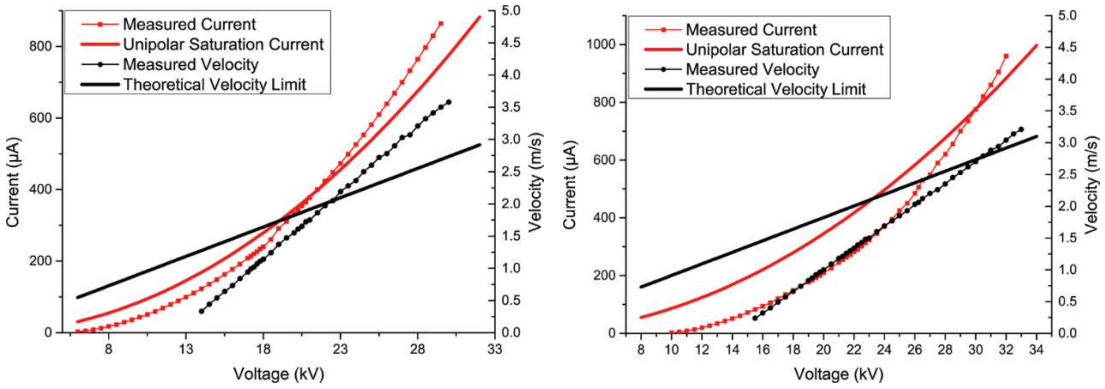

Figure 4.21. Comparison between the corona current and the EHD velocity of a wire-plane configuration for d = 3 cm, r = 40 μm (left) and d = 3 cm, r = 140 μm (right).

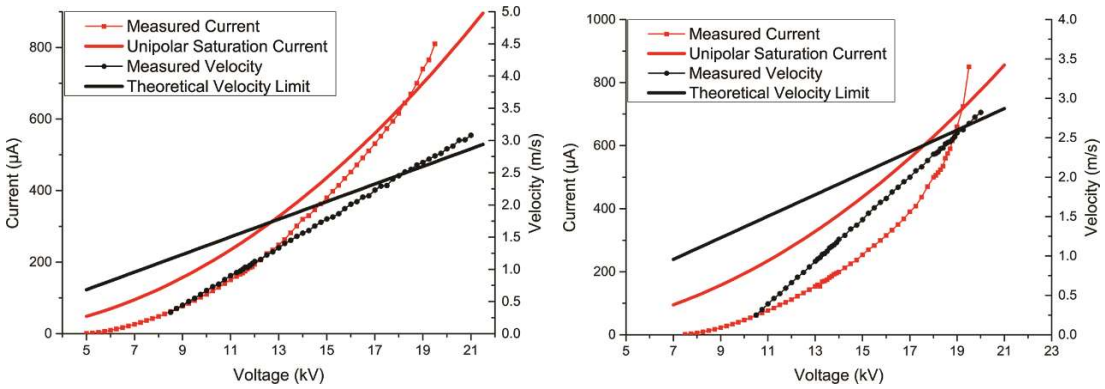

Figure 4.22. Comparison between the corona current and the EHD velocity of a wire-plane configuration for d = 2 cm, r = 40 μm (left) and d = 2 cm, r = 100 μm (right).

Once the unipolar saturation current limit has been surpassed, it is a clear indication that bipolar conduction phenomena are being formed, such as streamers, resulting to currents higher than the anticipated unipolar conduction limit [194]. Bipolar phenomena may exist before the unipolar saturation current limit but they surely exist if the measured current is higher that it. These phenomena however do not seem contribute to the EHD velocity. As it can be seen in Figure 4.23, from a highly asymmetric configuration that strongly favours the formation of such phenomena, the EHD velocity continues to increase linearly even after the unipolar saturation current limit, even though the current is growing exponentially.

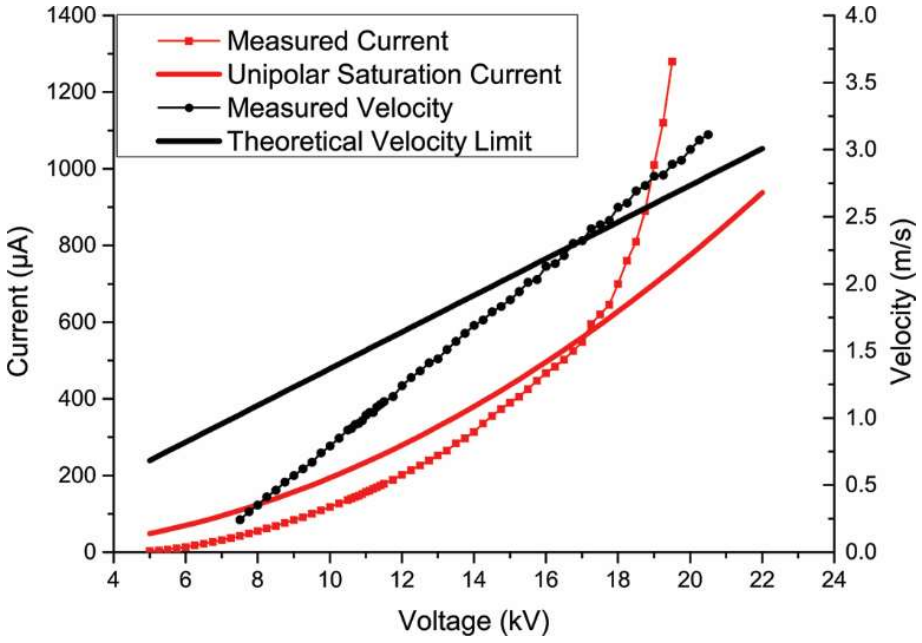

Figure 4.23. Comparison between the corona current and the EHD velocity for d = 2 cm, r = 30 μm.

Needle-grid electrode setup

In this section we examine the output of the mathematical model using a needle-grid electrode configuration and researching the average velocity limit of the geometry. In the case of the particular needle-grid geometry, Eq. 3.47 is adjusted to:

$$I_{s\,pt-p} = 2\,\pi\,\mu\,\varepsilon_0\,V^2 \int_0^{\varphi_{max}} \Delta(\varphi)\,d\Delta(\varphi)\,j_s(\varphi)\,d\varphi \quad A \tag{4.7}$$

As it can be seen from Figure 4.24, once again the EHD velocity is closely aligned with the unipolar current flow for a distance at least 50% greater than the discharge gap d. If the distance between the two electrodes is smaller, the electric field surrounding the needle's body can assist the acceleration of ions, particularly those emanating from large emission angles φ, resulting to velocities higher than anticipated (Figure 4.25).

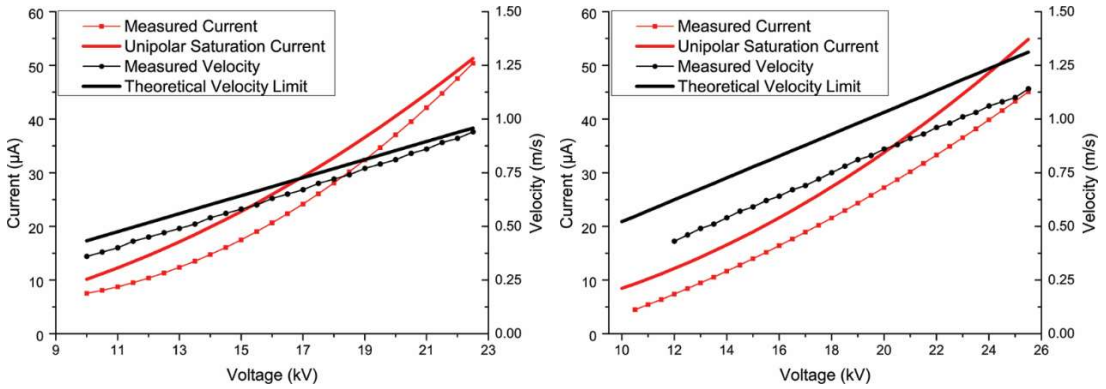

Figure 4.24. Comparison between the corona current and the EHD velocity for a needle-grid configuration of r = 32 μm and R = 520 μm, with an electrode gap d of 2.5 cm (left) and 3 cm (right).

It should also be noted that the type of grid affects both the formation of the electric field and the airflow impedance and, in extend, the EHD pump's velocity. As seen in Figure 4.26, the use of a grid with wires of smaller radius (R = 200 μm) and with greater nominal aperture (81%) significantly increases the corona current of the geometry. Even though the average air velocity increases, the difference is small compared to the increase of the current, especially considering the lower airflow impedance of the higher aperture grid.

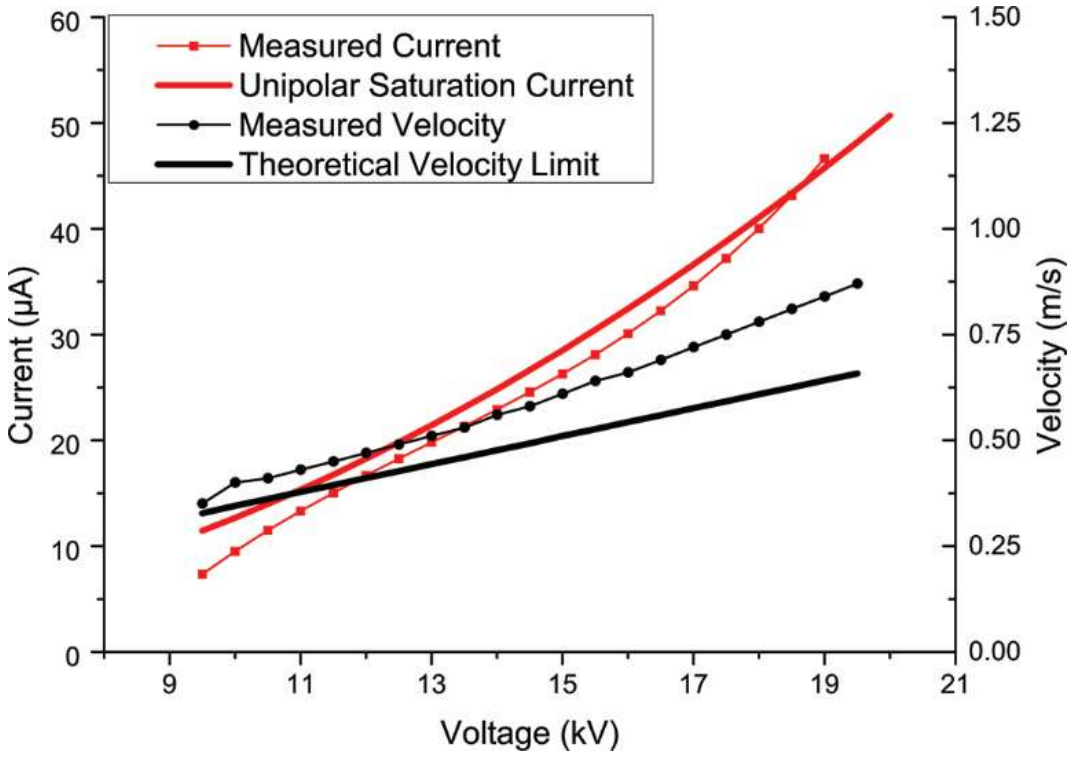

Figure 4.25. Comparison between the corona current and the EHD velocity for a needle-grid configuration of d = 2 cm, r = 32 μm and R = 520 μm.

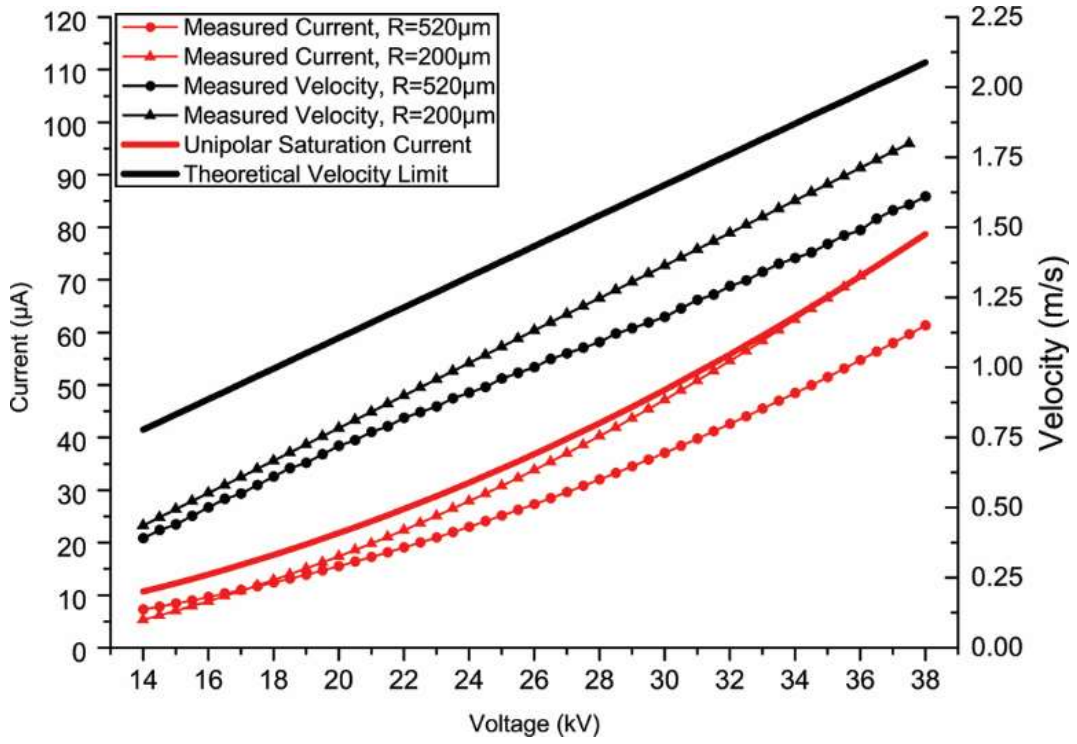

Figure 4.26. Comparison of the EHD velocity and the corona discharge current for needle-grid configurations using two different grid collectors (d = 4 cm, r = 32 μm).

Nevertheless, the efficiency n of the apparatus (Eq. 4.8) depends on the third power of the average air velocity and thus the use of the higher aperture grid results to a higher energy conversion efficiency, despite the disproportional increase of the corona current (Figure 4.27).

$$n = \frac{\frac{1}{2}\,\rho\,\pi\,r_c^2\,V_{EHD}^3}{V_{in}\,I_{in}} \times 100\% \tag{4.8}$$

Where V_{in} and I_{in} respectively are the input voltage and current of the EHD device.

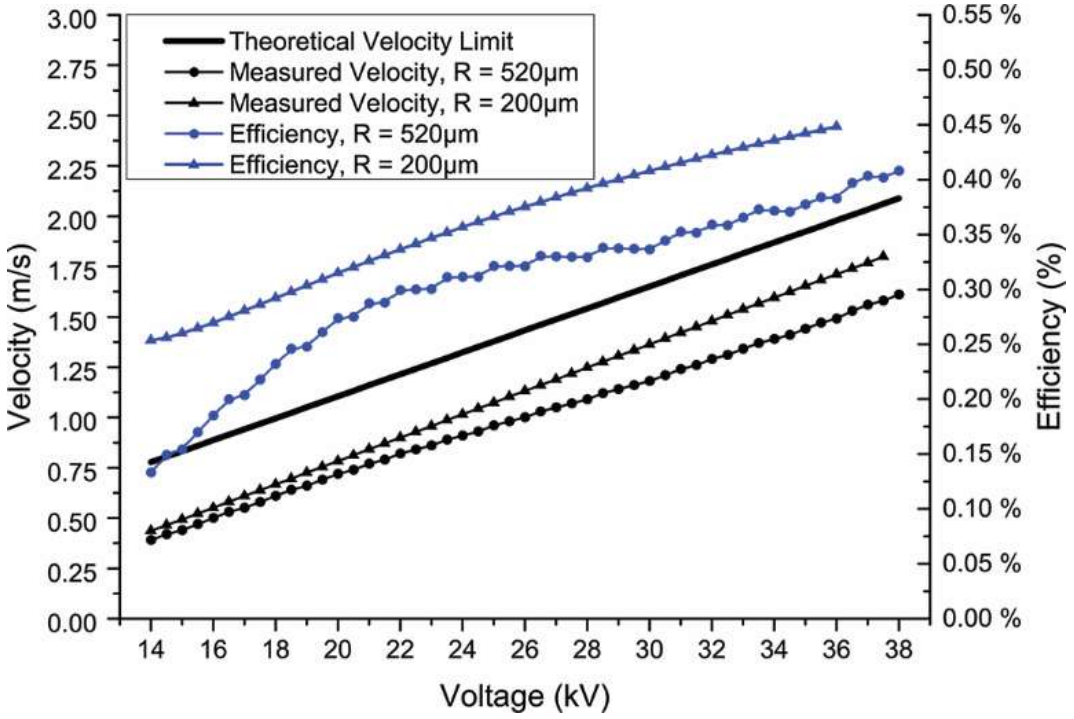

Figure 4.27. Comparison of the EHD velocity and the efficiency for needle-grid configurations using two different grid collectors (d = 4 cm, r = 32 μm).

CHAPTER 5 - Conclusions

The primary aim of this work was to study the development of the EHD phenomenon and contribute towards its advancement, particularly focused on EHD fluid accelerators. An extensive literature review revealed that, to this date, all mathematical models developed for assessing the primary performance characteristics of an EHD accelerator were either empirical or greatly simplified. Therefore, this work focused on providing analytical and, at the same time, practical mathematical models for the assessment of all primary performance characteristics describing EHD fluid accelerators (Voltage Potential, Electric Field Intensity, Corona Discharge Current and Fluid Velocity). This work covers all configurations where the emitter faces a plane or another identical electrode and has a cylindrical surface. For configurations where the emitter faces a plane or another identical electrode and has a spherical surface, Corona Discharge Current and Fluid Velocity models have been presented as well.

A mathematical model for the assessment of the voltage potential and the electric field gradient surrounding cylinder-plane or parallel cylinder-cylinder configurations was presented in chapter 3.1. In chapter 4.1, computer-assisted simulations were used to verify the validity of the mathematical model, with excellent results, proving its accuracy. The developed mathematical model has numerous practical applications, small and large scale alike. It can be used to calculate the electric field surrounding wire-plane or parallel wire configurations of any dimensions. Such geometries are present in a variety of devices, from EHD accelerators to electrostatic precipitators and ion generators. The wire-plane arrangement is particularly popular with EHD accelerators, as it creates a relatively large ionization area within a small space. It also may be used to estimate the potential at any point in the space surrounding these configurations by finding the exact equipotential line that crosses that point. These parameters are quite important in engineering design, such as for proper calculation of insulation and safety measures.

In chapter 3.2, an analytical solution for the assessment of the unipolar saturation current limit in various electrode configurations is introduced. With the proposed model based on the mathematical determination and analysis of the field lines, an exact solution giving the precise trajectory and length of each field line is presented for emitter electrodes with a cylindrical or spherical surface facing a plane

or an identical collector electrode. The unipolar saturation current limit for a positive corona discharge can then be calculated for any of the examined electrode geometries, if their spatial characteristics, the fluid's ion mobility and the applied voltage are known. In chapter 4.2, the mathematical models were experimentally verified for a wire-plane configuration, using emitters of varying radius. Both the total current and the distribution of the corona discharge current across the collecting electrode were investigated. The experimental results were closely related to the output of the proposed mathematical model and according to the known theory of corona discharges. According to these results, the corona discharge current on the collecting electrode is closely following a Warburg distribution; therefore, the bulk of the corona discharge current is contributed by field lines emanating from small emission angles.

Finally, in chapter 3.3, a mathematical model assessing the velocity limit of EHD fluid accelerators is presented. The model combines the known space charge distribution model with the analytical solution for the electric field lines developed in chapter 3.2.2. As such, the model is usable even if only the spatial characteristics of the geometry, the fluid's ion mobility and the applied voltage are known. The model can also assess both the average velocity limit of the entire apparatus and the velocity limit at the collision point of any electric field line. Do note that the developed EHD velocity limit models are based on the unipolar saturation current limit theory presented in chapter 3.2 and display the maximum possible fluid velocity attainable assuming unipolar conduction. The voltage for which every geometry fully attains unipolar conduction depends on the formation and strength of the developed electric field, i.e. on the geometrical characteristics of the geometry itself. Depending on the geometry, the corona current of the entire apparatus may be unable to reach the unipolar saturation current limit, such as when, for example, an emitter of high radius is placed at a short distance from a collector. The gap of such a configuration will go to breakdown long before the electric field can be strong enough to fully saturate the long field lines emanating from large emission angles. As the EHD velocity model is based on the unipolar saturation current limit model, the velocity is closely related to the unipolar discharge current of each geometry. The experimental testing presented in chapter 4.3 using both wire-plane 1and needle-grid configurations has validated the results of the model and the dependence on the unipolar discharge current. The corona discharge current of the EHD device may not always produce the expected velocity output, especially if the device is operating within a range that produces extensive

bipolar current conduction phenomena. These phenomena do not assist the acceleration of the fluid. This has been experimentally verified as well, since geometries that develop large currents due to extensive bipolar conduction display a disproportional rise to their input current after the unipolar saturation limit has been reached, while the fluid's velocity increases linearly. Experimental testing also revealed that the selection of a grid collector can be a complicated matter. Even though smaller grids can generate stronger electric fields that will trigger bipolar conduction, raising the corona discharge current of the device, their smaller aperture can improve the energy conversion efficiency. The selection of the collector electrodes according to the application, fluid and expected output velocity is subject to fluid dynamics optimization studies.

As shown in chapters 4.2.2 and 4.3.2, as the developed mathematical models assume unipolar current flow, they essentially display the current and velocity limit assuming unipolar conduction. However, as seen in Figure 4.16, the distribution of the discharge current in relation to the expected unipolar saturation current on the collector can greatly vary depending on the spatial characteristics of the geometry. This is to be expected with such asymmetric geometries - the smaller the emission angle φ is, the field lines are shorter and traverse through a stronger electric field. As the emission angle φ increases, the length of a field line and, in extend, the impedance of the drift region increases, while the average electric field intensity across it reduces. These parameters depend on the radius r and discharge gap d. Future experimental research may reveal the correlation of the corona current and the unipolar saturation current limit across the surface of the collecting electrode.

APPENDIX A*: Detailed solution of the equipotential lines model*

For a wire to grid electrode configuration, it is possible to achieve an accurate mathematical solution by assuming that the grid is forming a grounded plane. Then, according to the theory of mirror symmetry, the problem can be solved by describing the emitter electrode as a positive charge +q eccentrically placed inside the emitter and assuming that a negative charge -q of the exact same magnitude is being formed at the other side of the grid (Figure 3.1). According to the principle of superposition, the field intensity of a line charge is:

$$E(x) = \frac{q}{2\,\pi\,\varepsilon_0\,x}$$

Where *x* is the distance from the charge. For this geometry, we have that:

$$P_{el}(x,y) = \frac{-q_e}{2\pi\varepsilon_0}\ln\left(\frac{b}{a}\right) + P_{eq} \tag{5.1}$$

Where:

$$a = \sqrt{(x+c)^2 + y^2} \tag{5.2}$$

$$b = \sqrt{(x-c)^2 + y^2} \tag{5.3}$$

P_{eq} is a constant found from boundary conditions and indicates the plane of symmetry. However, for equal line charges of opposite polarity such in this case, the potential at the plane of symmetry is zero, therefore $P_{eq} = 0$.

Setting that:

$$A = \frac{-q_e}{2\pi\varepsilon_0} \tag{5.4}$$

Combining the above equations, we have that:

$$\ln\left(\frac{(x-c)^2 + y^2}{(x+c)^2 + y^2}\right) = \frac{2}{A}P_{eq} \tag{5.5}$$

Where P_{eq} is a number that denotes each different family of equipotential lines.

We need to transform this equation into a clear circle equation format: $((x-x_0)^2 + (y-y_0)^2 = R^2)$

Because the center of every cycle will always be on the Y-axis for parallel identical charges, then $y_0 = 0$. Assuming that:

$$B = e^{\frac{2}{A}P_{eq}}$$

$$B = \frac{(x-c)^2 + y^2}{(x+c)^2 + y^2}$$

$$B \times [(x+c)^2 + y^2] = (x-c)^2 + y^2$$

Using polynomial identities:

$$Bx^2 + 2Bxc + Bc^2 + By^2 = x^2 - 2xc + c^2 + y^2$$

$$(x^2 - Bx^2) - (2xc + 2Bxc) + (c^2 - Bc^2) + (y^2 - By^2) = 0$$

$$(1-B)x^2 - 2(1+B)xc + (1-B)c^2 + (1-B)y^2 = 0$$

Dividing everything with (1-B):

$$x^2 - 2\left(\frac{1+B}{1-B}\right)xc + c^2 + y^2 = 0$$

$$x^2 - 2\left(\frac{1+B}{1-B}\right)xc + c^2\left(\frac{1+B}{1-B}\right)^2 - c^2\left(\frac{1+B}{1-B}\right)^2 + c^2 + y^2 = 0$$

Reverse polynomial identity:

$$\left[x - \left(\frac{1+B}{1-B}\right)c\right]^2 - c^2\left(\frac{1+B}{1-B}\right)^2 + c^2 + y^2 = 0$$

So we have a circle equation of the form:

$$\left[x - \left(\frac{1+B}{1-B}\right)c\right]^2 + y^2 = c^2\left(\frac{1+B}{1-B}\right)^2 - c^2$$

Where x_{eq} is:

$$x_{eq} = \left(\frac{1+B}{1-B}\right)c \tag{5.6}$$

And r_{eq}^2 is:

$$r_{eq}^2 = c^2\left(\frac{1+B}{1-B}\right)^2 - c^2$$

$$r_{eq}^2 = c^2\frac{(1+B)^2}{(1-B)^2} - c^2\frac{(1-B)^2}{(1-B)^2}$$

$$r_{eq}^2 = c^2\left(\frac{(1+B)^2 - (1-B)^2}{(1-B)^2}\right)$$

$$r_{eq}^2 = c^2\frac{[(1+2B+B^2) - (1-2B+B^2)]}{(1-B)^2}$$

$$r_{eq}^2 = c^2\frac{4B}{(1-B)^2} \tag{5.7}$$

Simplifying further:

$$x_{eq} = \left(\frac{1+B}{1-B}\right)c = \frac{1+e^{\frac{2P_{eq}}{A}}}{1-e^{\frac{2P_{eq}}{A}}}c$$

The hyperbolic cotangent is:

$$coth_x = \frac{1+e^{-2x}}{1-e^{-2x}}$$

So:

$$x_{eq} = \frac{1+e^{\frac{2P_{eq}}{A}}}{1-e^{\frac{2P_{eq}}{A}}}c$$

$$x_{eq} = c\ coth\left(-\frac{P_{eq}}{A}\right) \tag{5.8}$$

As for the radius:

$$r_{eq}^2 = c^2\frac{4B}{(1-B)^2}$$

where:

$$\frac{4B}{(1-B)^2} = \frac{4B}{1-2B+B^2} = \left[\frac{1-2B+B^2}{4B}\right]^{-1} = \left[\frac{1+B^2}{4B} - \frac{2B}{4B}\right]^{-1}$$

$$= \left[\frac{1+e^{\frac{4P_{eq}}{A}}}{4e^{\frac{2P_{eq}}{A}}} - \frac{1}{2}\right]^{-1}$$

The hyperbolic cosine is:

$$cosh_x = \frac{1+e^{-2x}}{2e^{-x}}$$

So:

$$\left[\frac{1+e^{\frac{4P_{eq}}{A}}}{4e^{\frac{2P_{eq}}{A}}} - \frac{1}{2}\right]^{-1} \rightarrow \left[\frac{1}{2}\cosh\left(-\frac{2P_{eq}}{A}\right) - \frac{1}{2}\right]^{-1} = \frac{2}{\cosh\left(-\frac{2P_{eq}}{A}\right) - 1}$$

However:

$$cosh2x = 2\ sinh^2 x - 1$$

So:

$$\frac{2}{\cosh\left(-\frac{2P_{eq}}{A}\right) - 1} = \frac{1}{\sinh^2\left(-\frac{P_{eq}}{A}\right)} = \frac{1}{\sinh^2\left(-\frac{P_{eq}}{A}\right)}\frac{\cosh^2\left(-\frac{P_{eq}}{A}\right)}{\cosh^2\left(-\frac{P_{eq}}{A}\right)}$$

We have that:

$$\frac{1}{cosh^2 x} = 1 - tan^2 x \quad \& \quad \frac{cosh^2 x}{sinh^2 x} = coth^2 x$$

So:

$$\frac{1}{\sinh^2\left(-\frac{P_{eq}}{A}\right)} \frac{\cosh^2\left(-\frac{P_{eq}}{A}\right)}{\cosh^2\left(-\frac{P_{eq}}{A}\right)} = \coth^2\left(-\frac{P_{eq}}{A}\right) \frac{1}{\cosh^2\left(-\frac{P_{eq}}{A}\right)}$$

$$= \coth^2\left(-\frac{P_{eq}}{A}\right)\left[1 - \tan^2\left(-\frac{P_{eq}}{A}\right)\right]$$

We also have that:

$$\tan^2 x = \frac{1}{\coth^2 x}$$

So:

$$\coth^2\left(-\frac{P_{eq}}{A}\right)\left[1 - \tan^2\left(-\frac{P_{eq}}{A}\right)\right] = \coth^2\left(-\frac{P_{eq}}{A}\right) - \coth^2\left(-\frac{P_{eq}}{A}\right) \frac{1}{\coth^2\left(-\frac{P_{eq}}{A}\right)}$$

$$= \coth^2\left(-\frac{P_{eq}}{A}\right) - 1$$

Therefore:

$$r_{eq}^2 = c^2\left\{\coth^2\left(-\frac{P_{eq}}{A}\right) - 1\right\} = c^2 \coth^2\left(-\frac{P_{eq}}{A}\right) - c^2$$

Finally, we get that:

$$r_{eq}^2 = x_{eq}^2 - c^2 \qquad (5.9)$$

Now the center and radius of the equipotential circles are known. The geometric constants *r* (emitter radius), *d* (emitter to collector distance), and the physical constant *V* (emitter voltage) are known as well. The potential at X_1 (*d*,0) and X_2 (-*d*,0), on the surface of the electrodes, is known and is equal to *V* and -*V* respectively.

The distance *c* between the collector and the charge and the magnitude q of the charge are required. These two unknown figures can be found by solving a set of equations.

For a radius R equal to the radius r of the emitter electrode, we have:

$$r_{eq}^2 = x_0^2 - c^2$$

$$x_{eq} = d + r$$

Therefore, the distance from the collector to the charge q_l is:

$$r^2 = (d + r)^2 - c^2$$

$$0 = d^2 + 2dr + r^2 - c^2$$

$$c^2 = d^2 + 2dr$$

$$c = \sqrt{d^2 + 2dr} \tag{5.10}$$

We know that:

$$P_{el}(X1) = A\ ln\left(\frac{\sqrt{(d-c)^2}}{\sqrt{(d+c)^2}}\right) = A \ln \pm \left(\frac{d-c}{d+c}\right) \tag{5.11}$$

$$P_{el}(X2) = -A\ ln\left(\frac{\sqrt{(-d-c)^2}}{\sqrt{(-d+c)^2}}\right) = -A \ln \pm \left(\frac{-d-c}{-d+c}\right) \tag{5.12}$$

$$P_{el}(X1) = -P(X2) = V \tag{5.13}$$

Replacing Eq. 5.13 into 5.11 and 5.12 and subtracting 5.12 from 5.11, we get four possible equation combinations:

Case 1:

$$P_{el}(X1) = V = A \ln\left(\frac{d-c}{d+c}\right)$$

$$P_{el}(X2) = -V = A \ln\left(\frac{-d-c}{-d+c}\right)$$

$$2V = A \ln\left(\frac{\left(\frac{d-c}{d+c}\right)}{\left(\frac{-d-c}{-d+c}\right)}\right) = A \ln\left(\frac{(d-c)(-d+c)}{(d+c)(-d-c)}\right) = A \ln\left(\frac{-d^2+dc+dc-c^2}{-dc-d^2-c^2-dc}\right)$$

$$= A \ln\left(\frac{-d^2+2dc-c^2}{-d^2-2dc-c^2}\right) = A \ln\left(\frac{-(d-c)^2}{-(d+c)^2}\right) = 2A \ln\left(\frac{c-d}{c+d}\right)$$

Case 2:

$$P_{el}(X1) = V = A \ln\left(\frac{-d+c}{d+c}\right)$$

$$P_{el}(X2) = -V = A \ln\left(\frac{-d-c}{-d+c}\right)$$

$$2V = A \ln\left(\frac{\left(\frac{-d+c}{d+c}\right)}{\left(\frac{-c-d}{-d+c}\right)}\right) = A \ln\left(\frac{(-d+c)(-d+c)}{(d+c)(-c-d)}\right) = A \ln\left(\frac{-(d+c)^2}{-(d+c)^2}\right)$$

$$= 0\ (Unacceptable\ solution)$$

Case 3:

$$P_{el}(X1) = V = A\ln\left(\frac{d-c}{d+c}\right)$$

$$P_{el}(X2) = -V = A\ln\left(\frac{d+c}{-d+c}\right)$$

$$2V = A\ln\left(\frac{\left(\frac{d-c}{d+c}\right)}{\left(\frac{d+c}{-d+c}\right)}\right)$$

$$= A\ln\left(\frac{(d-c)(-d+c)}{(d+c)(d+c)}\right)\ (Unacceptable\ solution, results\ to\ an\ imaginary\ number)$$

Case 4:

$$P_{el}(X1) = V = A\ln\left(\frac{-d+c}{d+c}\right)$$

$$P_{el}(X2) = -V = A\ln\left(\frac{d+c}{-d+c}\right)$$

$$2V = A\ln\left(\frac{\left(\frac{-d+c}{d+c}\right)}{\left(\frac{d+c}{-d+c}\right)}\right) = A\ln\left(\frac{(-d+c)(-d+c)}{(d+c)(c+d)}\right) = 2A\ln\left(\frac{c-d}{c+d}\right)$$

The results of case 1 and 4 coincide, where the results of case 2 and 3 are unacceptable. Therefore, we have that the charge q is:

$$2V = 2A\ln\left(\frac{c-d}{c+d}\right)$$

From 5.4, we have that:

$$V = \frac{-q_e}{2\pi\varepsilon_0}\ln\left(\frac{c-d}{c+d}\right)$$

$$-q_l = \frac{2\,\pi\,\varepsilon_0\,V}{ln\left(\frac{c-d}{c+d}\right)} \qquad (5.14)$$

Therefore, if the radius *r* of the emitter electrode, the distance *d* between the collector and emitter electrodes and the potential *V* applied to the emitter electrode are all known, the formation of the equipotential lines is known as well.

APPENDIX B: *Proof that the field lines are perpendicular on the surface of the cylindrical emitter electrode and to the formed equipotential lines*

For the field line to emit perpendicularly from the point A(φ), then we should have a right triangle with:

$$OA \perp AB \;\Rightarrow\; OA^2 + AB^2 = OB^2 \;(Pythagorean\ theorem)$$

$$OA^2 + AB^2 = G(\varphi)^2$$

$$G(\varphi) = \sqrt{OA^2 + AB^2} = \sqrt{Y_0(\varphi)^2 + X_0(\varphi)^2}$$

Setting that:

$$A(\varphi) = \big(x'(\varphi), y'(\varphi)\big)$$

Where:

$$OA = r$$

Then we have:

$$AB^2 = MB^2 + MA^2 = [y'(\varphi) + Y_0(\varphi)]^2 + x'(\varphi)^2$$

The following figure is inserted as a reference.

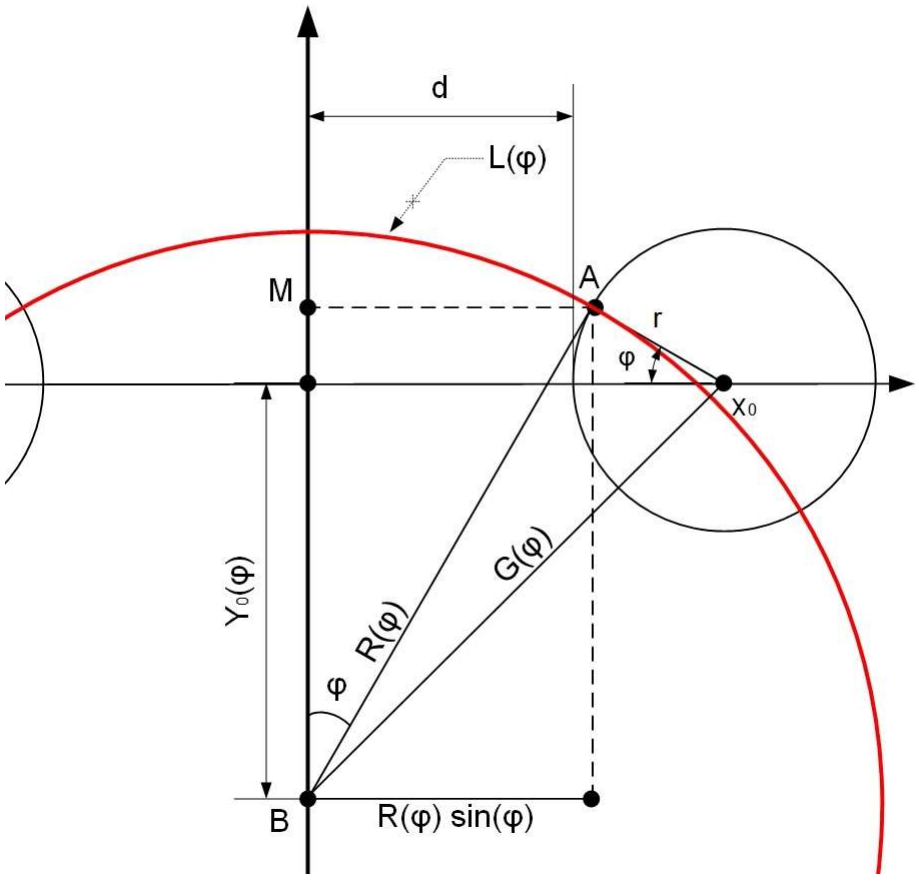

So, we should have:

$$R(\varphi) = \sqrt{r^2 + [y'(\varphi) + Y_0(\varphi)]^2 + x'(\varphi)^2}$$

$$Y_0(\varphi)^2 + X_0(\varphi)^2 = r^2 + [y'(\varphi) + Y_0(\varphi)]^2 + x'(\varphi)^2$$

$$Y_0(\varphi)^2 + X_0(\varphi)^2 = r^2 + y'(\varphi)^2 + 2y'(\varphi)Y_0(\varphi) + Y_0(\varphi)^2 + x'(\varphi)^2$$

$$X_0(\varphi)^2 = r^2 + y'(\varphi)^2 + 2y'(\varphi)Y_0(\varphi) + x'(\varphi)^2$$

$$Y_0(\varphi) = \frac{X_0(\varphi)^2 - r^2 - y'(\varphi)^2 - x'(\varphi)^2}{2y'(\varphi)}$$

We also have that:

$$x'(\varphi) = X_0(\varphi) - r\cos(\varphi)$$

$$y'(\varphi) = r\sin(\varphi)$$

Solving for $Y_0(\varphi)$:

$$Y_0(\varphi) = \frac{X_0(\varphi)^2 - r^2 - r^2\sin(\varphi)^2 - (X_0(\varphi)^2 - 2X_0(\varphi)\, r\cos(\varphi) + r^2\cos(\varphi)^2)}{2\, r\sin(\varphi)}$$

$$Y_0(\varphi) = \frac{X_0(\varphi)^2 - r^2 - r^2\sin(\varphi)^2 - X_0(\varphi)^2 + 2X_0(\varphi)\, r\cos(\varphi) - r^2\cos(\varphi)^2}{2\, r\sin(\varphi)}$$

$$Y_0(\varphi) = \frac{-r^2 - r^2\sin(\varphi)^2 + 2X_0(\varphi)\, r\cos(\varphi) - r^2\cos(\varphi)^2}{2\, r\sin(\varphi)}$$

$$\sin(\varphi)^2 + \cos(\varphi)^2 = 1$$

$$Y_0(\varphi) = \frac{-r^2 - r^2\,(\sin(\varphi)^2 + \cos(\varphi)^2) + 2X_0(\varphi)\, r\cos(\varphi)}{2\, r\sin(\varphi)}$$

$$Y_0(\varphi) = \frac{-r^2 - r^2 + 2X_0(\varphi)\, r\cos(\varphi)}{2\, r\sin(\varphi)}$$

$$Y_0(\varphi) = \frac{-2\, r^2 + 2X_0(\varphi)\, r\cos(\varphi)}{2\, r\sin(\varphi)}$$

$$Y_0(\varphi) = \frac{2\, r\left(-r + X_0(\varphi)\,\cos(\varphi)\right)}{2\, r\sin(\varphi)}$$

$$Y_0(\varphi) = \frac{-r + X_0(\varphi)\,\cos(\varphi)}{\sin(\varphi)} \qquad (5.15)$$

Eq. 5.15 coincides with Eq. 3.34 and proves that $\triangle OAB$ is a right triangle for any emission angle φ.

The following figure displays the formation of two equipotentials, randomly selected for arithmetic validation.

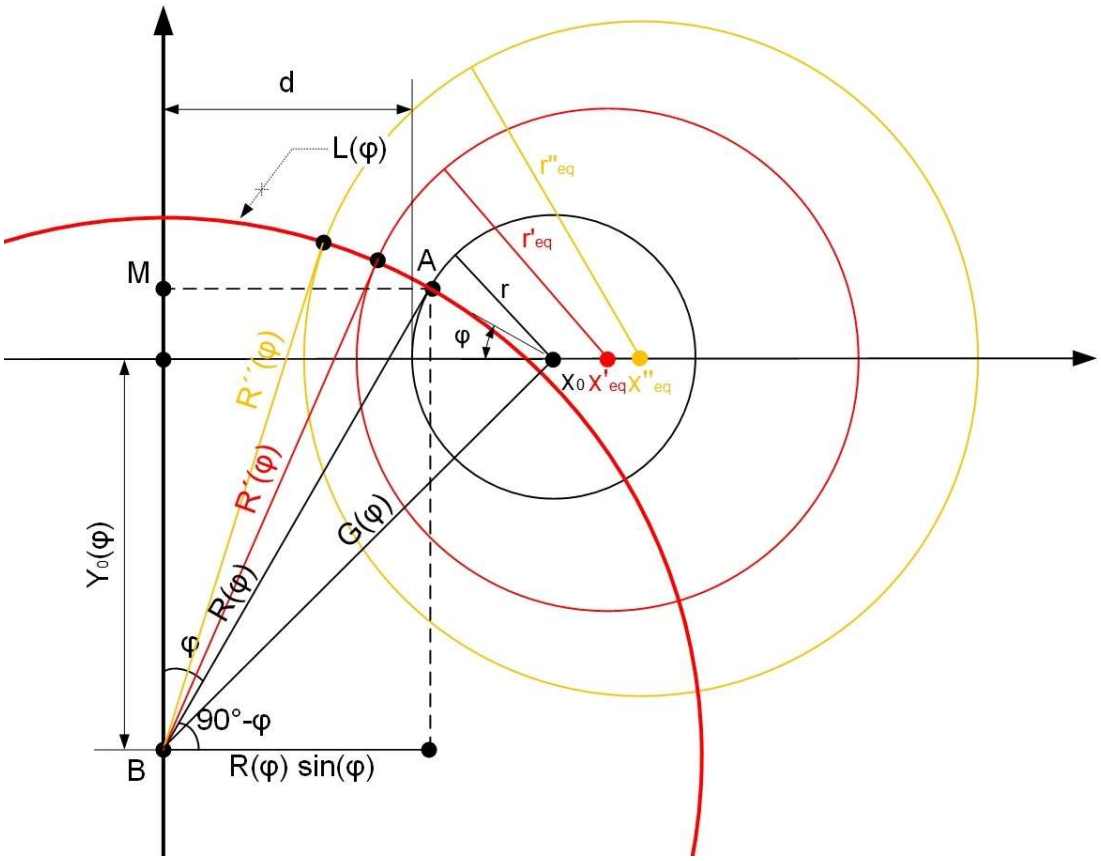

Solving arithmetically for d = 3 cm, r = 0.01 cm, φ = 30°, V = 1000, P_{eq} = 500, we have:

$$Y_0(\varphi) = 3.01\cot(30°) - 0.01\,csc\,(30°) = 5.1935$$

$$R(\varphi) = \frac{x_0 - r\cos(\varphi)}{\sin(\varphi)} = \frac{3.01 - 0.01 * \cos(30)}{\sin(30)} = 6.00268$$

$$x'_{eq} = \sqrt{d^2 + 2dr}\,\coth\left(-\frac{\ln\left(\frac{c-d}{c+d}\right)}{2}\right)$$

$$r'_{eq} = \sqrt{x_{eq}^2 - (\sqrt{d^2 + 2dr})^2}$$

C = 3.00998

$$x'_{eq} = 3.00998\,\coth\left(-\frac{\ln\left(\frac{0.00998}{6.00998}\right)}{2}\right) = 3.02$$

$$r'_{eq} = \sqrt{x_{eq}^2 - (\sqrt{d^2 + 2dr})^2} = 0.2458$$

$$G'(\varphi) = \sqrt{{r'_{eq}}^2 + R(\varphi)^2} = \sqrt{0.2458^2 + 6.00268^2} = 6.0077$$

$$G'(\varphi) = \sqrt{Y_0(\varphi)^2 + {x'_{eq}}^2} = \sqrt{5.1935^2 + 3.02^2} = 6.0077$$

Similarly for P_{eq} = 200:

C = 3.00998

$$x''_{eq} = \sqrt{d^2 + 2dr}\coth\left(-\frac{P_{eq}\ln\left(\frac{c-d}{c+d}\right)}{V}\right)$$

$$x''_{eq} = \sqrt{d^2 + 2dr} \times 1.1675197$$

$$x''_{eq} = 3.514215$$

$$\mathrm{r''_{eq}} = \sqrt{x''^2_{eq} - (\sqrt{d^2 + 2dr})^2} = 1.813755$$

$$G''(\varphi) = \sqrt{\mathrm{r''_{eq}}^2 + R(\varphi)^2} = \sqrt{1.813755^2 + 6.00268^2} = 6.2707$$

$$G''(\varphi) = \sqrt{Y_0(\varphi)^2 + x''^2_{eq}} = \sqrt{5.1935^2 + 3.514215^2} = 6.2707$$

REFERENCES

[1] N. Cabeo, *Philosophia magnetica*. Cologne: Francesco Suzzi, Ferrara, 1629.

[2] F. Hauksbee, *Physico-mechanical experiments on various subjects*. London, 1709.

[3] I. Newton, *Opticks*. London, 1718.

[4] A. P. Chattock, "On the velocity and mass of the ions in the electric wind in air," *Philosophical Magazine,* vol. 48, pp. 401-420, 1899.

[5] E. Lob, *Archiv der elektrischen Uebertragung 8*, 1954.

[6] D. J. Cravens, "Electric propulsion study (AL-TR-89-040)," Air Force Astronautics Lab, Edwards AFB, CA1990.

[7] A. A. Martins and M. J. Pinheiro, "Modeling of an EHD corona flow in nitrogen gas using an asymmetric capacitor for propulsion," *Journal of Electrostatics,* vol. 69, pp. 133-138, 2011.

[8] H. R. Velkoff and F. A. Kulacki, "Electrostatic cooling," Chicago, 1977.

[9] H. J. Schmid, S. Stolz, and H. Buggisch, "On the modelling of the electro-hydrodynamic flow field in electrostatic precipitators," *Flow, Turbulence and Combustion,* vol. 68, pp. 63-89, 2002.

[10] R.-T. Huang, W.-J. Sheu, and C.-C. Wang, "Heat transfer enhancement by needle-arrayed electrodes – An EHD integrated cooling system," *Energy Conversion and Management,* vol. 50, pp. 1789-1796, 2009.

[11] S. Lynikiene, "Carrot seed preparation in a corona discharge field," *CIGR Journal of Scientific Research and Development,* vol. 3, p. 021, 2001.

[12] B. L. Owsenek and J. Seyed-Yagoobi, "Theoretical and Experimental Study of Electrohydrodynamic Heat Transfer Enhancement Through Wire-Plate Corona Discharge," *Journal of Heat Transfer,* vol. 119, pp. 604-610, 1997.

[13] A. Richter and H. Sandmaier, "An electrohydrodynamic micropump," in *Micro Electro Mechanical Systems, 1990. Proceedings, An Investigation of Micro Structures, Sensors, Actuators, Machines and Robots. IEEE*, 1990, pp. 99-104.

[14] B. Wilson, *Treatise on electricity*. London, 1750.

[15] T. Cavallo, *A complete treatise of electricity*. London, 1777.

[16] M. Faraday, *Experimental researches in electricity*. London, 1834.

[17] J. C. Maxwell, *Treatise in electricity and magnetism*. Oxford: Oxford University Press, 1873.

[18] F. W. Peek, *Dielectric phenomena in high voltage engineering*. New York: McGraw-Hill Book Company, inc, 1915.

[19] T. Musha, "Theoretical explanation of the biefeld-brown effect," *Electric Spacecraft Journal,* vol. 31, pp. 21-29, 2000.

[20] M. Tajmar, "Biefeld–Brown effect: misinterpretation of corona wind phenomena," *AIAA Journal,* vol. 42, pp. 315-318, Feb. 2004.

[21] D. J. Harney, "An aerodynamic study of the electric wind," California Institute of Technology, Pasadena, 1957.

[22] O. M. Stuetzer, "Magnetohydrodynamics and electrohydrodynamics," *Physics of Fluids,* vol. 5, p. 534, 1962.

[23] R. D. Morrison and D. M. Hopstock, "The distribution of current in wire-to-cylinder corona," *Journal of Electrostatics,* vol. 6, pp. 349-360, Sep. 1979.

[24] J. Argyris and D. Scharpf, "Finite elements in time and space," *Nuclear Engineering and Design,* vol. 10, pp. 456-464, Dec. 1969.

[25] K. H. Huebner, *The finite element method for engineers*. New York: John Wiley & Sons, 1975.

[26] J. L. Davis and J. F. Hoburg, "Wire-duct precipitator field and charge computation using finite element and characteristics methods," *Journal of Electrostatics,* vol. 14, pp. 187-199, Aug. 1983.

[27] S. Cristina, G. Dinelli, and M. Feliziani, "Numerical computation of corona space charge and V-I characteristic in DC electrostatic precipitators," *Industry Applications, IEEE Transactions on,* vol. 27, pp. 147-153, 1991.

[28] D. Meeker, "Finite Element Method Magnetics (FEMM), Version 4.2," *Web Page: http://femm.berlios.de,* 2006.

[29] R. Morrow, "The theory of positive glow corona," *Journal of Physics D: Applied Physics,* vol. 30, p. 3099, Nov. 1997.

[30] G. Georghiou, R. Morrow, and A. Metaxas, "A two-dimensional, finite-element, flux-corrected transport algorithm for the solution of gas discharge

problems," *Journal of Physics D: Applied Physics,* vol. 33, p. 2453, Oct. 2000.

[31] P. Atten, K. Adamiak, and V. Atrazhev, "Electric corona discharge simulation in the hyperbolic point - ground plane configuration," in *Electrical Insulation and Dielectric Phenomena, 2002 Annual Report Conference on*, 2002, pp. 109-112.

[32] K. Adamiak and P. Atten, "Simulation of corona discharge in point–plane configuration," *Journal of Electrostatics,* vol. 61, pp. 85-98, Jun. 2004.

[33] L. Zhao, E. D. Cruz, K. Adamiak, A. Berezin, and J. Chang, "A numerical model of a wire-plate electrostatic precipitator under electrohydrodynamic flow conditions," in *CD–ROM proceedings of the international conference on air pollution abatement technologies-Future challenges, Cairns, Australia*, 2006.

[34] J. Suda, T. Ivancsy, I. Kiss, and I. Berta, "Complex analysis of ionic wind in ESP modeling," in *The 10th International conference on electrostatic precipitator, Australia*, 2006.

[35] J. Balaji, S. Wei, and T. Siddharth, "Modeling of dielectric barrier discharge and resulting fluid dynamics," in *44th AIAA Aerospace Sciences Meeting and Exhibit*, ed: American Institute of Aeronautics and Astronautics, 2006.

[36] D. B. Go, S. V. Garimella, and T. S. Fisher, "Numerical simulation of microscale ionic wind for local cooling enhancement," in *Thermal and Thermomechanical Phenomena in Electronics Systems, 2006. ITHERM'06. The Tenth Intersociety Conference on*, 2006, pp. 45-53.

[37] J. P. A. Bastos and N. Sadowski, *Electromagnetic Modeling by Finite Element Methods*. New York: Marcel Dekker, 2003.

[38] S. S. Rao, *The Finite Element Method in Engineering*: Elsevier Science, 2011.

[39] S. Moaveni, *Finite Element Analysis: Theory and Application with Ansys*. Englewood Cliffs, NJ: Prentice-Hall, 1999.

[40] D. Meeker, "FEMM-Finite Element Method Magnetics," ed, 1999.

[41] P. Glushchenko and Y. K. Stishkov, "Modeling of the through EHD-flow structure in a wire-wire system," *Surface Engineering and Applied Electrochemistry,* vol. 43, pp. 257-264, Aug. 2007.

[42] L. M. Dumitran, L. Dascalescu, P. V. Notingher, and P. Atten, "Modelling of corona discharge in cylinder-wire-plate electrode configuration," *Journal of electrostatics,* vol. 65, pp. 758-763, Nov. 2007.

[43] K. N. Kiousis and A. X. Moronis, "Experimental Investigation of EHD Flow in Wire to Cylinder Electrode Configuration," in *10th IASTED European Conference on Power and Energy Systems, Crete*, 2011, pp. 21-26.

[44] Y. K. Stishkov and V. Chirkov, "Computer simulation of EHD flows in a needle-plane electrode system," *Technical physics,* vol. 53, pp. 1407-1413, Nov. 2008.

[45] T. T. Brown, "Electrokinetic apparatus," US Patent 2949550, Aug 16, 1960, 1960.

[46] T. T. Brown, "Electrokinetic transducer," US Patent 3018394, Jan 23, 1962, 1962.

[47] T. T. Brown, "Electrokinetic apparatus," US Patent 3187206, 1 Jun 1965, 1965.

[48] A. P. d. Seversky, "Ionocraft," US Patent 3130945, Apr 28, 1964, 1964.

[49] E. A. Christenson and P. S. Moller, "Ion-neutral propulsion in atmospheric media," *AIAA Journal,* vol. 5, pp. 1768-1773, Oct. 1967.

[50] Scythe INC. (2013). *Scythe Mini Kaze Ultra 40 x 20 mm fan specifications*. Available: http://www.scythe-usa.com/product/acc/023/sy124020l_detail.html

[51] Yate Loon Electronics Co. Ltd. (2013). *Yate Loon D60SM-12C 60 x 20 mm fan specifications*. Available: http://www.yateloon.com/style/content/CN-02c/product_detail.asp?lang=2&customer_id=1356&name_id=31277&rid=58936&id=38826

[52] A. Morozov and L. Solov'ev, "Motion of charged particles in electromagnetic fields," *Reviews of Plasma Physics,* vol. 2, p. 201, 1966.

[53] J. S. Sovey and M. A. Mantenieks, "Performance and lifetime assessment of magnetoplasmadynamic arc thruster technology," *Journal of Propulsion and Power,* vol. 7, pp. 71-83, Jan. 1991.

[54] F. G. III and R. Spores, "Analysis of Hall-effect thrusters and ion engines for orbit transfer missions," in *32nd Joint Propulsion Conference and Exhibit*, ed: American Institute of Aeronautics and Astronautics, 1996.

[55] S. Marcuccio, A. Genovese, and M. Andrenucci, "Experimental performance of field emission microthrusters," *Journal of Propulsion and Power,* vol. 14, pp. 774-781, Sep. 1998.

[56] L. F. Velasquez-Garcia, A. I. Akinwande, and M. Martinez-Sanchez, "A Planar Array of Micro-Fabricated Electrospray Emitters for Thruster Applications," *Microelectromechanical Systems, Journal of,* vol. 15, pp. 1272-1280, Oct. 2006.

[57] F. X. Canning, C. Melcher, and E. Winet, "Asymmetrical capacitors for propulsion," *NASA TM CR-2004-213312,* Oct. 2004.

[58] L. Zhao and K. Adamiak, "EHD gas flow in electrostatic levitation unit," *Journal of electrostatics,* vol. 64, pp. 639-645, Jul. 2006.

[59] C. F. Chung and W. J. Li, "Experimental studies and parametric modeling of ionic flyers," in *Advanced intelligent mechatronics, 2007 IEEE/ASME international conference on*, 2007, pp. 1-6.

[60] L. Koziell, L. Zhao, J. Liaw, and K. Adamiak, "Experimental studies of EHD lifters," in *Proc. 2011 ESA Annual Meeting on Electrostatics*, Case Western Reserve University, Cleveland OH, 2011, pp. 1-6.

[61] C. Wan, "Electro-hydrodynamic (EHD) Thruster Analysis and Optimization," Master of Engineering Thesis, Albert Nerken School of Engineering, Cooper Union, New York, 2009.

[62] J.-M. Wang, T.-Y. Lin, and L.-J. Yang, "Electrohydrodynamic (EHD) micro-boat," in *Nano/Micro Engineered and Molecular Systems, 2007. NEMS'07. 2nd IEEE International Conference on*, 2007, pp. 584-587.

[63] H. S. Poon, M. K. Lam, M. Chow, and W. J. Li, "Noiseless and vibration-free ionic propulsion technology for indoor surveillance blimps," in *Robotics and Automation, 2009. ICRA'09. IEEE International Conference on*, 2009, pp. 2891-2896.

[64] L. Pekker and M. Young, "Model of Ideal Electrohydrodynamic Thruster," *Journal of Propulsion and Power,* vol. 27, pp. 786-792, 2011.

[65] J. Wilson, H. D. Perkins, and W. K. Thompson, "An investigation of ionic wind propulsion," ed: National Aeronautics and Space Administration (NASA), 2009.

[66] K. Masuyama, "Performance characterization of electrohydrodynamic propulsion devices," Master of Science Thesis, Department of Aeronautics and Astronautics, Massachusetts Institute of Technology, Massachusetts, USA, 2012.

[67] E. K. Levy, "The effects of electrostatic fields on forced convection heat transfer," ed. Massachusetts Massachusetts Institute of Technology, 1964.

[68] J. L. Fernandez, "Electrohydrodynamic enhancement of forced convection heat transfer in tubes," PhD Thesis, Department of Mechanical Engineering, University of Bristol, Bristol, 1975.

[69] J. Fernández and R. Poulter, "Radial mass flow in electrohydrodynamically-enhanced forced heat transfer in tubes," *International Journal of Heat and Mass Transfer,* vol. 30, pp. 2125-2136, Oct. 1987.

[70] M. M. Ohadi, D. A. Nelson, and S. Zia, "Heat transfer enhancement of laminar and turbulent pipe flow via corona discharge," *International Journal of Heat and Mass Transfer,* vol. 34, pp. 1175-1187, Apr. 1991.

[71] R. Baghaei Lakeh and M. Molki, "Targeted heat transfer augmentation in circular tubes using a corona jet," *Journal of Electrostatics,* vol. 70, pp. 31-42, Feb. 2012.

[72] J. Mathew and F. C. Lai, "Enhanced heat transfer in a horizontal channel with double electrodes," in *Conference Record of the 1995 IEEE Industry Applications Conference, Thirtieth IAS Annual Meeting*, Orlando, Florida, 1995, pp. 1472-1479.

[73] N. Kasayapanand and T. Kiatsiriroat, "EHD enhanced heat transfer in wavy channel," *International Communications in Heat and Mass Transfer,* vol. 32, pp. 809-821, May 2005.

[74] L. Léger, E. Moreau, G. Artana, and G. Touchard, "Influence of a DC corona discharge on the airflow along an inclined flat plate," *Journal of electrostatics,* vol. 51, pp. 300-306, May 2001.

[75] L. Léger, E. Moreau, and G. G. Touchard, "Effect of a DC corona electrical discharge on the airflow along a flat plate," *Industry Applications, IEEE Transactions on,* vol. 38, pp. 1478-1485, Nov. 2002.

[76] E. Moreau, L. Léger, and G. Touchard, "Effect of a DC surface-corona discharge on a flat plate boundary layer for air flow velocity up to 25m/s," *Journal of electrostatics,* vol. 64, pp. 215-225, Mar. 2006.

[77] D. B. Go, R. A. Maturana, T. S. Fisher, and S. V. Garimella, "Enhancement of external forced convection by ionic wind," *International Journal of Heat and Mass Transfer,* vol. 51, pp. 6047-6053, Dec. 2008.

[78] M. Robinson, "Convective heat transfer at the surface of a corona electrode," *International Journal of Heat and Mass Transfer,* vol. 13, pp. 263-274, Feb. 1970.

[79] T. Mizushina, H. Ueda, T. Matsumoto, and K. Waga, "Effect of electrically induced convection on heat transfer of air flow in an annulus," *Journal of Chemical Engineering of Japan,* vol. 9, pp. 97-102, 1976.

[80] H. Velkoff and R. Godfrey, "Low-velocity heat transfer to a flat plate in the presence of a corona discharge in air," *Journal of Heat Transfer,* vol. 101, p. 157, 1979.

[81] Y. Tada, A. Takimoto, and Y. Hayashi, "Heat transfer enhancement in a convective field by applying ionic wind," *Journal of Enhanced Heat Transfer,* vol. 4, 1997.

[82] D. Nelson, M. Ohadi, S. Zia, and R. Whipple, "Electrostatic effects on heat transfer and pressure drop in cylindrical geometries," in *ASME/JSME Thermal Engineering Joint Conference*, Reno, Nevada, 1991, pp. 33-39.

[83] M. M. Ohadi, "Heat transfer enhancement in heat exchangers," *ASHRAE Journal (American Society of Heating, Refrigerating and Air-Conditioning Engineers),* vol. 33, pp. 42-50, 1991.

[84] R. A. Moss and J. Grey, "Heat transfer augmentation by steady and alternating electric fields," in *Proceedings of the 1966 Heat Transfer and Fluid Mechanics Institute*, Santa Clara, California, 1966, pp. 210-235.

[85] R. H. Velkoff, "The effects of ionization on the flow and heat transfer of a dense gas in a transverse electrical field " in *Proceedings of the 1964 Heat Transfer and Fluid Mechanics Institute*, 1964, p. 260.

[86] F. Grosu and M. Bologa, "The influence of electric fields on heat-exchange processes in gases," *Appl. Elec. Phenom.(USSR),* vol. 5, pp. 350-356, 1968.

[87] H. Choi, "Electrohydrodynamic condensation heat transfer," *Journal of Heat Transfer,* vol. 90, p. 98, Feb. 1968.

[88] A. Seth and L. Lee, "The effect of an electric field in the presence of noncondensable gas on film condensation heat transfer," *Journal of Heat Transfer,* vol. 96, p. 257, 1974.

[89] R. E. Holmes and A. Chapman, "Condensation of Freon-114 in the Presence of a Strong Nonuniform, Alternating Electric Field," *Journal of Heat Transfer,* vol. 92, p. 616, Nov. 1970.

[90] C. Damianidis, M. Collins, T. Karayiannis, and P. Allen, "EHD effect in condensation of dielectric fluids Proceeding second international symposium on condensers and condensation," *Bath, UK,* pp. 505-18, 1990.

[91] T. Karayiannis, "EHD boiling heat transfer enhancement of R123 and R11 on a tube bundle," *Applied thermal engineering,* vol. 18, pp. 809-817, Sep. 1998.

[92] J. Bryan and J. Seyed-Yagoobi, "Electrohydrodynamically enhanced convective boiling: relationship between electrohydrodynamic pressure and momentum flux rate," *Journal of heat transfer,* vol. 122, pp. 266-277, 2000.

[93] Y. Feng and J. Seyed-Yagoobi, "Mechanism of annular two-phase flow heat transfer enhancement and pressure drop penalty in the presence of a radial electric field-turbulence analysis," *Journal of heat transfer,* vol. 125, pp. 478-486, 2003.

[94] H. Sadek, C. Y. Ching, and J. Cotton, "The effect of pulsed electric fields on horizontal tube side convective condensation," *International Journal of Heat and Mass Transfer,* vol. 53, pp. 3721-3732, Sep. 2010.

[95] J. H. Davidson and P. J. McKinney, "EHD flow visualization in the wire-plate and barbed plate electrostatic precipitator," *Industry Applications, IEEE Transactions on,* vol. 27, pp. 154-160, 1991.

[96] W.-J. Liang and T. Lin, "The characteristics of ionic wind and its effect on electrostatic precipitators," *Aerosol Science and Technology,* vol. 20, pp. 330-344, 1994.

[97] A. Niewulis, J. Podlinski, V. Shapoval, and J. Mizeraczyk, "Collection efficiency in narrow electrostatic precipitators with a longitudinal or transverse wire electrode," *Dielectrics and Electrical Insulation, IEEE Transactions on,* vol. 18, pp. 1423-1428, 2011.

[98] H. Fujishima, Y. Morita, M. Okubo, and T. Yamamoto, "Numerical simulation of three-dimensional electrohydrodynamics of spiked-electrode electrostatic precipitators," *Dielectrics and Electrical Insulation, IEEE Transactions on,* vol. 13, pp. 160-167, 2006.

[99] K. Adamiak and P. Atten, "Numerical simulation of the 2-D gas flow modified by the action of charged fine particles in a single-wire ESP," *Dielectrics and Electrical Insulation, IEEE Transactions on,* vol. 16, pp. 608-614, 2009.

[100] L. Zhao and K. Adamiak, "Numerical simulation of the electrohydrodynamic flow in a single wire-plate electrostatic precipitator," *Industry Applications, IEEE Transactions on,* vol. 44, pp. 683-691, 2008.

[101] N. Farnoosh, G. P. Castle, and K. Adamiak, "A 3D simulation of a single section electrostatic precipitator for dust particles removal," in *Electrical and Computer Engineering (CCECE), 2011 24th Canadian Conference on*, 2011, pp. 000749-000752.

[102] T. Yamamoto, S. Maeda, Y. Ehara, and H. Kawakami, "Development of EHD-assisted plasma electrostatic precipitator," *Industry Applications, IEEE Transactions on,* vol. 49, pp. 672-678, 2013.

[103] T. Yamamoto, S. Asada, and Y. Ehara, "Integrated Diesel Engine Emission Control Using Plasma-Combined Hybrid System," *Industry Applications, IEEE Transactions on,* vol. 49, pp. 2414-2420, 2013.

[104] A. P. Krueger, W. W. Hicks, and J. C. Beckett, "Effects of unipolar air ions on microorganisms and on evaporation," *Journal of the Franklin Institute,* vol. 266, pp. 9-19, Jul. 1958.

[105] N. N. Barthakur and S. Bhartendu, "Enhancement of evaporation rates from thin layers of liquids exposed to air ions," *International Journal of Biometeorology,* vol. 32, pp. 163-167, 1988.

[106] N. N. Barthakur, "An electrostatic method of drying saline water," *Drying Technology,* vol. 7, pp. 503-521, Sep. 1989.

[107] N. N. Barthakur and T. Al-Kanani, "An electrohydrodynamic technique for removal of moisture from soil samples," *Communications in Soil Science and Plant Analysis,* vol. 21, pp. 649-665, May 1990.

[108] Y. H. Chen and N. N. Barthakur, "Potato slab dehydration by air ions from corona discharge," *International Journal of Biometeorology,* vol. 35, pp. 67-70, Jun. 1991.

[109] N. N. Barthakur and N. P. Arnold, "Evaporation rate enhancement of water with air ions from a corona discharge," *International Journal of Biometeorology,* vol. 39, pp. 29-33, Mar. 1995.

[110] F. Lai, M. Huang, and D. Wong, "EHD-enhanced water evaporation," *Drying technology,* vol. 22, pp. 597-608, Jan. 2004.

[111] A. Alem-Rajabif and F. Lai, "EHD-enhanced drying of partially wetted glass beads," *Drying technology,* vol. 23, pp. 597-609, Mar. 2005.

[112] F. Hashinaga, T. R. Bajgai, S. Isobe, and N. N. Barthakur, "Electrohydrodynamic (EHD) Drying Of Apple Slices," *Drying Technology,* vol. 17, pp. 479-495, Mar. 1999.

[113] T. R. Bajgai and F. Hashinaga, "Drying Of Spinach With A High Electric Field," *Drying Technology,* vol. 19, pp. 2331-2341, Sep. 2001.

[114] W. Cao, Y. Nishiyama, and S. Koide, "Electrohydrodynamic drying characteristics of wheat using high voltage electrostatic field," *Journal of Food Engineering,* vol. 62, pp. 209-213, May 2004.

[115] F.-D. Li, L.-T. Li, J.-F. Sun, and E. Tatsumi, "Effect of electrohydrodynamic (EHD) technique on drying process and appearance of okara cake," *Journal of Food Engineering,* vol. 77, pp. 275-280, Nov. 2006.

[116] T. I. Goodenough, P. W. Goodenough, and S. M. Goodenough, "The efficiency of corona wind drying and its application to the food industry," *Journal of food engineering,* vol. 80, pp. 1233-1238, Jun. 2007.

[117] T. R. Bajgai and F. Hashinaga, "HIGH ELECTRIC FIELD DRYING OF JAPANESE RADISH," *Drying Technology,* vol. 19, pp. 2291-2302, Sep. 2001.

[118] A. Esehaghbeygi and M. Basiry, "Electrohydrodynamic (EHD) drying of tomato slices (Lycopersicon esculentum)," *Journal of Food Engineering,* vol. 104, pp. 628-631, Jun. 2011.

[119] A. A. Alemrajabi, F. Rezaee, M. Mirhosseini, and A. Esehaghbeygi, "Comparative Evaluation of the Effects of Electrohydrodynamic, Oven, and

Ambient Air on Carrot Cylindrical Slices during Drying Process," *Drying Technology,* vol. 30, pp. 88-96, Jan. 2012.

[120] S. Isobe, N. Barthakur, T. Yoshino, L. Okushima, and S. Sase, "Electrohydrodynamic drying characteristics of agar gel," *Food Science and Technology Research,* vol. 5, pp. 132-136, 1999.

[121] M. Basiry and A. Esehaghbeygi, "Electrohydrodynamic (EHD) drying of rapeseed (Brassica napus L.)," *Journal of Electrostatics,* vol. 68, pp. 360-363, Aug. 2010.

[122] F. Lai and K.-W. Lai, "EHD-enhanced drying with wire electrode," *Drying Technology,* vol. 20, pp. 1393-1405, Jul. 2002.

[123] F. Lai and R. Sharma, "EHD-enhanced drying with multiple needle electrode," *Journal of Electrostatics,* vol. 63, pp. 223-237, Mar. 2005.

[124] Y. Bai, Y. Hu, X. Li, and J. Li, "Experiment study of electrohydrodynamic (EHD) drying scallop," in *Power and Energy Engineering Conference, 2009. APPEEC 2009. Asia-Pacific*, 2009, pp. 1-4.

[125] F. Lai, "A prototype of EHD-enhanced drying system," *Journal of Electrostatics,* vol. 68, pp. 101-104, Feb. 2010.

[126] M. Robinson, "Movement of air in the electric wind of the corona discharge," Research-Cottrell INC, New Jersey, 1960.

[127] O. M. Stuetzer, "Ion drag pumps," *Journal of Applied Physics,* vol. 31, pp. 136-146, 1960.

[128] E. Moreau and G. Touchard, "Enhancing the mechanical efficiency of electric wind in corona discharges," *Journal of Electrostatics,* vol. 66, pp. 39-44, Jan. 2008.

[129] M. S. June, J. Kribs, and K. M. Lyons, "Measuring efficiency of positive and negative ionic wind devices for comparison to fans and blowers," *Journal of Electrostatics,* vol. 69, pp. 345-350, Aug. 2011.

[130] J.-D. Moon, D.-h. Hwang, and S.-T. Geum, "An EHD gas pump utilizing a ring/needle electrode," *IEEE Transactions on Dielectrics and Electrical Insulation,* vol. 16, pp. 352-358, Apr. 2009.

[131] C. Kim, D. Park, K. C. Noh, and J. Hwang, "Velocity and energy conversion efficiency characteristics of ionic wind generator in a multistage configuration," *Journal of Electrostatics,* vol. 68, pp. 36-41, Feb. 2009.

[132] H. Bondar and F. Bastien, "Effect of neutral fluid velocity on direct conversion from electrical to fluid kinetic energy in an electro-fluid-dynamics (EFD) device," *Journal of Physics D: Applied Physics,* vol. 19, pp. 1657-1663, Sep. 1986.

[133] K. Asano and K. Yatsuzuka, "Fundamental study of EHD pump with needle-cylinder electrodes," in *Electrical Insulation and Dielectric Phenomena, 1999 Annual Report Conference on*, 1999, pp. 785-788.

[134] M. Rickard, D. Dunn-Rankin, F. Weinberg, and F. Carleton, "Characterization of ionic wind velocity," *Journal of Electrostatics,* vol. 63, pp. 711-716, Jun. 2005.

[135] M. Rickard, D. Dunn-Rankin, F. Weinberg, and F. Carleton, "Maximizing ion-driven gas flows," *Journal of electrostatics,* vol. 64, pp. 368-376, 2006.

[136] J.-D. Moon, J.-S. Jung, J.-G. Kim, and S.-T. Geum, "An EHD Gas Pump Utilizing a Wet Porous Point Electrode," *Dielectrics and Electrical Insulation, IEEE Transactions on,* vol. 16, pp. 622-628, Jun. 2009.

[137] H. Nakamura and R. Ohyama, "An image analysis of positive ionic wind velocity under the DC corona discharge in needle-cylinder electrode system," presented at the IEEE Conference on Electrical Insulation and Dielectric Phenomena, 2009. CEIDP '09, Virginia Beach, 2009.

[138] W. Qiu, L. Xia, X. Tan, and L. Yang, "The Velocity Characteristics of a Serial-Staged EHD Gas Pump in Air," *Plasma Science, IEEE Transactions on,* vol. 38, pp. 2848-2853, Oct. 2010.

[139] Q. Wei, X. Lingzhi, Y. Lanjun, Z. Qiaogen, X. Lei, and C. Li, "Experimental Study on the Velocity and Efficiency Characteristics of a Serial Staged Needle Array-Mesh Type EHD Gas Pump," *Plasma Science and Technology,* vol. 13, p. 693, Dec. 2011.

[140] L. Zhao and K. Adamiak, "EHD flow in air produced by electric corona discharge in pin–plate configuration," *Journal of electrostatics,* vol. 63, pp. 337-350, Mar. 2004.

[141] Y. Kitahara, K. Aoyagi, and R. Ohyama, "An experimental analysis of ionic wind velocity characteristics in a needle-plate electrode system by means of laser-induced phosphorescence," in *Electrical Insulation and Dielectric*

Phenomena, 2007. CEIDP 2007. Annual Report-Conference on, 2007, pp. 529-532.

[142] E. Karakas, A. Begum, and M. Laroussi, "A positive corona-based ion wind generator," *IEEE Transactions on Plasma Science,* vol. 36, pp. 950-951, Aug. 2008.

[143] Y. Otsubo and K. Edamura, "Viscoelasticity of a dielectric fluid in nonuniform electric fields generated by electrodes with flocked fabrics," *Rheologica Acta,* vol. 37, pp. 500-507, 1998/11/01 1998.

[144] J. Zhang and F. Lai, "Effect of emitting electrode number on the performance of EHD gas pump in a rectangular channel," *Journal of Electrostatics,* vol. 69, pp. 486-493, Dec. 2011.

[145] P. Magnier, D. Hong, A. Leroy-Chesneau, J.-M. Pouvesle, and J. Hureau, "A DC corona discharge on a flat plate to induce air movement," *Journal of electrostatics,* vol. 65, pp. 655-659, Oct. 2007.

[146] B. Komeili, J. Chang, G. Harvel, C. Ching, and D. Brocilo, "Flow characteristics of wire-rod type electrohydrodynamic gas pump under negative corona operations," *Journal of Electrostatics,* vol. 66, pp. 342-353, May 2008.

[147] N. Takeuchi and K. Yasuoka, "Efficiency of a Wire-Rod Type Electrohydrodynamic Gas Pump Under Negative Corona Operation," *Plasma Science, IEEE Transactions on,* vol. 37, pp. 1021-1026, Jun. 2009.

[148] J.-D. Moon, D.-H. Hwang, J.-S. Jung, J.-G. Kim, and S.-T. Geum, "A sliding discharge-type EHD gas pump utilizing a saw-toothed-plate discharge electrode," *Dielectrics and Electrical Insulation, IEEE Transactions on,* vol. 17, pp. 742-747, Jun. 2010.

[149] R. Mestiri, R. Hadaji, and S. B. Nasrallah, "An experimental study of a plasma actuator in absence of free airflow: Ionic wind velocity profile," *Physics of Plasmas,* vol. 17, p. 083503, 2010.

[150] D. F. Colas, A. Ferret, D. Z. Pai, D. A. Lacoste, and C. O. Laux, "Ionic wind generation by a wire-cylinder-plate corona discharge in air at atmospheric pressure," *Journal of Applied Physics,* vol. 108, pp. 103306 - 103306-6, 2010.

[151] B. Owsenek, J. Seyed-Yagoobi, and R. Page, "Experimental investigation of corona wind heat transfer enhancement with a heated horizontal flat plate," *Journal of heat transfer,* vol. 117, pp. 309-315, 1995.

[152] H. Kalman and E. Sher, "Enhancement of heat transfer by means of a corona wind created by a wire electrode and confined wings assembly," *Applied thermal engineering,* vol. 21, pp. 265-282, Feb. 2001.

[153] A. Shooshtari, M. Ohadi, and F. H. R. Franca, "Experimental and numerical analysis of electrohydrodynamic enhancement of heat transfer in air laminar channel flow," in *Semiconductor Thermal Measurement and Management Symposium, 2003. Ninteenth Annual IEEE*, 2003, pp. 48-52.

[154] L. Zhao, K. Adamiak, and M. Mazumder, "Numerical and Experimental Studies of the Electrohydrodynamic Pump for Sampling System on Mars," presented at the Proceedings of the 2008 ESA Annual Meeting on Electrostatics, Minneapolis, MN, 2008.

[155] S. F. Bart, L. S. Tavrow, M. Mehregany, and J. H. Lang, "Microfabricated electrohydrodynamic pumps," *Sensors and Actuators A: Physical,* vol. 21, pp. 193-197, Feb 1990.

[156] A. Richter and H. Sandmaier, "An electrohydrodynamic micropump," presented at the Micro Electro Mechanical Systems, 1990. Proceedings, An Investigation of Micro Structures, Sensors, Actuators, Machines and Robots., Napa Valley, 1990.

[157] M. Sen, D. Wajerski, and M. Gad-el-Hak, "A novel pump for MEMS applications," *Journal of Fluids Engineering, Transactions of the ASME,* vol. 118, pp. 624-627, 1996.

[158] J. M. Crowley, G. S. Wright, and J. C. Chato, "Selecting a working fluid to increase the efficiency and flow rate of an EHD pump," *Industry Applications, IEEE Transactions on,* vol. 26, pp. 42-49, 1990.

[159] A. H. Sharbaugh and G. W. Walker, "The Design and Evaluation of an Ion-Drag Dielectric Pump to Enhance Cooling in a Small Oil-Filled Transformer," *Industry Applications, IEEE Transactions on,* vol. IA-21, pp. 950-955, 1985.

[160] M. Bologa, I. Kozhevnikov, and I. Kozhukhari, "Multistage electrohydrodynamical pump," in *Electrical Insulation and Dielectric Phenomena, 2000 Annual Report Conference on*, 2000, pp. 57-60.

[161] I. Kojevnikov, O. Motorin, M. Bologa, and A. Kojevnikova, "Optimization of the electrohydrodynamic pump," in *Electrical Insulation and Dielectric Phenomena, 2002 Annual Report Conference on*, 2002, pp. 204-207.

[162] I. Kano, K. Mizuochi, and I. Takahashi, "Micro-electrohydrodynamic pump by dielectric fluid: Improvement for performance of pressure using cylindrical electrodes," *Proceedings of the 6th JFPS International,* vol. 2, p. 3, 2005.

[163] I. Kano and I. Takahashi, "Improvement for pressure performance of Micro-EHD pump with an arrangement of thin cylindrical electrodes," *JSME International Journal Series B,* vol. 49, pp. 748-754, 2006.

[164] G. Fuhr, R. Hagedorn, T. Muller, W. Benecke, and B. Wagner, "Microfabricated electrohydrodynamic (EHD) pumps for liquids of higher conductivity," *Microelectromechanical Systems,* vol. 1, pp. 141-146, 1992.

[165] G. Fuhr, R. Hagedorn, T. Muller, W. Benecke, and B. Wagner, "Pumping of water solutions in microfabricated electrohydrodynamic systems," in *Micro Electro Mechanical Systems '92. An Investigation of Micro Structures, Sensors, Actuators, Machines and Robots.*, 1992, pp. 25-30.

[166] Y. Zhao, P. Foroughi, J. Lawler, and M. Ohadi, "Development of an electrohydrodynamic (EHD) micro pump for LN2 spot cooling," presented at the proceedings of International Mechanical Engineering Congress and Exposition, Washington, DC, 2003.

[167] P. Foroughi, V. Benetis, M. Ohadi, Y. Zhao, and J. Lawler, "Design, testing and optimization of a micropump for cryogenic spot cooling applications," in *Semiconductor Thermal Measurement and Management Symposium, 2005 IEEE Twenty First Annual IEEE*, 2005, pp. 335-340.

[168] C. C. Wong, D. R. Adkins, and D. Chu, "Development of a micropump for microelectronic cooling," presented at the International mechanical engineering congress and exhibition, Atlanta, 1996.

[169] A. Si-Hong and K. Yong-Kweon, "Fabrication and experiment of planar micro ion drag pump," in *International Conference on Solid State Sensors and Actuators*, Chicago, 1997, pp. 373-376 vol.1.

[170] J. Darabi, M. M. Ohadi, and D. DeVoe, "An electrohydrodynamic polarization micropump for electronic cooling," *Journal of Microelectromechanical Systems,* vol. 10, pp. 98-106, Mar. 2001.

[171] J. Darabi, M. Rada, M. Ohadi, and J. Lawler, "Design, fabrication, and testing of an electrohydrodynamic ion-drag micropump," *Microelectromechanical Systems, Journal of,* vol. 11, pp. 684-690, 2002.

[172] S. Chowdhury, J. Darabi, M. Ohadi, and J. Lawler, "Chip integrated micro cooling system for high heat flux electronic cooling applications," in *Proc of the International Conf on Thermal Challenges in Next Generation Electronic Systems (THERMES 2002)*, 2002, pp. 85-93.

[173] J. Darabi and K. Ekula, "Development of a chip-integrated micro cooling device," *Microelectronics Journal,* vol. 34, pp. 1067-1074, Nov. 2003.

[174] V. Benetis, A. Shooshtari, P. Foroughi, and M. M. Ohadi, "A source-integrated micropump for cooling of high heat flux electronics," in *Semiconductor Thermal Measurement and Management Symposium, 2003. Ninteenth Annual IEEE*, 2003, pp. 236-241.

[175] C. K. Lee, A. J. Robinson, and C. Y. Ching, "Development of EHD ion-drag micropump for microscale electronics cooling," presented at the Thermal Investigation of ICs and Systems, 2007. 13th International Workshop on, 2007.

[176] H. Yu, J. Yu, and C. Ma, "Design, fabrication and experimental research for an electrohydrodynamic micropump," *Science China Technological Sciences,* vol. 53, pp. 2839-2845, Oct. 2010.

[177] J. Darabi and C. Rhodes, "CFD modeling of an ion-drag micropump," *Sensors and Actuators A: Physical,* vol. 127, pp. 94-103, Feb. 2006.

[178] A. Rashkovan, E. Sher, and H. Kalman, "Experimental optimization of an electric blower by corona wind," *Applied Thermal Engineering,* vol. 22, pp. 1587-1599, Oct. 2002.

[179] F. Yang, N. E. Jewell-Larsen, D. L. Brown, K. Pendergrass, D. A. Parker, I. A. Krichtafovitch*, et al.*, "Corona driven air propulsion for cooling of

electronics," presented at the International Symposium on High Voltage Engineering, Rotterdam, 2003.

[180] N. E. Jewell-Larsen, E. Tran, I. A. Krichtafovitch, and A. V. Mamishev, "Design and optimization of electrostatic fluid accelerators," *IEEE Transactions on Dielectrics and Electrical Insulation,* vol. 13, pp. 191-203, Feb. 2006.

[181] D. Schlitz and V. Singhal, "An electro-aerodynamic solid-state fan and cooling system," in *Semiconductor Thermal Measurement and Management Symposium, 2008. Twenty-fourth Annual IEEE*, 2008, pp. 46-49.

[182] N. E. Jewell-Larsen, H. Ran, Y. Zhang, M. K. Schwiebert, K. A. H. Tessera, and A. V. Mamishev, "Electrohydrodynamic (EHD) cooled laptop," *Semiconductor Thermal Measurement and Management Symposium, 2009. SEMI-THERM 2009. 25th Annual IEEE,* pp. 261-266, Mar. 2009.

[183] N. Jewell-Larsen, Y. Zhang, M. Schwiebert, and K. Honer, "Collector-radiator structure for an electrohydrodynicamic cooling system," 2010.

[184] N. Jewell-larsen, K. Honer, and G. Joseph, "Electronic system adapted for passive convective cooling and staged use of electrohydrodynamic (ehd) and mechanical air movers for quiet forced convection assist," 2012.

[185] N. Jewell-larsen, "Electrohydrodynamic (ehd) fluid mover with field shaping feature at leading edge of collector electrodes," 2012.

[186] J.-S. Chang, H. Tsubone, G. Harvel, and K. Urashima, "Capillary/narrow flow channel driven EHD gas pump for an advanced thermal management of micro-electronics," in *Industry Applications Society Annual Meeting, 2008. IAS'08. IEEE*, 2008, pp. 1-8.

[187] J.-S. Chang, H. Tsubone, G. D. Harvel, and K. Urashima, "Narrow-Flow-Channel-Driven EHD Gas Pump for an Advanced Thermal Management of Microelectronics," *Industry Applications, IEEE Transactions on,* vol. 46, pp. 1151-1158, 2010.

[188] A. O. Ong, A. R. Abramson, and N. C. Tien, "Optimized and microfabricated ionic wind pump array as a next generation solution for electronics cooling systems," in *13th IEEE Intersociety Conference on Thermal and Thermomechanical Phenomena in Electronic Systems (ITherm)*, San Diego, California, 2012, pp. 1306-1311.

[189] I. Y. Chen, M.-Z. Guo, K.-S. Yang, and C.-C. Wang, "Enhanced cooling for LED lighting using ionic wind," *International Journal of Heat and Mass Transfer,* vol. 57, pp. 285-291, Jan. 2013.

[190] N. E. Jewell-Larsen, S. V. Karpov, H. Ran, P. Savalia, and K. A. Honer, "Investigation of dust in electrohydrodynamic (EHD) systems," presented at the Semiconductor Thermal Measurement and Management Symposium, 2010, SEMI-THERM 2010, 26th Annual IEEE, Santa Clara, 2010.

[191] J. S. Townsend, *Electricity in gases* New York: Oxford University press, 1915.

[192] R. S. Sigmond, "Simple approximate treatment of unipolar space-charge-dominated coronas: The Warburg law and the saturation current," *Journal of Applied Physics,* vol. 53, pp. 891-898, Feb. 1982.

[193] J. Kuffel, E. Kuffel, and W. Zaengl, *High voltage engineering fundamentals*: Newnes, 2000.

[194] R. S. Sigmond, "The unipolar corona space charge flow problem," *Journal of Electrostatics,* vol. 18, pp. 249-272, 1986.

[195] R. T. Waters and W. B. Stark, "Characteristics of the stabilized glow discharge in air," *Journal of Physics D: Applied Physics,* vol. 8, p. 416, 1975.

[196] P. Cooperman, "A theory for space-charge-limited currents with application to electrical precipitation," *American Institute of Electrical Engineers, Part I: Communication and Electronics, Transactions of the,* vol. 79, pp. 47-50, 1960.

[197] V. Mohnen, "Formation, nature, and mobility of ions of atmospheric importance," in *Electrical processes in atmospheres*, ed: Springer, 1976, pp. 1-17.

[198] K. Aplin, "Aspirated capacitor measurements of air conductivity and ion mobility spectra," *Review of scientific instruments,* vol. 76, p. 104501, 2005.

[199] M. Goldman, A. Goldman, and R. S. Sigfmond, "The corona discharge, its properties and specific uses," *Pure Appl Chem,* vol. 57, pp. 1353-1362, 1985.

[200] R. Sigmond and I. Lågstad, "Mass and species transport in corona discharges," *High Temp. Chem. Processes,* vol. 2, p. 5, 1993.

[201] G. H. Wannier, "On the motion of gaseous ions in a strong electric field. I," *Physical Review,* vol. 83, p. 281, 1951.

[202] J. Loschmidt, "On the size of the air molecules," *Journal of Chemical Education,* vol. 72, p. 870, 1995.

[203] J. C. Maxwell, "LX. A discourse on molecules," *The London, Edinburgh, and Dublin Philosophical Magazine and Journal of Science,* vol. 46, pp. 453-469, 1873.

[204] S. Kolassa and W. Schütz, "Advantages of the MAD/MEAN ratio over the MAPE," *Foresight: The International Journal of Applied Forecasting,* pp. 40-43, 2007.

[205] M. Goldman, A. Goldman, and R. Sigmond, "The corona discharge, its properties and specific uses," *Pure and Applied Chemistry,* vol. 57, pp. 1353-1362, 1985.

[206] M. Goldman and R. Sigmond, "Corona and insulation," *IEEE Transactions on Electrical Insulation,* vol. 2, pp. 90-105, 1982.

[207] G. Yinliang, X. Xiaodong, and C. Baozhi, "Investigation of Current Density Distribution Model for Barb-plate ESP," in *Electrostatic Precipitation*, K. Yan, Ed., ed: Springer Berlin Heidelberg, 2009, pp. 359-362.

[208] K. J. McLean and I. A. Ansari, "Calculation of the rod-plane voltage/current characteristics using the saturated current density equation and Warburg's law," *Physical Science, Measurement and Instrumentation, Management and Education - Reviews, IEE Proceedings A,* vol. 134, pp. 784-788, 1987.